

Washington University in St. Louis

Washington University Open Scholarship

McKelvey School of Engineering Theses & Dissertations

McKelvey School of Engineering

4-27-2021

Assessment and Diagnosis of Human Colorectal and Ovarian Cancer using Optical Imaging and Computer-aided Diagnosis

Yifeng Zeng

Washington University in St. Louis

Follow this and additional works at: https://openscholarship.wustl.edu/eng_etds

Recommended Citation

Zeng, Yifeng, "Assessment and Diagnosis of Human Colorectal and Ovarian Cancer using Optical Imaging and Computer-aided Diagnosis" (2021). *McKelvey School of Engineering Theses & Dissertations*. 1092. https://openscholarship.wustl.edu/eng_etds/1092

This Dissertation is brought to you for free and open access by the McKelvey School of Engineering at Washington University Open Scholarship. It has been accepted for inclusion in McKelvey School of Engineering Theses & Dissertations by an authorized administrator of Washington University Open Scholarship. For more information, please contact digital@wumail.wustl.edu.

WASHINGTON UNIVERSITY IN ST. LOUIS

McKelvey School of Engineering
Department of Biomedical Engineering

Dissertation Examination Committee:

Quing Zhu, Chair

Hong Chen

Ian S. Hagemann

Matthew Lew

Yuan-Chuan Tai

Assessment and Diagnosis of Human Colorectal and Ovarian Cancer using
Optical Imaging and Computer-aided Diagnosis

by

Yifeng Zeng

A dissertation presented to
The Graduate School
of Washington University in
partial fulfillment of the
requirements for the degree
of Doctor of Philosophy

May 2021
St. Louis, Missouri

© 2021, Yifeng Zeng

Table of Contents

List of Figures	v
List of Tables	vii
Acknowledgements	viii
Abstract of the Dissertation	x
Chapter 1 Introduction	1
1.1 Motivation	1
1.2 Optical Imaging and Computer-aided Diagnosis	2
1.3 Organization of the Dissertation	3
References	4
Chapter 2: The Angular Spectrum of the Scattering Coefficient Map Reveals Subsurface Colorectal Cancer	6
2.1 Background	6
2.2 Method and Materials.....	7
2.2.1 Colon Specimen Preparation.....	7
2.2.2 SS-OCT System Setup.....	7
2.2.3 Automatic Image Surface Delineation.....	8
2.2.4 Scattering Coefficient Mapping.....	9
2.2.5 Angular Spectrum	11
2.2.6 Data analysis	12
2.3 Results	12
2.3.1 OCT images of normal and cancerous specimens	12
2.3.2 Scattering coefficient maps of human colorectal specimens	13
2.3.3 Angular spectrum analysis and its strength in revealing subsurface cancer	16
2.4 Discussion	19
2.5 Conclusion.....	21
References	21
Chapter 3: Real-time colorectal cancer diagnosis using PR-OCT with deep learning	23
3.1 Background	23
3.2 Materials and Methods	24
3.2.1 Colon specimen preparation	24

3.2.2 OCT image labeling and pattern marking.....	25
3.2.3 Dense object detection with RetinaNet.....	26
3.2.4 Statistical analysis.....	28
3.3 Results	28
3.3.1 Preparation of PR-OCT: establishing OCT dataset and training RetinaNet model.....	29
3.3.2 Qualitative OCT imaging results	30
3.3.3 Teeth pattern detection result.....	31
3.3.4 Identifying colon region with endogenous optical contrast	34
3.4 Discussion	35
References	38
Chapter 4: Diagnosing colorectal abnormalities using scattering coefficient maps acquired from optical coherence tomography.....	43
4.1 Background	43
4.2 Materials & Methods.....	44
4.2.1 Colon Specimen Preparation.....	44
4.2.2 <i>en face</i> Scattering Coefficient Mapping	45
4.2.3 Feature Extraction.....	48
4.2.4 Feature Selection & Image Classification.....	50
4.3 Results	51
4.3.1 <i>en face</i> Scattering Coefficient Maps	51
4.3.2 Feature Importance	52
4.3.3 Image Classification.....	54
4.4 Discussion	56
References	59
Chapter 5: Adaptive Boosting (AdaBoost)-based multi-wavelength spatial frequency domain imaging and characterization for <i>ex vivo</i> human colorectal tissue assessment.....	62
5.1 Background	62
5.2 Materials and Methods	63
5.2.1 Colon specimen preparation	63
5.2.2 SFDI System	63
5.2.3 Absorption and scattering feature characterization.....	64
5.2.4 Feature selection	64

5.2.5 AdaBoost classifier	65
5.2.6 Statistical analysis.....	68
5.3 Results	68
5.3.1 Reconstructed absorption and reduced scattering coefficient maps	69
5.3.2 Absorption and scattering feature characterization.....	69
5.3.3 Testing result of AdaBoost classifier and SVM classifiers using all wavelengths	74
5.4 Discussion	75
References	77
Chapter 6: Histogram Analysis of <i>en face</i> Scattering Coefficient Map Predicts Malignancy in Human Ovarian Tissue	80
6.1 Background	80
6.2 Materials and Methods	81
6.2.1 Ovary sample preparation.....	81
6.2.2 Feature extraction	81
6.2.3 Feature selection and classification	83
6.3 Results	84
6.3.1 B-scan images of ovary samples.....	85
6.3.2 Scattering coefficient maps of human ovary specimens	85
6.3.3 Histogram analysis.....	87
6.3.4 Training and testing results of two predictive models	87
6.4 Discussion	89
References	93
Chapter 7: Conclusion and Future Work.....	96
Curriculum Vitae	98

List of Figures

Figure 2.1 Homemade SS-OCT system.....	8
Figure 2.2 Surface detection of typical SS-OCT images with challenges.....	10
Figure 2.3 Scattering coefficient fitting.....	11
Figure 2.4 OCT images of normal and cancer colon specimens.....	14
Figure 2.5 Scattering coefficient maps.....	15
Figure 2.6 Scattering coefficient maps.....	16
Figure 2.7. Angular spectrum images and their angular spectrum indexes quantified with a two-ellipse method.....	18
Figure 2.8. Angular spectrum index.....	19
Figure 3.1 PR-OCT workflow.....	26
Figure 3.2 An illustration of RetinaNet.....	28
Figure 3.3 3D-OCT images of normal and cancerous human colon specimens.....	32
Figure 3.4 PR-OCT dentate pattern detection results.....	33
Figure 3.5 Plot of the ROC of the binary classification (normal vs. cancer) result.....	35
Figure 4.1 Integral image example.....	47
Figure 4.2 Scattering coefficient maps.....	52
Figure 4.3 Feature importance for identifying abnormal tissue from normal tissue.....	53
Figure 4.4 Feature importance for distinguishing adenomatous polyp from cancerous tissue.....	54
Figure 5.1 Flow chart for AdaBoost algorithm.....	67
Figure 5.2 Absorption and reduced scattering coefficient maps (at 660 nm and 950 nm), H&E stained histology results and photographs of a T2 adenocarcinoma and corresponding normal tissue.....	70
Figure 5.3 Absorption and reduced scattering coefficient maps (at 660 nm and 950 nm), H&E stained histology results and photographs of an adenomatous polyp and corresponding normal tissue.....	71
Figure 5.4 Boxplot of averaged absorption coefficient (a) and reduced scattering coefficient (b).....	72
Figure 5.5 Receiver operating characteristic curve for abnormal vs. normal.....	73

Figure 5.6 Receiver operating characteristic curve for adenomatous polyp vs. normal AdaBoost classifier	74
Figure 6.1 Representative OCT images of benign and malignant ovary specimens	84
Figure 6.2 Scattering coefficient maps of human ovarian tissues	86
Figure 6.3 Histogram analysis of one representative malignant ovary (A) and one representative benign ovary (B)	88
Figure 6.4 Boxplot of the six features extracted from histogram analysis of scattering maps of malignant ovaries, benign ovaries, and benign fallopian tubes	88
Figure 6.5 Testing results of two optimal data sets ([mean, entropy] and [energy, skewness, entropy]) used to train two classification models	89

List of Tables

Table 3.1 Colorectal Lesion characteristics	29
Table 3.2 Cohen's d between all scores of five tissue groups	34
Table 4.1 Characteristics of the studied colorectal patients.....	45
Table 4.2 Surface detection time using different algorithms on various volumes of interest	48
Table 4.3 Testing AUCs for distinguishing abnormal from normal tissue.....	55
Table 4.4 Testing AUCs for distinguishing adenomatous polyp from cancerous tissue.....	56
Table 6.1 Ovarian Lesion characteristics.....	82

Acknowledgements

I would like to express my sincere appreciation and gratitude to my principal investigator and dissertation committee chair Prof. Quing Zhu. She guided me throughout my Ph.D. studies with patience and sincerity. She always motivates me with her passion in research and positive attitude towards challenges. Thanks for teaching me how to approach important clinical and scientific problems with creativity and integrity.

I am thankful to my lab mates in the Optical and Ultrasound Imaging Laboratory at Washington University in St. Louis, including Dr. Sreyankar Nandy, Dr. Atahar Mostafa, Dr. K. M. Shihab Uddin, Dr. Bin Rao, Xiandong Leng, Eghbal Amidi, Guang Yang, Shuying Li, Menghao Zhang, Hongbo Luo, Shiqi Xu, Sitai Kou, and Yun Zou. My Ph.D. dissertation would not have been completed without their help.

Thanks for my committee members Dr. Hong Chen, Dr. Yuan-Chuan Tai, Dr. Matthew Lew, and Dr. Ian S. Hagemann for their precious suggestions.

Finally, I want to thank my family for their accompaniment and support through my Ph.D. life, including my parents, my wife, and my two kittens. I cannot finish this thesis dissertation without them.

Yifeng Zeng

Washington University in St. Louis

May 2021

Dedicated to my parents and wife.

ABSTRACT OF THE DISSERTATION

Assessment and Diagnosis of Human Colorectal and Ovarian Cancer using

Optical Imaging and Computer-aided Diagnosis

by

Yifeng Zeng

Doctor of Philosophy in Biomedical Engineering

Washington University in St. Louis, 2021

Professor Quing Zhu, Advisor

Tissue optical scattering has recently emerged as an important diagnosis parameter associated with early tumor development and progression. To characterize the differences between benign and malignant colorectal tissues, we have created an automated optical scattering coefficient mapping algorithm using an optical coherence tomography (OCT) system. A novel feature called the angular spectrum index quantifies the scattering coefficient distribution. In addition to scattering, subsurface morphological changes are also associated with the development of colorectal cancer. We have observed a specific mucosa structure indicating normal human colorectal tissue, and have developed a real-time pattern recognition neural network to localize this specific structure in OCT images, enabling classification of the morphological changes associated with the progression of human colon cancer. Differentiating normal from malignant tissues is critically important, however, identifying different subtypes of abnormalities is also useful in clinical diagnosis. We have designed a feature extraction method using texture features and computer-vision related features to characterize different types of colorectal tissues. We first ranked these features according to their importance, then trained two classifiers: one for normal vs. abnormal, and the other one for cancer vs. polyp, where polyp is a pre-cancer marker. In assessing tissue

abnormalities, optical absorption reveals contrast related to tumor microvasculature and tumor angiogenesis. Spatial frequency domain imaging (SFDI), a powerful wide field, label-free imaging modality, is sensitive to both absorption and scattering. We designed a computer-aided diagnostic algorithm, AdaBoost, to use multispectral SFDI imaging for *ex vivo* assessment of different types of colorectal tissues, including normal and cancerous tissue and adenomatous polyps. For diagnosis of human ovarian cancer, we first designed a histogram-based feature extraction algorithm. Then we trained and tested traditional machine learning methods utilizing these histogram features for ovarian cancer diagnosis. We also explored the use of these features in characterizing human fallopian tubes, which are believed to be the origin of the most lethal subtype of human ovarian cancers.

Chapter 1 Introduction

1.1 Motivation

As of 2020, colorectal cancer (CRC) is estimated to be the third most prevalent type of cancer in both men and women in the United States and to have the third highest mortality rate among all cancer types [1]. In the US, approximately 145,600 cases of colorectal cancer are diagnosed annually [2]. Arising from the inner surface – the mucosal layer – of the colon, these cancers can penetrate the deeper layers of the colon and spread to other organs. Left untreated, the disease is fatal. Current endoluminal screening or surveillance for colorectal malignancy is performed by flexible endoscopy, which involves visually inspecting the mucosal lining of the colon and rectum with an optical camera mounted on the endoscope. Abnormal appearing areas are then biopsied for histologic analysis. Although it is the current standard of care, endoscopic screening has several shortcomings. First, this technique relies on visual detection of abnormal tissue to guide biopsy site selection. However, because small or sessile lesions are hard to detect with the naked eye, early malignancies are often missed [3, 4]. Second, visual endoscopy can detect changes only in the surface of the bowel wall, and because quantitative measurements are lacking, interpreting the images is subjective and subject to inter-reader variation. To improve screening and surveillance of colorectal cancers, better imaging modalities and methods are needed.

Better imaging would also help combat ovarian cancer, the fifth leading cause of cancer death among women and the most lethal gynecologic cancer [1,5]. Due to its typically late detection, ovarian cancer has a 5-year survival rate of only 40% [6]. However, when diagnosed at stage I, ovarian cancer has a 5-year survival rate of 92% [1]. Currently the best screening method for women at high risk is a CA125 blood test combined with transvaginal ultrasound; unfortunately, the screening's sensitivity and specificity are low, and only 15% of ovarian cancers are diagnosed

at an early stage [7]. The standard of care for high-risk women is bilateral salpingo-oophorectomy (RRSO), which can reduce the risk of ovarian cancer by more than 50% [8]. However, RRSO causes early menopause, which also carries risks, including accelerated bone loss and increased risk of heart disease. Ovarian cancer is a heterogeneous disease at the molecular and histologic levels [9]. During the progression of ovarian cancer, the collagen fiber architecture of the extracellular matrix is remodeled. Because collagen fibers are the main elastic scatterers in the ovarian stroma, the redistribution and re-organization of collagen fiber bundles affects its optical scattering properties. A non-invasive and sensitive micrometer-resolution instrument could potentially identify these structural alterations for early detection of ovarian cancer.

1.2 Optical Imaging and Computer-aided Diagnosis

Optical imaging can provide functional and structural information about biological tissues, with high resolution and without labels. Among optical modalities, optical coherence tomography (OCT) is a particularly well-established technique providing label-free high-resolution imaging with a penetration depth of a couple of millimeters [10]. OCT has already become a standard imaging modality in ophthalmology [11]. The use of intravascular OCT in investigating coronary atherosclerosis has grown exponentially, and it has shown potential for monitoring therapy [12]. One main advantage of OCT is that it can provide subsurface structure information in early neoplastic progression [13]. In addition, OCT can provide micro-scale real-time images without physically resecting the tissue. These advantages emphasize OCT's potential in early-stage diagnosis of colorectal and ovarian cancers.

Spatial frequency domain imaging (SFDI) is based on the diffuse optical propagation of light in the spatial frequency domain, which makes SFDI sensitive to both tissue absorption and scattering

[14]. Sinusoidal patterns of spatial frequencies with different phase shifts are projected onto the tissue surface and captured by a broadband camera over a large field of view. SFDI can provide quantitative optical characteristics of human tissues in real-time [15]. This method is low cost and label free, and it has numerous applications in dermatology, ovarian cancer, and colorectal cancer [16].

Computer-aided diagnosis (CAD) can assist in the analysis and classification of medical images by providing objective and quantitative interpolation. One notable success of CAD is using feature extraction and texture analysis technologies to register features/textures that are difficult to identify under visual inspection. Another success of CAD is using convolutional neural networks (CNN), whose outstanding performance in computer vision tasks has popularized deep learning for CAD imaging [17]. CNNs have been applied to OCT images for detecting ophthalmological and cardiac diseases [18] as well as for segmenting healthy esophagus layers *in vivo* [19]. CNN has also been applied to colon cancer diagnosis for imaging classification [20]. With recent advances in pattern recognition neural networks, it is possible to detect and localize certain objects from a single image [21], using a small training dataset.

1.3 Organization of the Dissertation

This dissertation is organized into seven chapters.

Chapter 1 provides the background and motivation of the current research, and introduces different optical imaging modalities and CAD techniques. **Chapter 2** first describes an automated image processing method for OCT images, then presents a customized feature for colorectal cancer diagnosis. In **Chapter 3**, OCT is combined with a pattern recognition neural network for assessing the structural differences between abnormal and normal colorectal tissues. **Chapter 4** presents a

feature engineering method based on tissue scattering information, which is derived from OCT images, for discrimination of different types of human colon tissues. The application of SFDI for multispectral discrimination of different types of human colon tissues is described in **Chapter 5**. **Chapter 6** presents OCT applications for ovarian cancer diagnosis using CAD technologies. Finally, **Chapter 7** summarizes of the current work and suggests future developments.

References

- [1] R.L. Siegel, K.D. Miller, and A. Jemal, *CA. Cancer J. Clin.* **2020**, 70, 7.
- [2] R.L. Siegel, K.D. Miller, and A. Jemal *CA Cancer J Clin.* **2019**, 69, 7.
- [3] J.S. Levine, and D.J. Ahnen, *N. Engl. J. Med.* **2006**, 355, 2551.
- [4] I.A. Issa, and M. Nouredine, *World J. Gastroenterol.* **2017**, 23, 5086.
- [5] S. Nandy, A. Mostafa, I. S. Hagemann, M. A. Powell, E. Amidi, K. Robinson, D. G. Mutch, C. Siegel, and Q. Zhu, *Radiology.* **2019**, 289(3):740-747.
- [6] L. A. Torre, B. Trabert, C. E. DeSantis, K. D. Miller, G. Samimi, C. D. Runowicz, M. M. Gaudet, A. Jemal, and R. L. Siegel, *CA Cancer J. Clin.* **2018**, 68(4):284-296.
- [7] J. R. van Nagell Jr., P. D. DePriest, M. B. Reedy, H. H. Gallion, F. R. Ueland, E. J. Pavlik, and R. J. Kryscio, *Gynecol. Oncol.* **2000**, 77(3):350-6.
- [8] T. R. Rebbeck, H. T. Lynch, S. L. Neuhausen, S. A. Narod, L. van't Veer, J. E. Garber, G. Evans, C. Isaacs, M. B. Daly, E. Matloff, O. I. Olopade, and B. L. Weber, *N. Engl. J. Med.* **2002**, 346(21):1616-22.
- [9] J. Prat, *Ann. Oncol.* **2012**, 23 Suppl 10:x111-7.
- [10] Y. Zeng, W. C. Chapman Jr., Y. Lin, S. Li, M. Mutch, and Q. Zhu, *J. Biophotonics.* **2021**, 14(1), e202000276.

- [11] J. Fujimoto, and E. Swanson, *Investig. Ophthalmol. Vis. Sci.* **2016**, 57, OCT1.
- [12] M. J. Gora, M. J. Suter, G. J. Tearney, and X. Li. *Biomed. Opt. Express.* **2017**, 8(5): 2405-44.
- [13] Y. Zeng, B. Rao, W. C. Chapman Jr., S. Nandy, R. Rais, I. Gonzalez, D. Chatterjee, M. Mutch, and Q. Zhu, *Sci. Rep.* **2019**, 9(1): 1-11.
- [14] D. J. Cuccia, F. P. Bevilacqua, A. J. Durkin, F. R. Ayers, and B. J. Troberg, *J. Biomed. Opt.* **2009**, 14(2): 024012.
- [15] S. Nandy, A. Mostafa, P. D. Kumavor, M. Sanders, M. Brewer, and Q. Zhu, *J. Biomed. Opt.* **2016**, 21(10): 101402.
- [16] S. Li, Y. Zeng, W. C. Chapman Jr., M. Erfanzadeh, S. Nandy, M. Mutch, and Q. Zhu, *J. Biophotonics*, **2020**, 13(6): e201960241.
- [17] A. Esteva, B. Kuprel, R. A. Novoa, J. Ko, S. M. Swetter, H. M. Blau, et al. *Nature.* **2017**, 542: 115–8.
- [18] A. Abdolmanafi, L. Duong, N. Dahdah, and F. Cheriet. *Biomed Opt Express.* **2017**, 8: 1203–20.
- [19] D. Li, J. Wu, Y. He, X. Yao, W. Yuan, D. Chen, et al. *Biomed Opt Express.* **2019**; 10: 1126–35.
- [20] G. Urban, P. Tripathi, T. Alkayali, M. Mittal, F. Jalali, W. Karnes, et al. *Gastroenterology.* **2018**; 155: 1069–78.
- [21] T. Y. Lin, P. Goyal, R. Girshick, K. He, and P. Dollár. In: Proceedings of the IEEE international conference on computer vision. **2017**.

Chapter 2: The Angular Spectrum Derived from the Scattering Coefficient Map Can Reveal Subsurface Colorectal Cancer

2.1 Background

Current standard of care for colorectal cancer is endoscopic screening, which relies on visual detection of surface abnormalities, and no subsurface quantitative information is provided. Often, early malignancies can be missed [1,2]. Multiple studies have demonstrated the survival advantages of screening and subsequent early intervention [3]. Therefore, to improve screening and surveillance of colorectal cancers, better screening and diagnostic imaging modalities are needed.

To address this need, we investigated the feasibility of using OCT for differentiating cancerous and normal human colon tissues. OCT's main advantage is providing subsurface structural and quantitative information in early neoplastic progression, when the colon undergoes subsurface architectural disruption that is invisible to the naked eye [4]. Previous studies have demonstrated OCT's ability for colon cancer diagnosis in mice colon tissues and *in vitro* human colon slides [5-7]. In this study, for the first time, we report an *ex vivo* study to reveal subsurface abnormalities in nine fresh human colon specimens using quantified subsurface scattering coefficient maps acquired by swept-source OCT (SSOCT). We automatically generate subsurface scattering coefficient maps OCT C-scans to provide a visualization of tissue optical properties. A 2-D Fourier transformation generates angular spectrums from scattering coefficient maps. An angular spectrum index (ASI) is derived to quantify the differences between the normal and abnormal tissues, and its strength in revealing subsurface cancer in *ex vivo* colorectal specimens is statistically analyzed.

These preliminary results demonstrate the feasibility of using quantified SS-OCT to identify early mucosal neoplasms within the human colon.

2.2 Method and Materials

In this section, we describe the colon specimen preparation, the SS-OCT system, the scattering coefficient mapping generation, the angular spectrum, and the ASI calculation.

2.2.1 Colon Specimen Preparation

Nine patients undergoing extirpative colonic resection at Washington University School of Medicine were recruited in our initial study. From these patients' operative specimens, we imaged and processed eight cancers, one pre-malignant polyp, and five representative areas with no gross abnormality. For each image of a specimen, we selected an area 10 mm x 20 mm and processed a region of interest for 3-D mapping of the scattering coefficients. This study was approved by the Institutional Review Board of Washington University School of Medicine, and informed consent was obtained from all patients. All samples were imaged immediately upon resection, prior to fixation in formalin.

2.2.2 SS-OCT System Setup

The SS-OCT system (Figure 2.1) is based on a swept source (HSL-2000, Santec Corp., Japan) with a 1310 nm center wavelength, 110 nm full width at half maximum bandwidth, and 20 kHz scan rate. The interference signal was detected by a balanced detector (Thorlabs PDB450C) and sent to a data acquisition board (ATS9462, Alazartec Technologies Inc). The lateral resolution of the system in air was 10 μm , and the axial resolution was 6 μm . To balance the effects of system

signal-to-noise ratio roll-off and Gaussian beam focusing, we performed a calibration test by measuring attenuated mirror signals from different imaging depths.

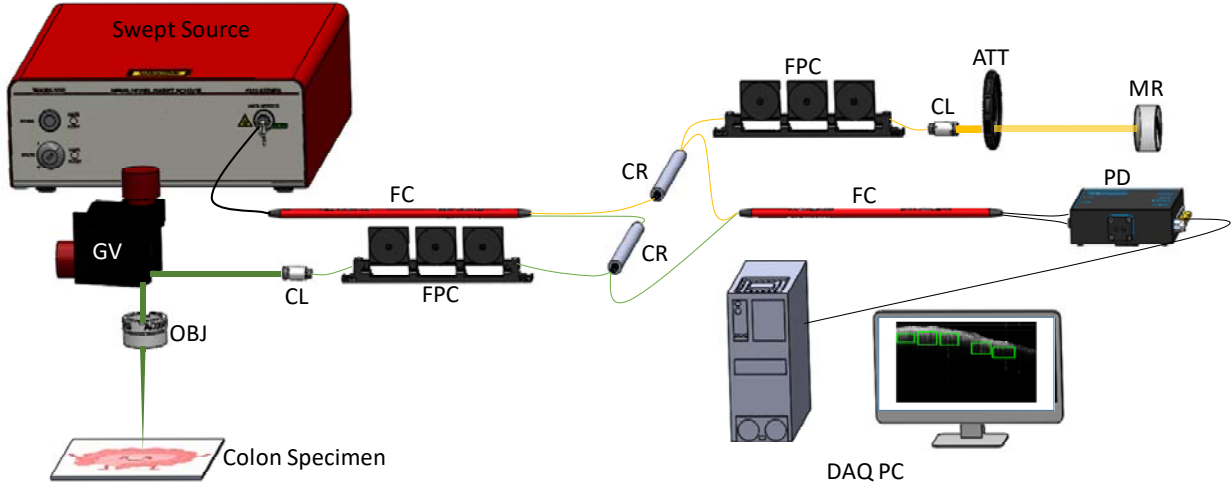


Figure 2.1 Homemade SS-OCT system. FC: fiber coupler, CR: circulator, FPC: fiber polarization controller, CL: collimator, ATT: attenuator, MR: mirror, GV: galvo mirror system, OBJ: objective lens, PD: photodetector, DAQ PC: data acquisition computer.

2.2.3 Automatic Image Surface Delineation

We model the surface delineation as an optimization problem. In physics, when travelling between two points, particles tend to follow the route that has the lowest potential energy. Here, we consider the tissue surface as the travelling path and establish a potential function $V(\mathbf{l})$ to derive it.

We first treat the SS-OCT image as a n -by- m matrix $I(n, m)$ with each entry represents the OCT signal. Then we use a 1 -by- m vector \mathbf{l} represents a possible path from the first column to the last column. The i th entry of \mathbf{l} is the row number of the path at the i th column and each entry has n possible values in this case. We establish the potential function $V(\mathbf{l})$ based on two observations: the detectable sample surface is generally continuous, and the surface has a higher OCT signals than surroundings especially under hyper-reflection situation. The $V(\mathbf{l})$ for the i th entry of \mathbf{l} is calculated as:

$$V(\mathbf{l}(i)) = C(i) + \alpha * Diff(i) + V(\mathbf{l}(i - 1))$$

where $C(i)$ stands for the continuity, $Diff(i)$ represents the signal gradient, and α is a custom defined scaling coefficient. $C(i)$ is defined as:

$$C(i) = |I(i) - I(i - 1)|$$

and $Diff(i)$ is calculated by the following equation:

$$Diff(i) = \sum_{j=I(i)-w}^{I(i)-1} I(j, i) - \sum_{j=I(i)}^{I(i)+w-1} I(j, i)$$

where w is the custom-defined window size to calculate the local gradient. Finally, we can find the surface \mathbf{s} by solving the optimization problem:

$$\mathbf{s} = \underset{\mathbf{l}}{argmin} V(\mathbf{l})$$

We use dynamic programming to realize this algorithm in MATLAB. In the study, we choose the window size as 15 and α as 0.01 for the best performance. The delineation result is shown in Figure 2.2.

2.2.4 Scattering Coefficient Mapping

The scattering coefficient within the colon epithelium layer was calculated by fitting each A-scan with a single attenuation model based on Beer's law [8-10]: $i(z) \propto \sqrt{\exp[-2\mu_t z]}$, where $i(z)$ is the OCT signal and the factor of 2 accounts for the round-trip attenuation. $\mu_t = \mu_a + \mu_s$ is the total absorption coefficient, which is the summation of the absorption coefficient μ_a and the scattering coefficient μ_s . Since in soft tissue μ_a is much less than μ_s , the fitted μ_t was used as a good approximation of μ_s .

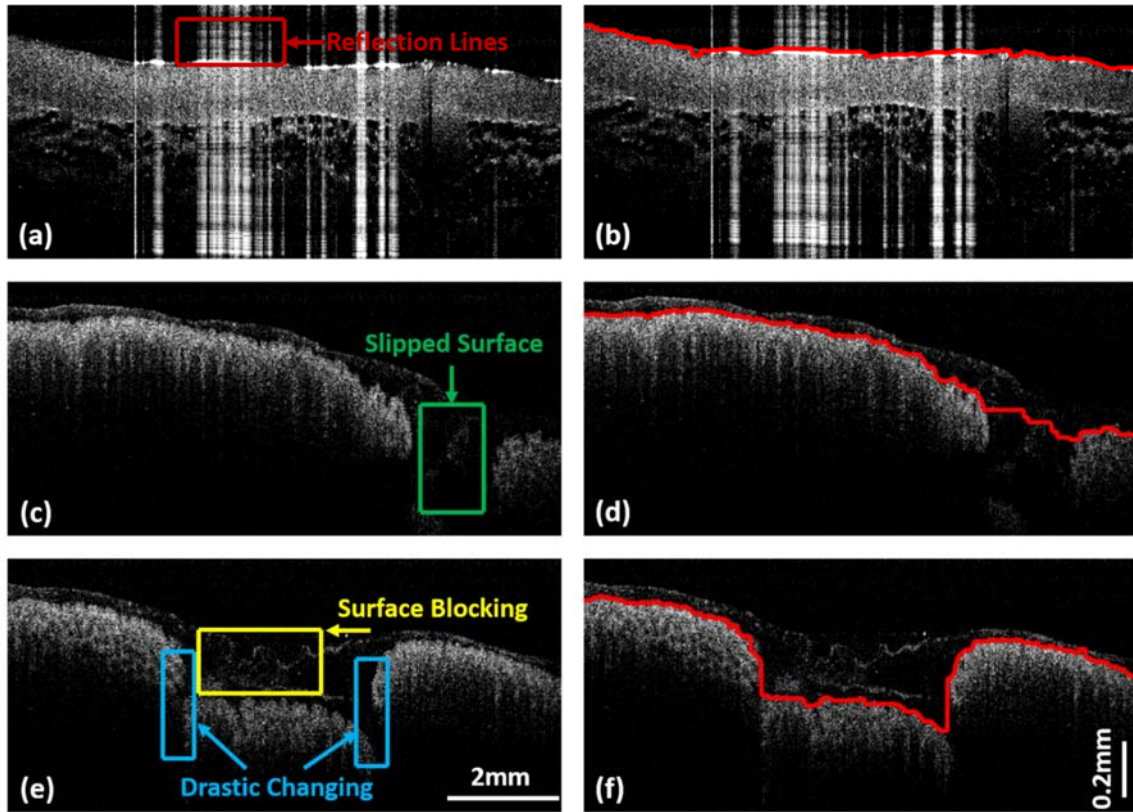


Figure 2.2 Surface detection of typical SS-OCT images with challenges. *Ex vivo* human colon SS-OCT images with hyper-reflection, surface discontinuation, surface blocking, and drastic changing are shown in (a), (c), and (e). (b), (d), and (f) show the corresponding surface detection result, respectively, after applying new automatic surface delineation method. Red line depicts the detected surface. All images share the same scale bar.

We automatically located the colon surface and then added a thickness to obtain the epithelium region. The area between the two red curves in Figure 2.3a and 2.3b identifies the colonic epithelium layer, and the curve fitting for one A-line from the de-noised signal is shown in Figure 2.3c and 2.3d. All A-lines within a B-scan are fitted. Afterwards we performed this fitting to consecutive B-scans, then generated an *en face* scattering coefficient map of the processed area.

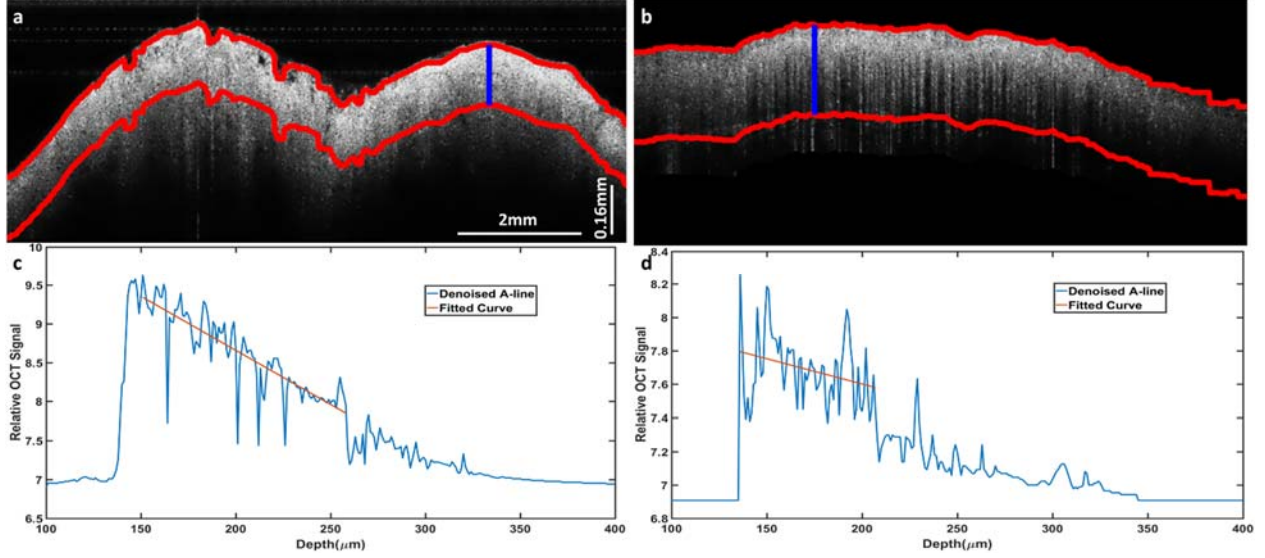


Figure 2.3 Scattering coefficient fitting. The colon epithelium layer is labeled between two red curves in the denoised B-scan SS-OCT image (**a.cancer**, **b.normal**). The scattering coefficient of the example A-line (blue) is fitted based on the quantification model, respectively (**c.cancer**, **d.normal**).

2.2.5 Angular Spectrum

One new image feature, extracted from the scattering map, is based on the observed differences between the normal and abnormal tissue scattering maps in terms of the spatial distributions. We first cropped the scattering maps to avoid out of focus or hyper-reflection areas. Then 2-D Fourier transform was used to reveal the angular spectrum of these maps.

A Sobel edge detection was performed in MATLAB to acquire a region with valid frequency information, and the border of the detected edges were fitted to an ellipse (ellipse 1) using the least squares criterion. The spatial frequency is derived as

$$f = \sqrt{f_{major}^2 + f_{minor}^2},$$

where f_{major} stands for the spatial frequency of the major axis and f_{minor} stands for the spatial frequency of the minor axis.

To further quantify the ASI, ellipse (ellipse 2) with a quarter of the area of ellipse 1 was used to depict the signal focused in the center region. Then, we defined the ASI as how much signal is outside the center:

$$ASI = \frac{all - inner}{all}$$

all = integration of all signals within ellipse 1

inner = integration of all signals within ellipse 2

We then took the average ASI of all cropped areas from one scattering map as the ASI of this map.

2.2.6 Data analysis

Statistical analysis was performed using MATLAB R2016a. The ASIs of normal and cancerous tissues were compared using student's t-test, and $p < 0.05$ was considered statistically significant.

2.3 Results

2.3.1 OCT images of normal and cancerous specimens

Representative SS-OCT B-scan images of normal colon tissues, cancerous tissues, and corresponding H&E slides are shown in Figure 2.4. The OCT and histologic images have the same scale and come from similar, but not identical, locations within the colon specimens. Figures 2.4a and 2.4b are representative OCT B-scan images from two normal specimens. A dentate line structure, which may correlate to the presence of a regular and well-organized crypt pattern in the epithelium, is observed in these images. These serrated edges in the OCT images correspond to the surface morphology shown in their histology results in Figures 2.4e and 2.4f.

However, the cancerous tissues present themselves differently in their OCT images, shown in Figures 2.4c and 2.4d. Significant surface erosions in cancer OCT images could be attributed to cancer invasions of the surface tissue. In the corresponding histology images (Figures 2.4g and

2.4h), the cancerous tissue appears highly irregular compared to the normal specimens, and shows a loss of normal colonic architecture.

2.3.2 Scattering coefficient maps of human colorectal specimens

We performed 3-D mapping of the scattering coefficients of the epithelium layer and then derived the ASI of each map, as described in the Methods section. Figures 2.5 and 2.6 show scattering coefficient maps from colorectal specimens of three patients and one corresponding histology result. The white areas are regions that are out of focus.

The *en face* scattering coefficient maps of the normal colons (Figs. 2.5b, 2.6d) contain a large area of homogenous scattering coefficients with periodic dot patterns, while the scattering coefficient map of cancer region (Figs. 2.5c, 2.6e) shows a large area of heterogeneous scattering coefficients. The normal map matches very well with the histological *en face* crypt structure, which is shown in magnification in Fig. 2.5d. The average dot-diameter (from eight random dots) is $67.88 \mu m$ in the scattering map and $69.75 \mu m$ in the histology, a very close match. The colon samples in Fig. 2.6 do not have such a close histological comparison because of the pathological process. The scattering distribution relates highly to the cancer's shape and inner structure. Since each colon cancer case can be pathologically different, there are no common features except for highly irregularity in the scattering coefficient maps of cancer tissues. Figure 2.6f shows the scattering coefficient map of a polyp that has been shown to be precancerous. The periodic pattern can hardly be visualized, and the map shows heterogeneity due to the abnormal growth.

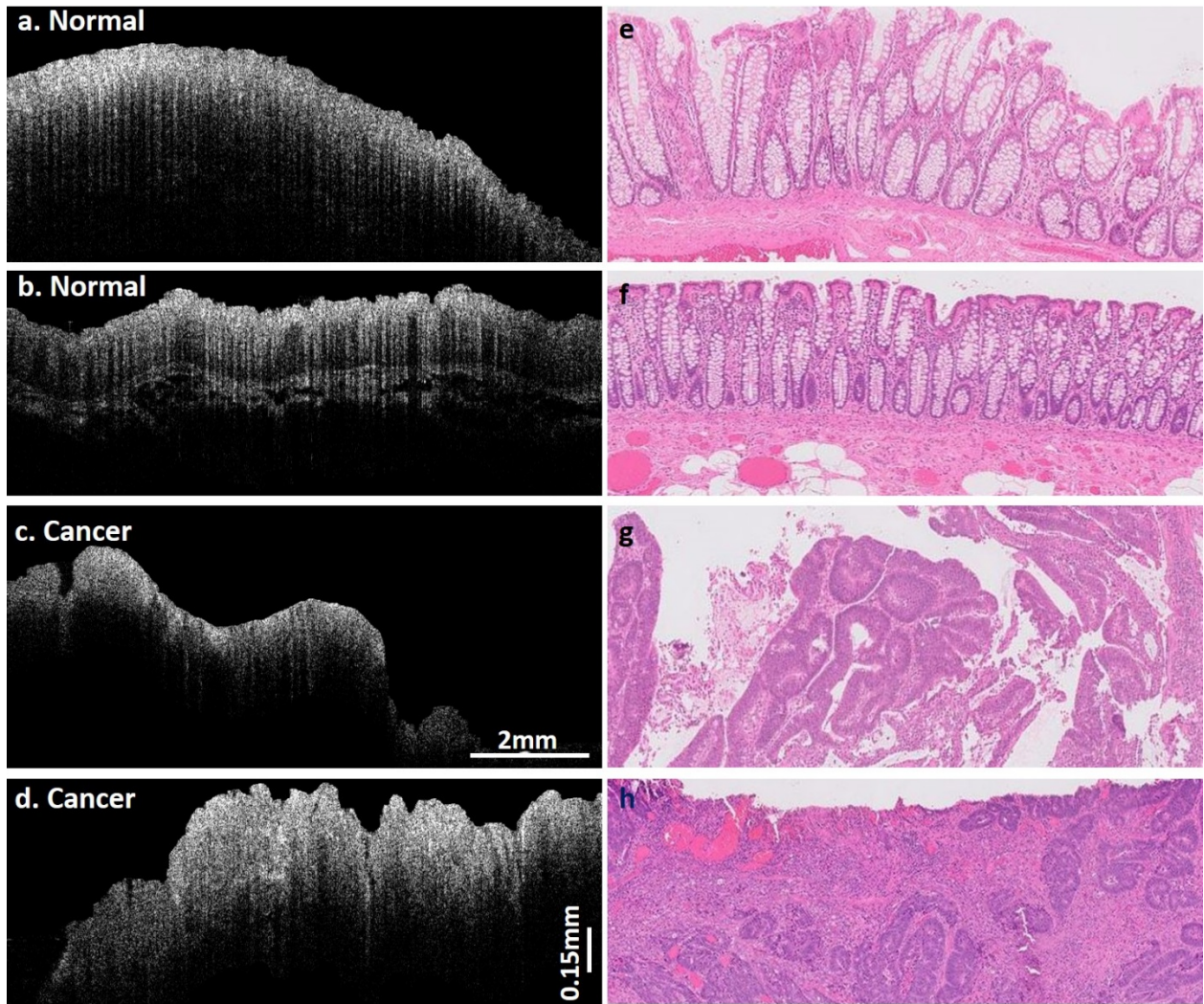


Figure 2.4 OCT images of normal and cancer colon specimens. **a** and **b** are typical normal tissue SS-OCT B-scan images from different patients. **e** and **f** are corresponding H&E slides. **c** and **d** are selected abnormal tissue SS-OCT B-scan images from the same patients as **a** and **b**, respectively. **g** and **h** are H&E slides of the same malignancy.

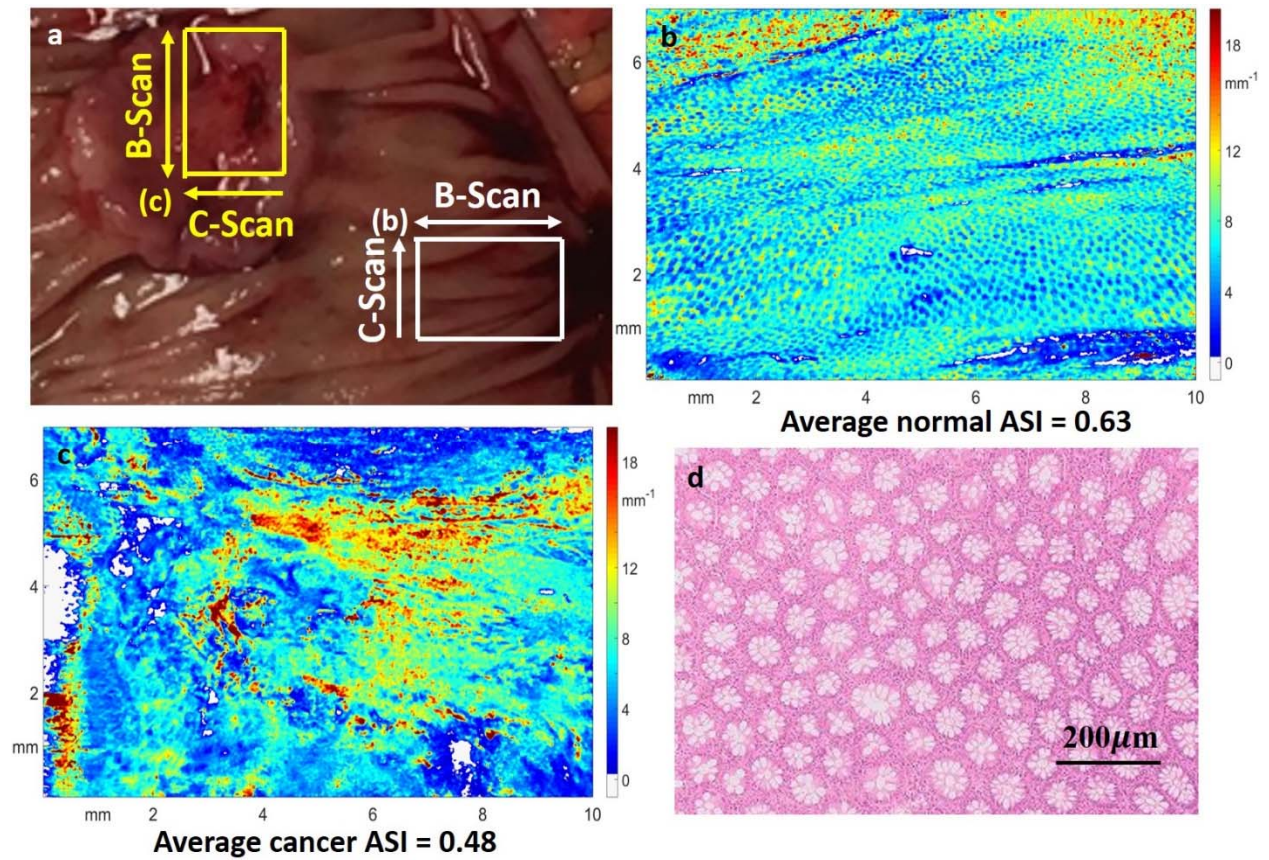


Figure 2.5 Scattering coefficient maps. **a** is a photograph of the colon specimen. The white box marks the imaged normal tissue area, while the yellow box delineates the processed malignant tissue. **b** is the scattering coefficient map from the normal tissue. **c** is the scattering coefficient map of the cancer. **d** illustrates the histological crypt structure of normal surface mucosa visualized in coronal cross section.

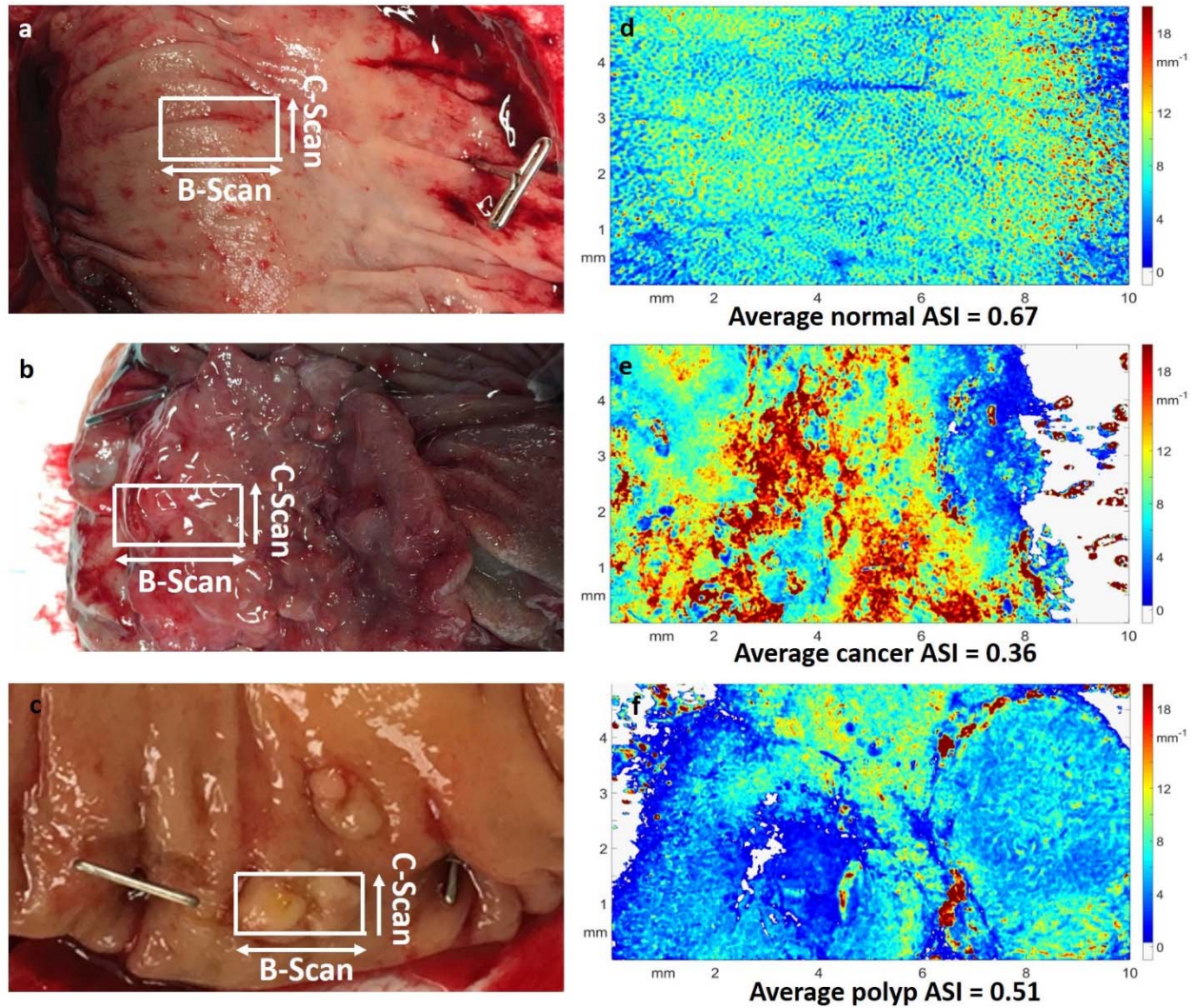


Figure 2.6 Scattering coefficient maps. **a** and **b** are gross photographs of normal and cancerous regions of one colon specimen, respectively. The white block approximately shows the processed area. **c** is a gross photograph of a polyp specimen, **d** shows the scattering map of the normal region, **e** is the scattering map of the cancer region, and **f** presents the polyp scattering map.

2.3.3 Angular spectrum analysis and its strength in revealing subsurface cancer

Nine colon specimens, including eight cancerous regions, five normal regions, and one pre-malignant polyp were successfully imaged and processed. The angular spectrum was acquired by applying 2-D Fourier transform to selected regions of the scattering coefficient maps, with the results shown in the left column of Figure 2.7. The right column of Figure 2.7 shows ellipses on top of angular spectra for quantification of ASI according to the Methods section. Specifically, we

use a Sobel edge detection method to find the area with valid signal, and then fit an ellipse using the least squares criterion (blue ellipses). Red ellipses are ellipses with quarter of the area of blue ellipses. While the blue ellipses include most of the scattering coefficient signals, the red ellipses enclose lower frequency components, corresponding to an inhomogeneous scattering coefficient distribution. Most high-frequency components, corresponding to a homogeneous and periodic scattering coefficient distribution, are outside of the red ellipse.

An angular spectrum ring between the red ellipse and blue ellipses can be observed only in the normal cases. The angular spectrum ring corresponds to clear separation between the frequency components of the homogeneous and periodic scattering coefficient distribution and the spatial frequency components of the inhomogeneous scattering coefficient distribution. From the histology result (Figure 2.5d), we calculated the average spatial frequency to be 12.93 mm^{-1} ; from the angular spectrum, we derived the average spatial frequency to be 11.89 mm^{-1} . Unfortunately, due to the pathological processing, we were not able to obtain histological results for other normal regions of imaged colon specimens. However, we estimate the range to be 9.41 mm^{-1} to 16.93 mm^{-1} based on other normal angular spectrums.

To measure the ring structure, the ASI was quantified by taking the ratio of the higher frequency components (integration of all signals in between the red and blue ellipse) to all frequency components (integration of all signals within the blue ellipse). This index separates five normal tissues from eight cancer tissues (Figure 2.8, p-value $\ll 0.001$). One polyp, which is a precancerous lesion, is also shown in Figure 2.8. It sits between the normal and cancerous tissues, which indicates a gradual structural change and the potential of using ASI to detect early stage colon cancer.

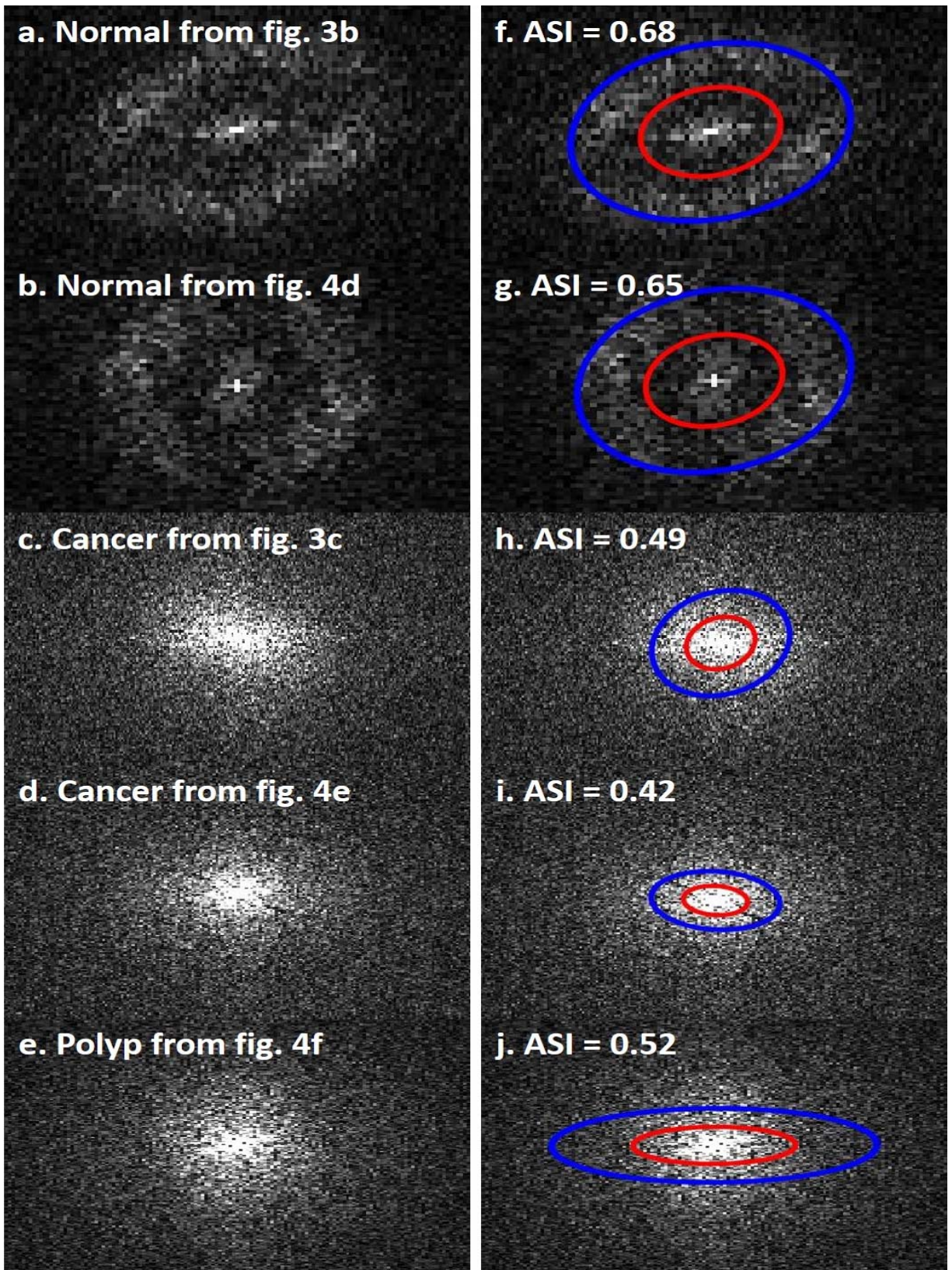


Figure 2.7. Angular spectrum images and their angular spectrum indexes quantified with a two-ellipse method.

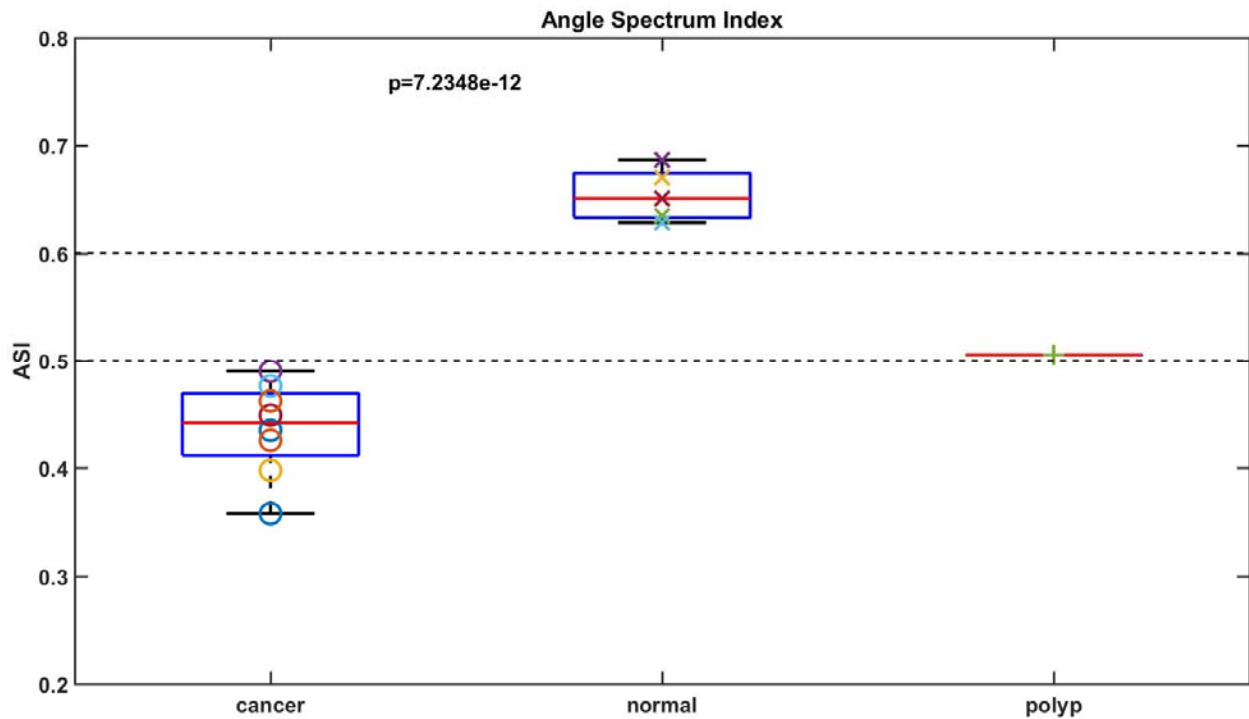


Figure 2.8. Angular spectrum index. Eight cancer tissues, five normal tissues, and one polyp are quantified. The p-value is between cancer and normal. The two dotted lines are used for visualizing the separation.

2.4 Discussion

In this pilot study, we evaluated the feasibility of qualitatively and quantitatively differentiating malignancies from normal colon tissue through optical coherence tomography (OCT). Scattering coefficient maps and angular spectrum analysis were calculated from OCT images generated from known malignant and normal tissue immediately after surgical resection. Qualitatively, 3-D scattering coefficient mapping of these specimens suggested unique subsurface microscopic optical scattering patterns that appear to differentiate malignant from normal tissue. Specifically, subsurface cancers destroy the homogenous crypt pattern seen in normal tissues and create random distributions. Quantitatively, angular spectra of the scattering maps demonstrate higher frequency components in normal tissues, shown as an angular spectrum ring pattern (Figure 2.7). Further

ASI quantification reveals the spatial frequency range of the normal crypt pattern, which significantly varies from ASI in cancerous tissues. Some highly scattering regions may look heterogeneous in normal scattering coefficient maps due to stronger scattering, e.g., the upper right portion of Figure 2.5b. We cropped and visualized this region separately and it shows a periodic pattern similar to normal regions. Moreover, we have quantified the ASI of this cropped area and it lies within normal tissue ranges.

Based on these findings, our system appears to differentiate organized normal colonic architecture from the irregular heterogeneous areas observed in malignant histology within this limited pilot study. Recent studies have shown that changes in crypt size and appearance are associated with the earliest forms of colorectal cancer [11,12]; therefore, OCT's ability to image the mucosal architecture in real time may lead to more sensitive assessment of early malignancies and improved detection of residual malignant tissue after chemotherapy and radiation treatment.

However, several technical limitations currently reduce the clinical efficacy of the specific system as described. All image post-processing is based on CPU running MATLAB. The total image post-processing time for a 5 mm by 1 cm (500 B-scans, 1000 A-lines/B-scan, and 1024 pixels/A-line) area is twelve hours on a Dell Inspiron 3650 (x64-based, Intel i5-6400 CPU @ 2.70GHz, 8GB RAM). To produce clinically relevant results, however, image processing and ASI quantification must be achieved in significantly shorter amounts of time. Future system improvements will therefore focus on GPU implementation and algorithm optimization to improve computational speed and accuracy. Then, *in vivo* study of system performance will be undertaken in an appropriately powered study to evaluate the clinical efficacy of this promising technology.

The data presented here suggest that OCT imaging may produce qualitative and quantitative information that differentiates malignant from normal tissue in the human colon. After

computational improvements and further testing, this system may augment traditional endoscopy when screening the large bowel for occult early malignancies or residual nests of cancer cells following initial oncologic therapy. Though promising, these preliminary results therefore warrant further study. Specifically, future efforts must focus on increasing the image processing speed and further evaluation of the scattering coefficient map and ASI quantification patterns *in vivo*.

2.5 Conclusion

We report the use of swept-source optical coherence tomography and a novel quantitative characteristic to differentiate malignant from normal tissue in nine fresh human colon specimens. Subsurface scattering coefficient maps were generated, and ASI were calculated for each imaged specimen. We found significant qualitative and quantitative differences between normal and malignant tissue. Among this limited sample, we demonstrated that the ASI varies significantly between normal and malignant tissue. While further system optimization and clinical testing are required, we conclude that SS-OCT may provide new diagnostic information when screening for early cancers or surveilling known disease following oncologic therapy. Future work will include system optimization to reduce image processing time, construction of an endoscopic device for further testing, and performance of an appropriately powered *in vivo* study to refine the accuracy of our system.

References

- [1] I.A. Issa, and M. Nouredine, *World J. Gastroenterol.* **2017**, 23, 5086.
- [2] J. M. Church, *Clinics in colon and rectal surgery*, **2005**, 18(3), 141.

- [3] D. E. Fleischer, B. F. Overholt, V. K. Sharma, A. Reymunde, M. B. Kimmey, R. Chuttani, K. J. Chang, *et al. Endoscopy*, **2010**, *42*, 781-789.
- [4] M. Fleming, S. Ravula, S. F. Tatishchev, and H. L. Wang, *J. Gastro. Oncol.*, **2012**, *3*(3), 153.
- [5] D. C. Adler *et al. Optics express*, **2009**, *17*, 784-796.
- [6] W. A. Welge, and J. K. Barton, *Lasers in surgery and medicine*, **2017**, *49*(3), 249-257.
- [7] H. K. Roy *et al. Gastroenterology*, **2004**, *126*(4), 1071-1081.
- [8] D. J. Faber, F. J. Van Der Meer, M. C. Aalders, and T. G. van Leeuwen, *Optics express*, **2004**, *12*, 4353-4365.
- [9] Y. Yang, *et al. Biomedical optics express*, **2012**, *3*(7), 1548-1556.
- [10] Y. Yang, *et al. Biomedical optics express*, **2011**, *2*, 2551-2561.
- [11] T. Tanaka. *Journal of carcinogenesis*, **2009**, *8*.
- [12] Y. Zeng, S. Xu, W. C. Chapman Jr., S. Li, Z. Alipour, H. Abdelal, D. Chatterjee, M. Mutch, and Q. Zhu. *Theranostics*, **2020**, *10*(6): 2587.

Chapter 3: Real-time colorectal cancer diagnosis using PR-OCT with deep learning

3.1 Background

In prior work, several research groups have demonstrated promising results that suggest OCT, an established high resolution imaging modality [1–5], may address the shortcomings of traditional camera endoscopy in the upper gastrointestinal tract [6-8] or large intestine [9-11]. OCT has been shown to accurately differentiate abnormal from normal tissue in multiple organs as an “optical biopsy” tool [12-15] in both murine and human colorectal models [16-19]. However, clinical application of the technology is complicated by the large volume of data generated and the subtle qualitative differences between normal and abnormal tissue. We hypothesize that computer aided diagnosis (CAD) may be valuable in adapting this modality to clinical applications.

The success of convolutional neural networks (CNN) in computer vision tasks has popularized deep learning for CAD imaging [20-22]. CNNs have been applied to OCT images for detecting ophthalmological and cardiac diseases [23-25] as well as segmenting healthy esophagus layers *in vivo*. Moreover, CNN has also been applied to colon cancer diagnostics in an image classification style [26-28]. Unfortunately, these methods require a large number of labeled training images, making them difficult to develop for clinical applications. Fortunately, recent advances on pattern recognition neural networks make it possible to detect and localize certain objects from a single image [29-31] using a small training dataset. These networks search for multiple patterns in each training image and allow PR-networks to be trained from fewer images as compared with older models. PR-networks have been previously explored in multiple setting, however, PR-networks paired with OCT have been unexplored in the colorectal cancer literature.

Here, we report the first study of PR-OCT in differentiating normal from neoplastic colorectal tissue. It is an OCT system trained by RetinaNet, a novel neural network architecture, for pattern recognition tasks. A dentate structural pattern has been utilized as a structural marker of normal specimens and used in PR-OCT prediction. Our method leverages the recent advancement in object detection, which localizes and classifies the diagnostic features at real-time, and achieves an accurate classification result. This initial study demonstrates the feasibility of using PR-OCT as an "optical biopsy" tool to assist doctors in real-time for mucosal neoplasms screening and treatment evaluation following initial oncologic therapy.

3.2 Materials and Methods

3.2.1 Colon specimen preparation

Patients undergoing extirpative colonic resection at Washington University School of Medicine were recruited prospectively into our study. Immediately following surgical resection, colon specimens underwent imaging of both normal bowel wall as well as areas of known abnormality. For each 3-D imaging task, several volumes of 10 mm x 20 mm x 1.6 mm or 5 mm x 10 mm x 1.6 mm were selected depending on the available time for the image task. Each imaged volume has one 3-D dataset for further data processing. Those scanned volumes were far from each other to preserve independence between data sets. This study was approved by the Institutional Review Board of Washington University School of Medicine, and informed consent was obtained from all patients. All samples were imaged within a one-hour period prior to fixation in formalin for routine pathological evaluation.

3.2.2 OCT image labeling and pattern marking

Prior to each imaging study, pathologists or surgical residents provided guidance to the researchers on the sample orientation and location of the examined tumor. Then OCT recorded several datasets accordingly. Each OCT image was labeled as “cancer”, “normal”, “adenomatous polyp”, “treated complete responder”, and “treated non-responder” based on the pathology record of each specimen. This manuscript focuses on identifying normal from malignant specimens, and the preliminary prediction result for other tissue types are also reported.

Two key imaging patterns were then marked to identify normal colonic mucosa from malignancies: “Teeth” and “Noise”. Literatures previously reported that normal colonic mucosa is associated with a dentate imaging structure, which we termed “Teeth” for this neural network [32]. The “Noise” category represents strong signals created by hyper-reflection and it has no association with any tissue signature. To train the network, we manually inspected each training B-scan image from both cancer and normal cohorts and marked the specific “Teeth” or “Noise” patterns using the `labelImg` toolbox. Four researchers were involved for annotating the boxes with a consistent criterion to avoid human bias. Since we detected the features based on the structure rather than the size of the features, we rescaled the input image to a size of 608×608 , which favors our network structure. The labeled coordinates were also transformed to be registered with the image accordingly. A typical labeled training image is illustrated in Figure 3.1A.

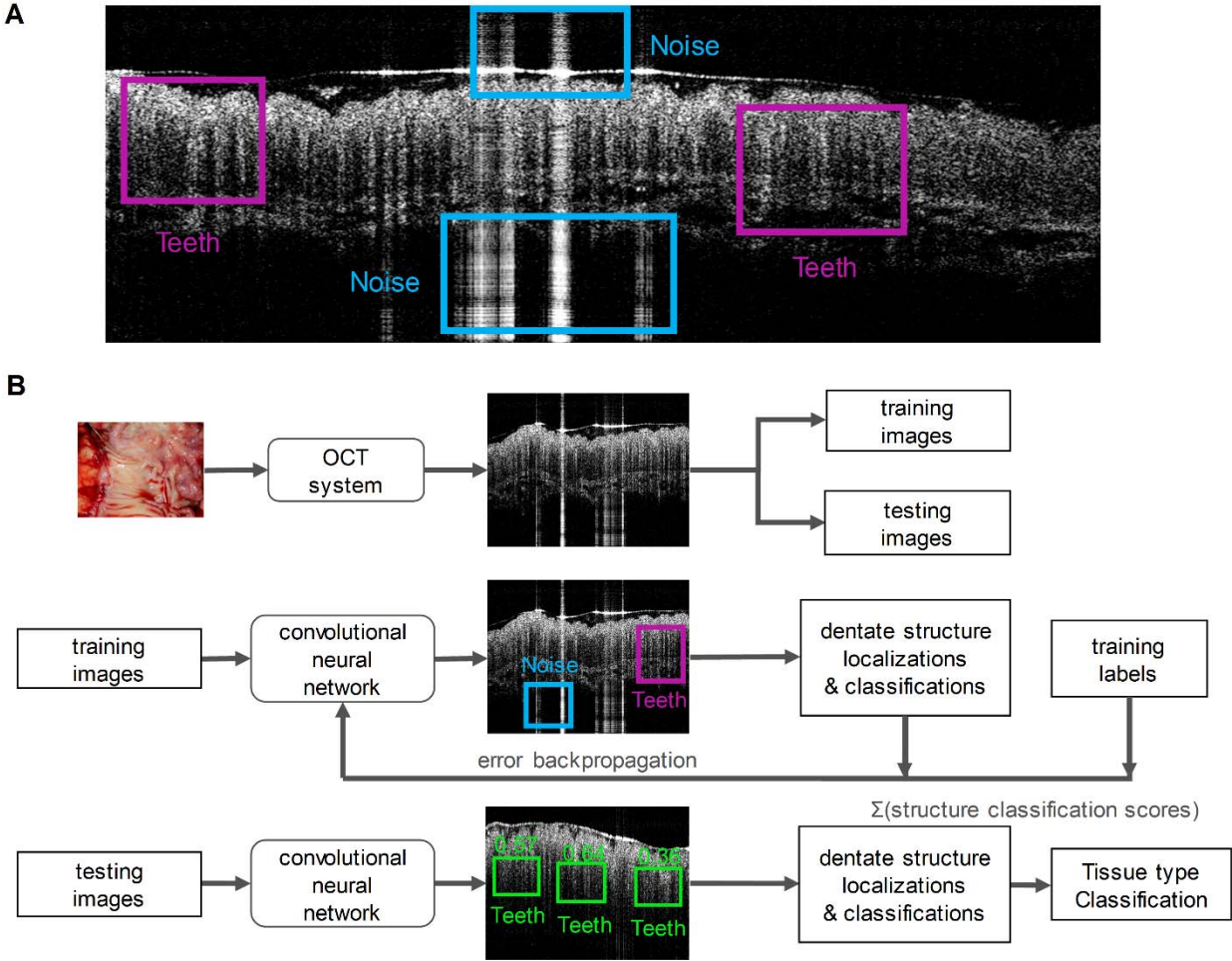


Figure 3.1 PR-OCT workflow. A. A training OCT B-scan image from a normal colon. Both “Teeth” and “Noise” classes are labeled with rectangular boxes shown in different colors; B. A flowchart summarizes the PR-OCT work flow: first, colorectal B-scan images were collected and separated into training and testing sets; second, “Teeth” and “Noise” patterns were labeled on training images and fed into the RetinaNet; finally, the trained model was tested on all testing images and the performance was evaluated.

3.2.3 Dense object detection with RetinaNet

We used a modified RetinaNet to detect structural patterns associated with normal or malignant tissue. The RetinaNet is composed of three parts: a backbone convolutional network that generates feature maps and two subnetworks that perform objection classification and bounding box regression. For our task, we used a feature pyramid network (FPN) backbone on top of a feedforward 18-layer ResNet. The feature maps generated from the backbone are then fed into a

convolutional subnetwork for object classification and boundary coordinates regression, as illustrated in Figure 3.2. Four anchors with two aspect ratios ($\{1:1, 1:2\}$) at two scales are used on each pyramid level. Each anchor is assigned with a 3-dimensional one-hot vector representing its class (background, teeth, or noise) and a 4-dimensional vector representing the coordinates of the upper left and lower right corners of the rectangular box that surrounds the objects. The classification is judged by the focal loss and the localization accuracy is evaluated with the robust smooth L1 loss. The network is trained for 80 epochs using the Adam solver. Though reported successful for many other CAD tasks, transfer learning techniques are not used here because empirically these methods degrade the performance for our study. We suspect this may be due to the mismatch between the OCT colon images and the nature photograph images. Thus we train the network from scratch using the labeled OCT images and the Xavier initialization.

After training, the model was tested on remaining unseen patients recruited later. During testing, once a pattern was detected in an OCT image, a score was given to estimate the probability of a correct prediction. Then the prediction results were used to classify the image as benign or neoplastic. For each input B-scan image, the RetinaNet provided a list of boxes along with its confidence (probability) belonging to every pattern class. The score for each B-scan image belonging to the normal class was calculated by summing the “Teeth” confidence value over all the boxes. Finally, we averaged the score over N sequenced OCT B-scan images. This score is used to represent the diagnostic result for the volume corresponding to these N images. Figure 3.1B summarizes the PR-OCT working flow in a flowchart.

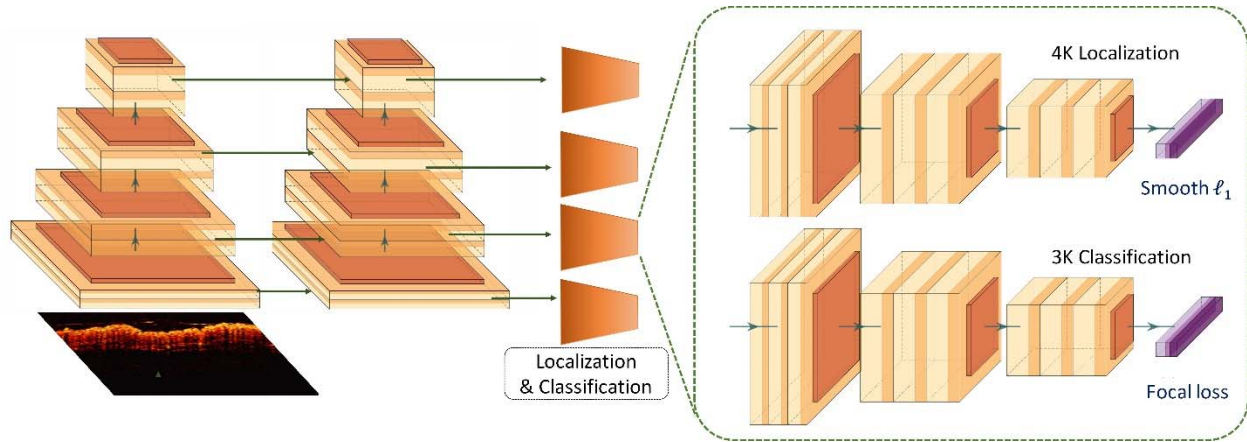


Figure 3.2 An illustration of RetinaNet. The left part is an FPN with a ResNet-18 backbone, and the right part are two sub-networks predicting the classifications and locations.

3.2.4 Statistical analysis

ROC curves were used for the evaluation of our model and the AUCs were used as a performance indicator. With the ground truth acquired from the histology, we categorized the system's prediction as true positive (TP), false positive (FP), true negative (TN), and false negative (FN). We denoted positive as predicting cancer and negative as predicting normal. True and false correspond to the presence of and the absence of a match with the histologic result, respectively. The sensitivity and specificity can then be calculated; from which we plot the ROC by computing the

$$\text{sensitivity} = \text{TP} / (\text{TP} + \text{FN})$$

and

$$1 - \text{specificity} = \text{FP} / (\text{FP} + \text{TN})$$

using different threshold values for the binary classification. The closer the ROC curve is to the upper left corner, the more accurate the neural network model has performed.

3.3 Results

3.3.1 Preparation of PR-OCT: establishing OCT dataset and training RetinaNet model

A total of 20 tumor areas, 16 normal areas, 2 adenomatous polyp areas, 2 treated areas from complete responders, and 2 treated areas from non-responders from 24 patients (mean age 69 years old, range: 53-91) were imaged and processed *ex vivo* from August 2017 to July 2019 in Washington University School of Medicine. Diagnoses were ascertained by subsequent surgical pathology examination. Details can be found in Table 3.1.

Table 3.1 Colorectal Lesion characteristics (patients' mean age 69 years old, range: 53-91)

Pathology reports	Number of imaged areas	Number of OCT images	Average OCT images per area	Median OCT images per area	Average imaged areas per patient	Median imaged areas per patient
Cancer	20	12550	628.4	600.0	1.1	1.0
Normal	16	8038	502.4	500.0	1.2	1.0
Adenomatous polyp	2	2500	1250.0	1250.0	1.0	1.0
Complete responder	2	1500	750.0	750.0	1.0	1.0
Non-responder	2	1500	750.0	750.0	1.0	1.0

In the training cohort of images, 838 labeled OCT images from 4 tumor areas and 4 normal areas acquired from 4 patients were included, where 2176 “Teeth” and 1875 “Noise” patterns were marked. We only used 4 tumor areas and 4 normal areas for training since the AUC of the ROC for our testing set did not improve too much as we included more areas in the training set. The remaining imaged areas, which were not seen by the trained model (from different patients), including 25,250 OCT images were categorized as the testing cohort.

3.3.2 Qualitative OCT imaging results

Distinct patterns were identified in normal colon tissues. Uniform crypt structures of normal colonic tissue created dentate structures within SS-OCT 3D-scanning images; likewise, the heterogeneous structure distribution of cancerous tissue yielded sparse dentate structures with little organized pattern. Representative images of normal colon tissues, cancerous tissues, and corresponding H&E slides are shown in Figure 3.3.

Figure 3.3A displays an *en face* image of a normal colon specimen formed by axial summation along the depth direction (z-dimension) of the entire 3D dataset for visualization. A clear crypt structure can be visualized as dot patterns in the image. When seen in cross-section (Figure 3.3B in XZ plane and Figure 3.3C in YZ plane), the uniform crypt structures create a dentate pattern that is replicated throughout normal colonic wall structure. Figure 3.3D shows an enlarged area in Figure 3.3A. Figure 3.3E is a representative *en face* histology image. The OCT and histology images have exactly the same size and come from similar, but not identical, location within the colon specimen. A microstructural *en face* crypt pattern can be clearly visualized in the enlarged area and it correlates well with the histology image. The average crypt diameter is $68\ \mu\text{m}$ in the enlarged area and $70\ \mu\text{m}$ in the *en face* histology, which suggests a close match. Note that tissue fixation as performed on standard pathologic processing results in some tissue shrinkage due to the removal of water from specimens. However, the degree to which this distorts measurements is difficult to assess and occurs more markedly on gross measurements than on microscopic ones. The degree of shrinkage also varies by tissue type; while renal tumors were found to shrink $\sim 10\%$ during fixation process, others have found that the majority of shrinkage occurs immediately after resection due to devascularization of the tissue. Since all measurements for this study were taken after resection, this may explain the similarities of size that we found between fresh *ex vivo*

measurements and those taken from histology slides after fixation. The photograph of the normal part of the colon specimen is displayed in Figure 3.3F for reference. Figure 3.3G shows the *en face* image of a cancerous colon specimen formed by axial summation. There is a heterogeneous structure distribution and the well-organized crypt pattern is broken. This may due to the neoplastic growth. When seen in cross-section (Figure 3.3H, 3.3I), no dentate line can be observed within those cross-sectional images.

3.3.3 Teeth pattern detection result

The trained RetinaNet was then tested on the testing cohort for pattern recognition purpose. Since the “Teeth” pattern is related to the normality of colon specimens, our network only predicted all “Teeth” patterns within the testing OCT images. Figure 3.4A-F display pattern recognition results from 6 typical OCT images. In normal cases (Figure 3.4A-B), the “Teeth” patterns are detected and marked by green boxes with the corresponding scores beside each box. However, no such pattern is detected in the cancerous case (Figure 3.4C). Figure 3.4D is the testing result of an adenomatous polyp. No “Teeth” pattern was detected. For the treated complete responders, the “Teeth” patterns come back as shown in Figure 3.4E. In contrast, no such pattern was detected in treated non-responders (Figure 3.4F). Only patterns with a score larger than 0.5 are shown for a better visualization. More tested normal and cancer cases can be found in respective Supplementary Video S1, Video S2, Video S3.

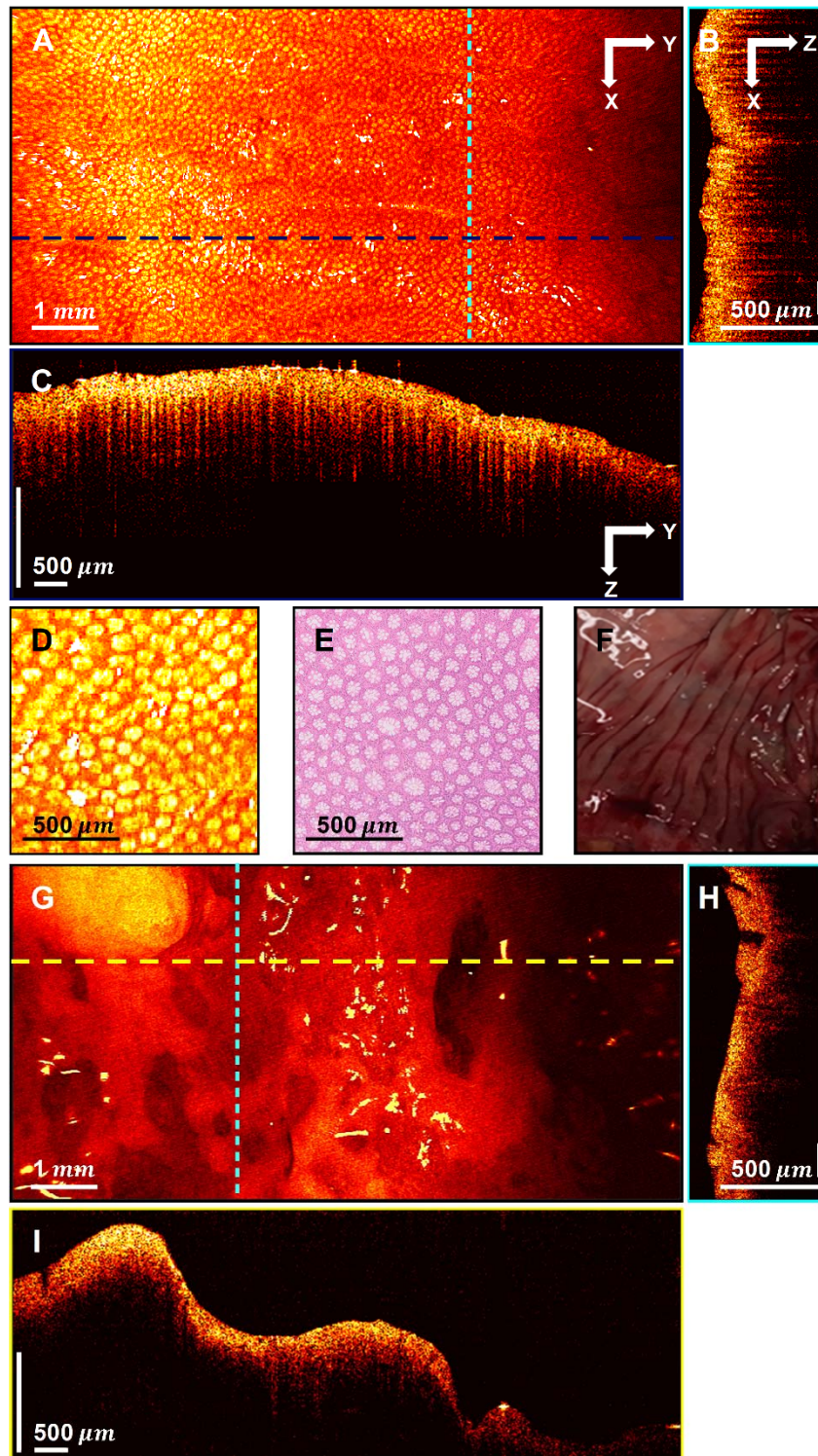


Figure 3.3 3D-OCT images of normal and cancerous human colon specimens. A. Normal specimen *en face* image constructed by axial summation; B. XZ cross-section of normal colon specimen; C. YZ cross-section image; D. Enlarged area of A; E. Representative *en face* histology; F. Photograph of a normal specimen; G. Cancerous specimen *en face* image constructed by axial summation; H. XZ cross-section of cancerous colon specimen; I. YZ cross-section image.

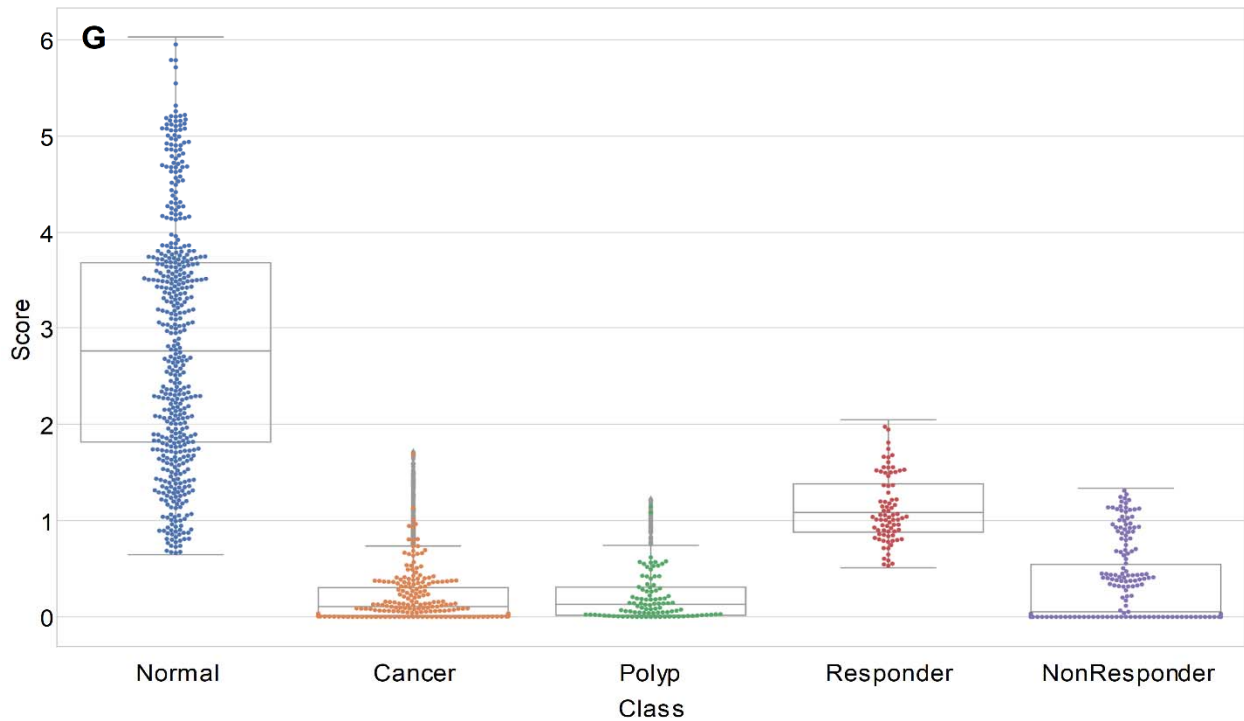
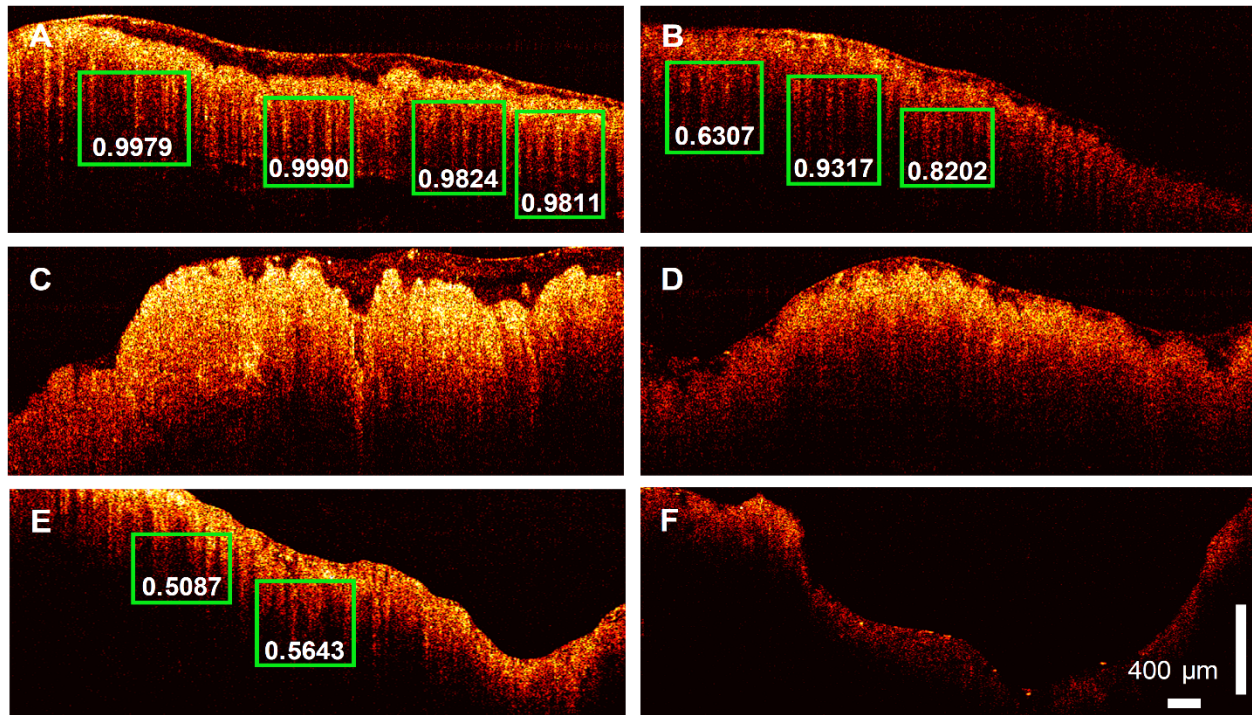


Figure 3.4 PR-OCT dentate pattern detection results for: A-B. normal colon images, green boxes are the predicted “Teeth” patterns and the corresponding scores are labelled on the bottom; C. cancer colon images; D. polyp colon images; E. treated complete responder colon images; F. treated non-responder colon images. G. A swarm plot on a box plot of prediction scores for normal, cancer, polyp, treated complete responder (Responder in the figure), and treated non-responder (NonResponder in the figure) colon specimens.

3.3.4 Identifying colon region with endogenous optical contrast

The identification results of tissue category using the trained neural network are displayed in Figure 3.4. During testing, N sequenced OCT B-scan images were used for tissue identification. In this report, N was heuristically chosen to be 40, as the AUC of the ROC improves slowly with the increasing of N. Figure 3.4G shows a swarm plot superimposed on a box plot of the prediction scores for the testing cohort. The median value of the normal ones (2.76) is noticeably higher than the cancer ones (0.11). For polyps, the median score is close to cancer (0.13). Treatment responders (median value: 1.08) show a distinct difference to non-responders (median value: 0.05). The treatment responder class has a score closer to normal specimen, and the non-responder class is closer to cancer tissue. The Cohen’s d between all scores of five tissue groups can be found in Table 3.2. Statistically, a larger d means a larger difference between two groups.

Table 3.2 Cohen’s d between all scores of five tissue groups

	Normal	Cancer	Polyp	Responder	Non-responder
Normal		3.34	2.47	1.47	2.16
Cancer			0.04	3.52	0.43
Polyp				3.62	0.44
Responder					2.20
Non-responder					

Figure 3.5 plots the ROC of the binary classification (normal vs. cancer) result. The true positive rate and the true negative rate are obtained by setting the threshold from 0 to 10. Note that the curve is plotted in the log-log scale because the AUC is very close to 1, which makes the linear scale plot indistinguishable from the boundary. A sensitivity of 100% and specificity of 99.7% can be achieved. The AUC of 0.998 is achieved in our study.

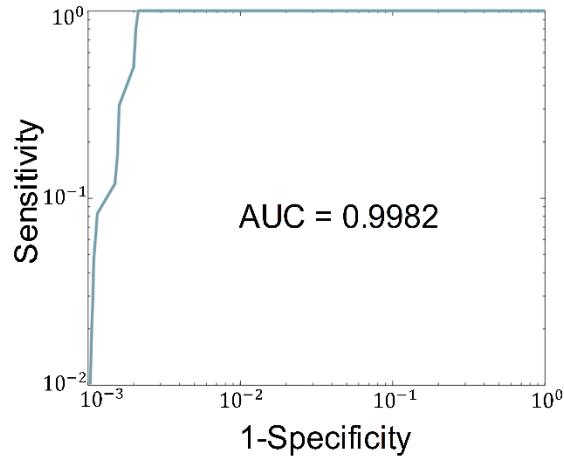


Figure 3.5 Plot of the ROC of the binary classification (normal vs. cancer) result. The AUC is labeled under the ROC.

Moreover, we have tested the classification time using different numbers of sequenced OCT images for identification. Using the CPU clock, a total time is calculated by recording the overall time cost to predict 2000 images using a batch size of N on a Nvidia Geforce GTX 1070 GPU. Then we report the classification time as the total time divided by $2000/N$. It took around 3.3 s for classifying 40 sequenced OCT images.

3.4 Discussion

This is the first report using a RetinaNet-based PR-OCT system to distinguish normal from neoplastic tissue within human colorectal specimens with real-time diagnosis capability. Using around 26,000 OCT images acquired from 20 tumor areas, 16 normal areas, 2 adenomatous polyp areas, 2 treated areas from complete responders, and 2 treated areas from non-responders, our system has achieved excellent performance. Quantitative scoring of the estimated probability of a normal specimen was used to evaluate performance. The accumulated scores from 40 sequenced OCT images were used for identification of tissue categories and its strength in differentiating cancer and normal in *ex vivo* specimens, with an AUC of 0.998 in 3.3 s.

Previously, a “Teeth” pattern was found as a landmark in OCT images of human normal colon due to the increased optical transmission through the normal crypt lumens [32]. Consistent results were found in this report. This dentate pattern was therefore used as the basis for tissue type prediction using the RetinaNet system. While we achieve a distinct classification between normal and cancer specimens, the preliminary test on polyps, treated complete responders, and non-responders is also a success. Recent studies have shown that changes in crypt size and appearance are associated with the earliest forms of colorectal cancer [33]; therefore, our PR-OCT may lead to more sensitive assessment of early malignancies and improved detection of residual malignant tissue after chemotherapy and radiation treatment.

Clinical translation of PR-OCT requires integration of the probe into the colonoscope for “optical biopsy” in real time during endoscopic evaluation. Several studies have demonstrated the feasibility of endoscopic OCT in both rodent and human models [6,7], especially, camera-guided endoscopic OCT [8,12]. Current screening methods for colorectal tissue rely on histologic evaluation of biopsy specimens, which take days to receive. With a classification time of only few seconds, PR-OCT shows a great potential to provide accurate real-time diagnosis. In addition, PR-OCT was tested on OCT images with different field of views (FoV) and the prediction power was similar. Though we assume the PR-OCT’s performance can generalize across different OCT systems, future efforts may focus on testing the performance on other OCT systems, i.e. spectral domain OCT. Therefore, suitable for serving as an “optical biopsy” tool to localize normal and malignant tissues with microscopic resolution. This can help guide more targeted biopsy. Once implemented into colonoscope, it can assist doctors during the colonoscopy procedure to potentially provide a high diagnostic accuracy of early malignancy.

Interestingly, we have achieved an accurate classification on a large amount of unseen testing data set with only limited training images. This is largely due to the training method employed in this study. Rather than throw images along with their classification labels, significant image patterns associate with normal specimens' structure have also provided to the network. In addition, a neural network designed for computer vision tasks is well suited for our objective – detecting one simple “Teeth” pattern in a grayscale image. Therefore, small amount of training data can yield a good prediction result in unseen images. Moreover, the powerful idea of introducing focal loss in RetinaNet dramatically improves the performance of the object detector under the condition of severely unbalanced classes (i.e., thousands of locations are evaluated by the detector, while only a few contain objects). Regarding object detection speed, RetinaNet also gives faster classification than its predecessors because it is a one-stage object detector.

One limitation of the study is the *ex vivo* nature of all imaged specimens. The human *in vivo* environment is likely more complex. For example, bowel movement, surgical adhesions, colonic strictures, etc. can cause difficulties in scanning and imaging. When fully developed, an OCT catheter will be delivered by colonoscope to the area of interest within the bowel. The system was tested on a very limited number of other abnormalities: 2 adenomatous polyp specimens. As the adenomatous polyp will potentially grow into cancer, it is promising that we got a lower predicting score which was close to cancerous tissue. Additionally, there are other colorectal abnormalities were not tested by PR-OCT, such as inflammatory bowel disease and hyperplastic polyp pathology. The ability to differentiate adenomatous from hyperplastic polyps would make a significant clinical impact. Since most biopsy-proven hyperplastic polyps will not undergo surgical resection due to the nature that they will not grow into malignancy, we did not encounter any patients with incidentally found hyperplastic polyps. We will need to test PR-OCT's ability to differentiate these

two types of polyps in future *in vivo* patient studies. Finally, the system was tested on a very limited number of tumors that had previously received radiation and chemotherapy treatment; though the result is promising, the number of specimen is limited. These devised lesions may require more categories in our PR-OCT classification design. It is also worth to mention that if the training sample is too small (i.e. one patient), the prediction power for abnormal lesions will drop as shown in Supplementary Figure S3. Future work includes training the network on an extended training set with more tissue abnormalities from a larger pool of patients.

In conclusion, the results presented suggest that PR-OCT may differentiate normal from cancerous colon rapidly, potentially enabling for real-time use. With further improvement, PR-OCT may enable "optical biopsy" of colorectal tissue in real time, which could direct diagnostic and therapeutic interventions to targeted areas of unusual mucosal growth. While the technology itself is not a direct treatment, one of its potential future applications is to assess the novel "wait and watch" rectal cancer treatment management strategy which allows treatment responders with no residual cancer left to be followed up safely by imaging rather than surgery and therefore preserves their quality of life. Though promising, these preliminary results warrant further study. Specifically, future efforts will include both hardware and software integration of PR-OCT into the endoscope, fine-tuning the network, and evaluation in the *in vivo* setting.

References

- [1] Huang D, Swanson EA, Lin CP, Schuman JS, Stinson WG, Chang W, et al. Optical coherence tomography. *Science*. 1991; 254: 1178–81.
- [2] Chen CL, Wang RK. Optical coherence tomography based angiography [Invited]. *Biomed Opt Express*. 2017; 8: 1056–82.

- [3] Pahlevaninezhad H, Khorasaninejad M, Huang YW, Shi Z, Hariri LP, Adams DC, et al. Nano-optic endoscope for high-resolution optical coherence tomography in vivo. *Nat Photonics*. 2018; 12: 540–7.
- [4] Katta N, Estrada AD, McElroy AB, Gruslova A, Oglesby M, Cabe AG, et al. Laser brain cancer surgery in a xenograft model guided by optical coherence tomography. *Theranostics*. 2019; 9: 3555–64.
- [5] Zhu M, Chang W, Jing L, Fan Y, Liang P, Zhang X, et al. Dual-modality optical diagnosis for precise in vivo identification of tumors in neurosurgery. *Theranostics*. 2019; 9: 2827–42.
- [6] Gora MJ, Quénéhervé L, Carruth RW, Lu W, Rosenberg M, Sauk JS, et al. Tethered capsule endomicroscopy for microscopic imaging of the esophagus, stomach, and duodenum without sedation in humans (with video). *Gastrointest Endosc*. 2018; 88: 830–40.
- [7] van der Sommen F, Curvers WL, Nagengast WB. Novel developments in endoscopic mucosal imaging. *Gastroenterology*. 2018; 154: 1876–86.
- [8] Ahsen OO, Lee HC, Liang K, Wang Z, Figueiredo M, Huang Q, et al. Ultrahigh-speed endoscopic optical coherence tomography and angiography enables delineation of lateral margins of endoscopic mucosal resection: a case report. *Therap Adv Gastroenterol*. 2017; 10: 931–6.
- [9] Kirtane TS, Wagh MS. Endoscopic optical coherence tomography (OCT): advances in gastrointestinal imaging. *Gastroenterol Res Pract*. 2014; 2014: 376367.
- [10] Gora MJ, Suter MJ, Tearney GJ, Li X. Endoscopic optical coherence tomography: technologies and clinical applications [Invited]. *Biomed Opt Express*. 2017; 8: 2405–44.
- [11] Welge WA, Barton JK. In vivo endoscopic Doppler optical coherence tomography imaging of the colon. *Lasers Surg Med*. 2017; 49: 249–57.

- [12] Panta P, Lu CW, Kumar P, Ho TS, Huang SL, Kumar P, et al. Optical coherence tomography: emerging in vivo optical biopsy technique for oral cancers. In: Panta P, Ed. Oral cancer detection: novel strategies and clinical impact. USA: Springer International Publishing AG; 2019: 217-37.
- [13] Freund JE, Faber DJ, Bus MT, van Leeuwen TG, de Bruin DM. Grading upper tract urothelial carcinoma with the attenuation coefficient of in-vivo optical coherence tomography. *Lasers Surg Med.* 2019; 51: 399–406.
- [14] Hariri LP, Mino-Kenudson M, Lanuti M, Miller AJ, Mark EJ, Suter MJ. Diagnosing lung carcinomas with optical coherence tomography. *Ann Am Thorac Soc.* 2015; 12: 193–201.
- [15] Zeng X, Zhang X, Li C, Wang X, Jerwick J, Xu T, et al. Ultrahigh-resolution optical coherence microscopy accurately classifies precancerous and cancerous human cervix free of labeling. *Theranostics.* 2018; 8: 3099–110.
- [16] Zagaynova E, Gladkova N, Shakhova N, Gelikonov G, Gelikonov V. Endoscopic OCT with forward-looking probe: clinical studies in urology and gastroenterology. *J Biophotonics.* 2008; 1: 114–28.
- [17] Adler DC, Zhou C, Tsai TH, Schmitt J, Huang Q, Mashimo H, et al. Three-dimensional endomicroscopy of the human colon using optical coherence tomography. *Opt Express.* 2009; 17: 784–96.
- [18] Li Y, Zhu Z, Chen JJ, Jing JC, Sun CH, Kim S, et al. Multimodal endoscopy for colorectal cancer detection by optical coherence tomography and near-infrared fluorescence imaging. *Biomed Opt Express.* 2019; 10: 2419–29.
- [19] Mavadia-Shukla J, Fathi P, Liang W, Wu S, Sears C, Li X. High-speed, ultrahigh-resolution distal scanning OCT endoscopy at 800 nm for in vivo imaging of colon tumorigenesis on murine models. *Biomed Opt Express.* 2018; 9: 3731–9.

- [20] Esteva A, Kuprel B, Novoa RA, Ko J, Swetter SM, Blau HM, et al. Dermatologist-level classification of skin cancer with deep neural networks. *Nature*. 2017; 542: 115–8.
- [21] Lu Y, Yu Q, Gao Y, Zhou Y, Liu G, Dong Q, et al. Identification of metastatic lymph nodes in MR imaging with faster region-based convolutional neural networks. *Cancer Res*. 2018; 78: 5135–43.
- [22] Litjens G, Kooi T, Bejnordi BE, Setio AAA, Ciompi F, Ghafoorian M, et al. A survey on deep learning in medical image analysis. *Med Image Anal*. 2017; 42: 60–88.
- [23] Lee CS, Baughman DM, Lee AY. Deep learning is effective for classifying normal versus age-related macular degeneration OCT images. *Ophthalmol Retina*. 2017; 1: 322–7.
- [24] Abdolmanafi A, Duong L, Dahdah N, Cheriet F. Deep feature learning for automatic tissue classification of coronary artery using optical coherence tomography. *Biomed Opt Express*. 2017; 8: 1203–20.
- [25] Hwang DK, Hsu CC, Chang KJ, Chao D, Sun CH, Jheng YC, et al. Artificial intelligence-based decision-making for age-related macular degeneration. *Theranostics*. 2019; 9: 232–45.
- [26] Chen PJ, Lin MC, Lai MJ, Lin JC, Lu HHS, Tseng VS. Accurate classification of diminutive colorectal polyps using computer-aided analysis. *Gastroenterology*. 2018; 154: 568–75.
- [27] Sirinukunwattana K, Raza SEA, Tsang YW, Snead DRJ, Cree IA, Rajpoot NM. Locality sensitive deep learning for detection and classification of nuclei in routine colon cancer histology images. *IEEE Trans Med Imaging*. 2016; 35: 1196–206.
- [28] Urban G, Tripathi P, Alkayali T, Mittal M, Jalali F, Karnes W, et al. Deep learning localizes and identifies polyps in real time with 96% accuracy in screening colonoscopy. *Gastroenterology*. 2018; 155: 1069–78.

- [29] Ren S, He K, Girshick R, Sun J. Faster R-CNN: towards real-time object detection with region proposal networks. In: Advances in neural information processing systems. 2015.
- [30] Lin TY, Goyal P, Girshick R, He K, Dollár P. Focal loss for dense object detection. In: Proceedings of the IEEE international conference on computer vision. 2017.
- [31] Redmon J, Farhadi A. YOLOv3: an incremental improvement. arXiv Prepr. 2018; arXiv: 1804.02767.
- [32] Zeng Y, Rao B, Chapman WC, Nandy S, Rais R, González I, et al. The angular spectrum of the scattering coefficient map reveals subsurface colorectal cancer. Sci Rep. 2019; 9: 2998.
- [33] Tanaka T. Colorectal carcinogenesis: review of human and experimental animal studies. J Carcinog. 2009; 8: 5.

Chapter 4: Diagnosing colorectal abnormalities using scattering coefficient maps acquired from optical coherence tomography

4.1 Background

Optical coherence tomography (OCT) is a high-resolution imaging technique that can probe about 1 mm into the surface[1–3], and it has been commercialized in ophthalmology and cardiology[4–7]. OCT has also been extensively studied as an “optical biopsy” tool for differentiating malignant tissue from abnormal/normal tissue in multiple organ systems[8–11]. Tissue optical scattering coefficient maps can be computed from OCT volumetric data, enabling quantification of early cancer morphological changes for diagnostic purposes. However, the OCT technique generates an enormous volume of data, which is slow and laborious to process manually. That’s why computer-aided diagnosis from OCT data, especially from within the GI tract, has garnered increasing interest in recent years.

Computer-aided diagnosis based on radiographic images requires feature extraction and texture analysis, and most features/textures are difficult to register under visual inspection. Texture analysis assumes that textural information is contained in the local gray-scale variations of an image[12]. Currently, its major medical applications are in oncology, such as automated tumor segmentation and grading, as well as in characterization of tumor heterogeneity[13]. Relevant oncological studies on PET[14], MRI[15], and CT[16] have demonstrated diagnostic results that are comparable to diagnoses from expert radiologists. Scale-invariant feature transform (SIFT) is an algorithm used in computer vision for object detection[17]. Unlike texture analysis, this algorithm detects local image descriptors that can be visually identified. It then quantifies these features by finding interest points, using Gaussian kernels with different scales. This algorithm has

been adopted in genetic analysis of colorectal cancer[18] and segmentation of kidney lesion areas in CT images[19].

In this *ex vivo* study of human colorectal cancer, we used swept-source OCT (SS-OCT) to acquire volumetric structural information about the colorectal tissue. Then the tissue scattering coefficient was computed using an algorithm developed in-house, generating scattering coefficient maps of the entire imaged region. An integral image algorithm, which reduced the processing time by 25%, was employed for image preprocessing. Regions of interest (ROIs) were manually selected from scattering maps and analyzed using a set of statistical texture features along with computer-vision related features. Significant features were selected based on feature importance, and a model with the reduced feature set was constructed to classify a tissue sample into normal tissue, cancerous tissue, or polyp. The results demonstrated the feasibility and potential for an alternative and improved way to differentiate colorectal tissue. To the best of our knowledge, this is the first report on using texture features and computer vision-based image features acquired from scattering coefficient maps to differentiate malignant, polypoid, and normal colorectal tissues.

4.2 Materials & Methods

4.2.1 Colon Specimen Preparation

Thirty-three patients (mean age, 66 years; range, 42-91; detailed characterizations in Table 4.1) undergoing extirpative colonic resection at Washington University School of Medicine were recruited to our initial study from August 2017 to February 2020. We studied one resected colorectal specimen from each patient. Among these specimens twenty-five were cancerous and four contained adenomatous polyps. We imaged one area per abnormality, i.e., twenty-five cancer areas and four adenomatous polyp areas. For imaging normal colorectal tissue regions, we used

two criteria to select the imaging area. First, if there were any abnormal growth in the resected tissue, the normal area needed to be at least 5 cm far from it. Second, only a single normal area per patient was evaluated. Using these selection criteria, twenty-six normal areas were imaged. The study protocol was approved by the Intuitional Review Board and informed consents were obtained from all patients. All samples were imaged within one hour after resection, and diagnoses were ascertained by subsequent pathology examination of the surgical specimen. Twenty-five cancer areas, twenty-six normal areas, and four adenomatous polyp areas were imaged.

Table 4.1 Characteristics of the studied colorectal patients

Histologic Examination	Number of patients	Age (mean \pm std)	Sex (% male)
Cancer	25	65 \pm 12	72 %
T1 adenocarcinoma	2	63 \pm 1	50 %
T2 adenocarcinoma	7	69 \pm 10	57 %
T3 adenocarcinoma	15	64 \pm 14	80 %
T4 adenocarcinoma	1	71	100%
Adenomatous polyp	4	70 \pm 8	50 %
Tubular adenoma	2	74 \pm 7	100 %
Tubulovillous adenoma	2	68 \pm 10	0 %
Normal	26	64 \pm 11	73 %

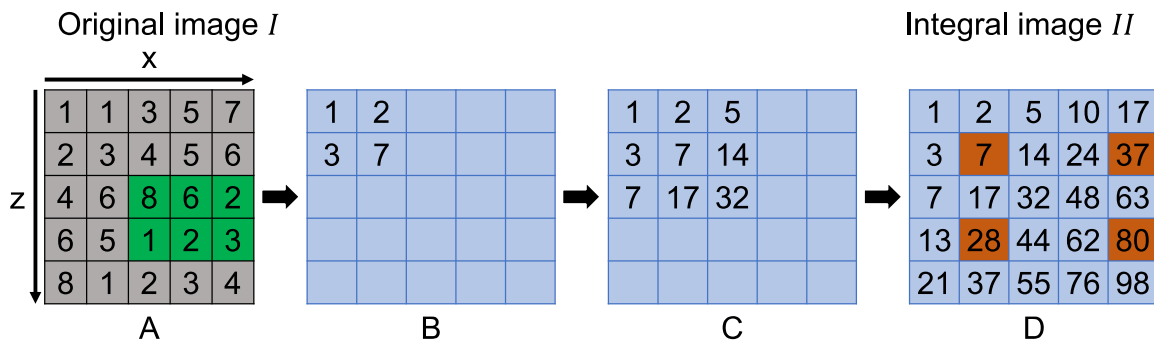
4.2.2 *en face* Scattering Coefficient Mapping

To generate the *en face* scattering coefficient map, we first automatically located the epithelium layer without any human intervention. Our surface detection algorithm will first read in a B-scan

image, and then output the coordinates of the surface of the epithelium layer. Adding a 1 mm depth, which is the typical mucosa thickness, the mucosa layer was extracted automatically. Formerly, this could take up to 14 hours for a 5 mm x 10 mm area, which corresponds to 500 B-scans with 1000 pixels by 1000 pixels per B-scan. In short, we formulated the surface delineation job as a global optimization problem. We created a matrix representation of each B-scan image named I , in which each entry $I(z, x)$ represented the intensity of pixel (z, x) . Here, x represented the lateral dimension and z was the depth dimension. We let \mathbf{l} represented a vector, with each entry $l(i)$ representing the imaged surface depth in each column of the image matrix. We optimized $V(\mathbf{l}(i)) = C(i) + \alpha * Diff(i) + V(\mathbf{l}(i - 1))$ to find the epithelium surface \mathbf{l} . The most computationally expensive aspect was calculating $Diff(i) = \sum_{j=l(i)-w}^{l(i)-1} I(j, i) - \sum_{j=l(i)}^{l(i)+w-1} I(j, i)$ for every pixel, where I is the OCT signal intensity and w is a custom-defined window size, for which we chose 10 pixels. Hence, for global optimization, we needed to calculate $n * n * 2w$ (i. e., $n * n * 20$) times, where n is the number of pixels within each B-scan. In this work, we introduce a preprocessing technique named integral image. As the name suggests, the value at any pixel (z, x) in the integral image is the sum of all the pixel intensities above and to the left of the pixel (z, x) , expressed as $II(z, x) = \sum_{z' \leq z, x' \leq x} I(z', x')$, where $I(z', x')$ is the intensity of the pixel (z', x') in the original image and $II(z, x)$ is the intensity of the pixel (z, x) in the integral image. Figure 4.1 shows an example of the integral image technique, proceeding from the original image to the integral image. Figure 4.1A is the original image intensity distribution: $I(z', x')$. Figure 4.1B shows the calculated values for the first four elements in the integral image. For example: $II(1, 2) = I(1, 1) + I(1, 2) = 1 + 1 = 2$; $II(2, 1) = I(1, 1) + I(2, 1) = 1 + 2 = 3$; $II(2, 2) = I(1, 1) + I(1, 2) + I(2, 1) + I(2, 2) = 1 + 1 + 2 + 3 = 7$. Figure 4.1C is one more step from Figure 4.1B: $II(2, 3) = I(1, 1) + I(1, 2) + I(1, 3) + I(2, 1) + I(2, 2) + I(2, 3) = 1 + 1 + 3 +$

$2 + 3 + 4 = 14$. Since we have information in those pixels which were already derived in the integral image, we can further simplify the calculation of $II(2, 3)$ to: $II(2, 3) = II(2, 2) + II(1, 3) - II(1, 2) + I(2, 3) = 7 + 5 - 2 + 4 = 14$. In general, it will take $n * n * 4$ computations to generate the entire integral image (Figure 4.1D). Once the integral image has been computed, evaluating the sum of intensities over any rectangular area requires only four pixels in the integral image, regardless of the area's size. Say the coordinates of the four vertices are $A = (z, x)$, $B = (z', x)$, $C = (z, x')$, and $D = (z', x')$. The sum of the pixel intensities over the rectangle $ABCD$ is $II(D = (z', x')) + II(A' = (z - 1, x - 1)) - II(B' = (z', x - 1)) - II(C' = (z - 1, x'))$. For example, to calculate the sum of the green area (vertices: $A = (3, 3)$, $B = (4, 3)$, $C = (3, 5)$, $D = (4, 5)$) in Figure 4.1A, we need just the four red pixels (vertices: $A' = (2, 2)$, $B' = (4, 2)$, $C' = (2, 5)$, $D = (4, 5)$) in Figure 4.1D: $8 + 6 + 2 + 1 + 2 + 3 = 22 = 80 + 7 - 28 - 37$. In practice, we performed zero padding to avoid boundary conditions. Therefore, the total computation time needed to calculate the $Diff(i)$ for every pixel is $n * n * 4 + n * n * (4 + 4 + 1) = n * n * 13$. Theoretically, a 35% reduction of computation time for calculating

L
 (



F
 P
 ir

Table 4.2 Surface detection time using different algorithms on various volumes of interest

Without integral image on a volume of 5 mm x 10 mm x 3 mm	With integral image on a volume of 5 mm x 10 mm x 3 mm	With integral image on a volume of 1 mm x 1 mm x 3 mm
47,989 s (13 hrs 19 mins 49 s)	35,831 s (9 hrs 57 mins 11 s)	700 s (11 mins 40 s)

After localization of the epithelium layer, scattering coefficients were extracted using Beer's Law and an *en face* scattering coefficient map was generated by applying this method to an OCT image volume. On each constructed *en face* scattering coefficient map, ROIs were manually selected for further quantitative analysis. Each ROI was 128 by 128 pixels, corresponding to 1.28 mm by 1.28 mm in physical dimensions. The final set of ROIs consisted of 121 normal regions, 84 malignant regions, and 24 adenomatous polyp regions.

4.2.3 Feature Extraction

Three sets of features were extracted from the ROIs: (1) six features extracted from the scattering maps, i.e., the mean scattering coefficient, median scattering coefficient, image entropy of the scattering map, and the 10th, 25th, and 75th percentiles; (2) nineteen texture parameters derived from the gray-level co-occurrence matrix (GLCM) of the scattering maps; and (3) four computer-vision based features acquired using SIFT, and one feature called the angular spectrum index (ASI). All feature extraction procedures were done in MATLAB 2019b.

The GLCM allows the calculation of texture features by describing the relationship among neighboring pixels within an image[30]. It measures how often different combinations of pixel intensities occur among neighboring pixels. To calculate the GLCM for each ROI, we first converted each ROI to a grayscale image. Then the GLCMs were generated for four directions, $\theta = \{0^\circ, 45^\circ, 90^\circ, 135^\circ\}$, assuming the distance between two neighboring pixels is 1. Then these

four matrices were averaged to generate the final GLCM, which is rotationally invariant to the intensity distribution.

We used the SIFT algorithm, a feature detection algorithm in computer vision, to locate points of interest[17]. The original image $I(x, y)$ was first convolved with a Gaussian kernel $G(x, y, k\sigma)$ at scale $k\sigma$:

$$L(x, y, k\sigma) = G(x, y, k\sigma) * I(x, y).$$

Then the differences of the Gaussians that occurred at multiple scales were calculated by

$$D(x, y, k\sigma) = L(x, y, k_i\sigma) - L(x, y, k_j\sigma).$$

Next, the algorithm used the differences as templates for pattern matching across each ROI, searching for interest points. Possible candidates were further screened using gradient and Hessian tests to remove edge points, and the number of interest points on each ROI was tallied. To characterize their distribution, the coordinate matrix of interest points was analyzed using principal component analysis, and the eigenvalues of the first two principal components were extracted. The relative difference between them was calculated to reflect the regularity of the interest points' distribution.

ASI is a feature which can evaluate whether there is a periodic structural pattern within an image. It first calculates the 2-dimensional fast Fourier transformation (2D FFT) of the image. After 2D FFT, a frequency spectrum of the image is generated. If there is a periodic structural pattern within the image, the frequency spectrum will show in higher spatial frequency band. ASI measures the ratio between higher spatial frequencies and all spatial frequencies. In general, normal colorectal tissues have a well-organized crypt pattern and the ASI is higher; while cancerous tissues are heterogeneous even in histopathological level and have a lower ASI.

4.2.4 Feature Selection & Image Classification

Feature selection is essential to avoid overfitting and to provide meaningful information from 25 features. Random forest (RF) is one of the most popular machine learning algorithms, as well as being a well-established feature selection algorithm. Feature selection using RF is categorized as an embedded method, offering the advantages of accuracy and generalizability. A random forest consists of hundreds of decision trees, and each node within a decision tree represents a rule for splitting data by using a single feature. The rule is based on Gini impurity (or information gain). When training a tree, we can compute how much each feature contributes to decrease the weighted impurity. In the sense of a random forest, we average the decrease in impurity caused by a single feature over all the trees to evaluate the feature's importance. According to their importance, we add features one-by-one to machine learning classifiers until an optimal dataset is found. A Python module, Scikit-Learn, was used for generating the feature importance.

Image classification was done in two phases. First, different machine learning classifiers were evaluated for differentiating abnormal tissues (cancers and adenomatous polyps) from normal tissues. Second, those classifiers were further tested on distinguishing cancerous tissues and adenomatous polyps. Two classifiers were evaluated, support vector machine (SVM) and RF. All features were normalized to avoid systematic biases. The evaluation of each model was based on the average performance from 100 repetitions of random train-test splits to minimize the randomness of single train-test splits. A train-test split for model fitting was defined as follows: the training set size was defined as $\frac{2}{3}$ of the smallest sample set, and then training data were chosen randomly from each diagnosis, while the rest were used for testing. Finally, the area under the receiver operating characteristic (ROC) curve (AUC) was used for determining both the optimal performance and the optimal feature sets of each model.

4.3 Results

4.3.1 *en face* Scattering Coefficient Maps

En face scattering coefficient mapping was performed on all OCT 3-D volumes. Figure 4.2A-C show representative scattering map ROIs from three different diagnoses. A is a ROI from normal tissue, within which a dotted pattern can be found. This pattern appears because the normal crypt pattern in the colon mucosa layer results in a crater structure in *en face* scattering maps. B and C are ROIs from an adenomatous polyp and cancerous tissue, respectively. Since abnormality growth breaks the crypt pattern and result in heterogeneous tissue distribution, no clear dotted pattern is found.

Figure 4.2D-F come from a special colorectal cancer case. Figure 4.2D is a photograph of this imaged tissue. The cancer area (green box) is flat and almost indistinguishable under visual inspection. This area was discovered using biopsy during colonoscopy since it was suspicious to an experienced endoscopist. It was also confirmed with following histopathology examination after OCT imaging. The histopathology slide is shown in Figure 4.2G. Figure 4.2E is a scattering map of the imaged area (blue box in Figure 4.2D). The distribution is heterogeneous and no dotted pattern can be found. The red box is a representative ROI, and Figure 4.2F shows an enlarged view of this area. Both the regular cancer (Figure 4.2C) and the flat cancer (Figure 4.2F) show a heterogeneous scattering coefficient distribution.

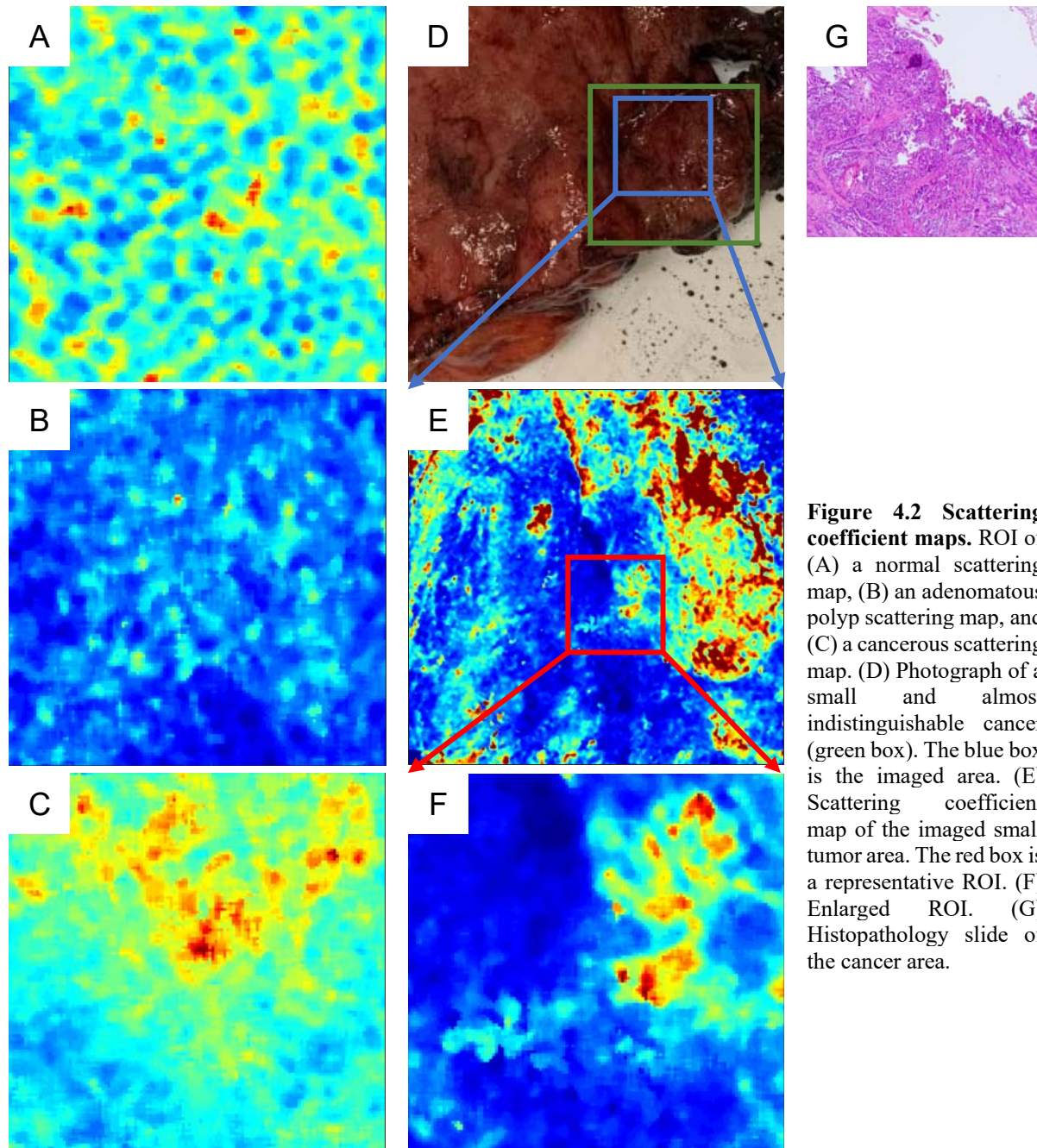


Figure 4.2 Scattering coefficient maps. ROI of (A) a normal scattering map, (B) an adenomatous polyp scattering map, and (C) a cancerous scattering map. (D) Photograph of a small and almost indistinguishable cancer (green box). The blue box is the imaged area. (E) Scattering coefficient map of the imaged small tumor area. The red box is a representative ROI. (F) Enlarged ROI. (G) Histopathology slide of the cancer area.

4.3.2 Feature Importance

Figure 4.3 and Figure 4.4 summarize the degrees of importance for each feature derived from the random forest classifier using Gini impurity. Figure 4.3 shows the relative individual importance of each variable included in the model differentiating malignant from normal tissue. Two

computer-vision based features, ASI and SIFT interest points, are the two most important features. This result is expected from the scattering map (Figure 4.2) since there is a unique image pattern within normal tissues. Likewise, Figure 4.4 displays the relative importance of the variables used in the model differentiating polypoid from cancerous tissues. Due to the lack of specific image patterns, texture features show higher importance among all features.

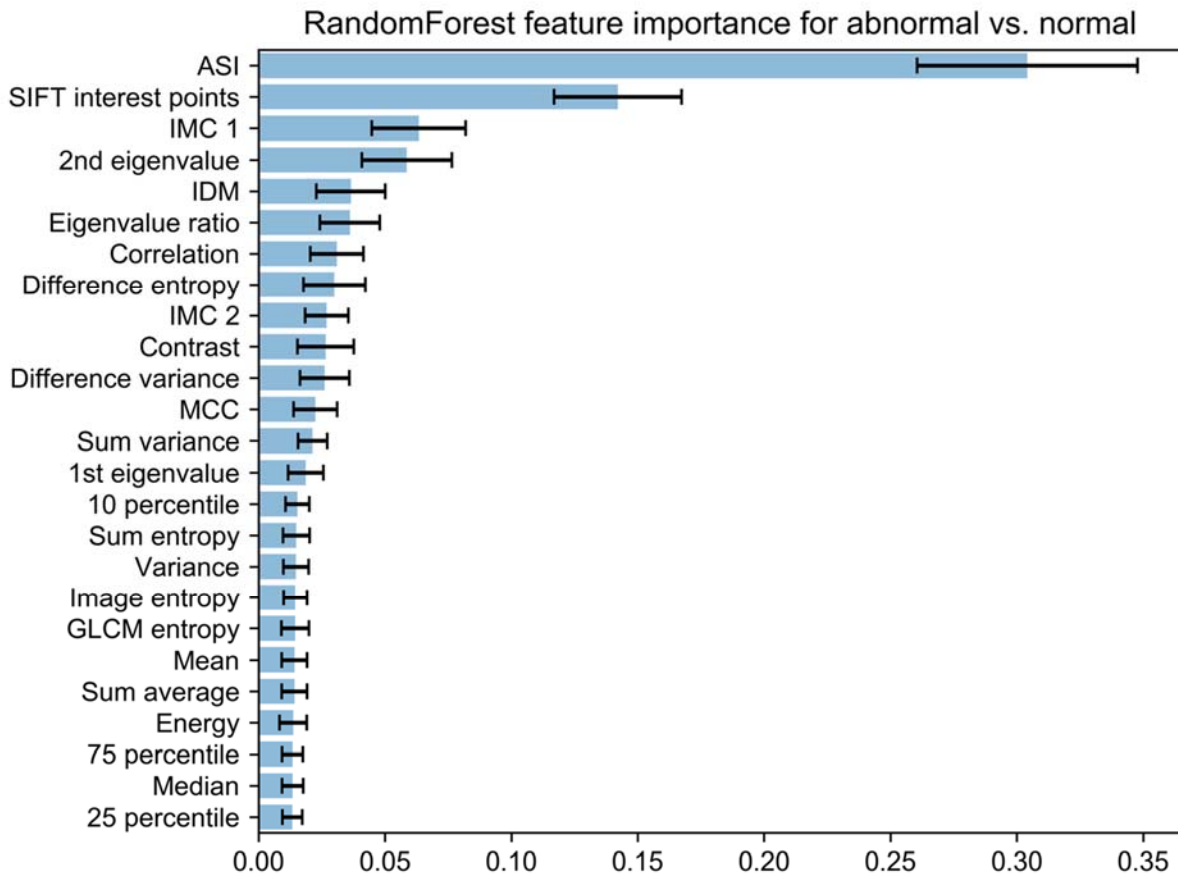


Figure 4.3 Feature importance for identifying abnormal tissue from normal tissue. ASI, angular spectrum index; IMC, information measure of correlation; IDM, inverse difference moment; MCC, maximal correlation coefficient.

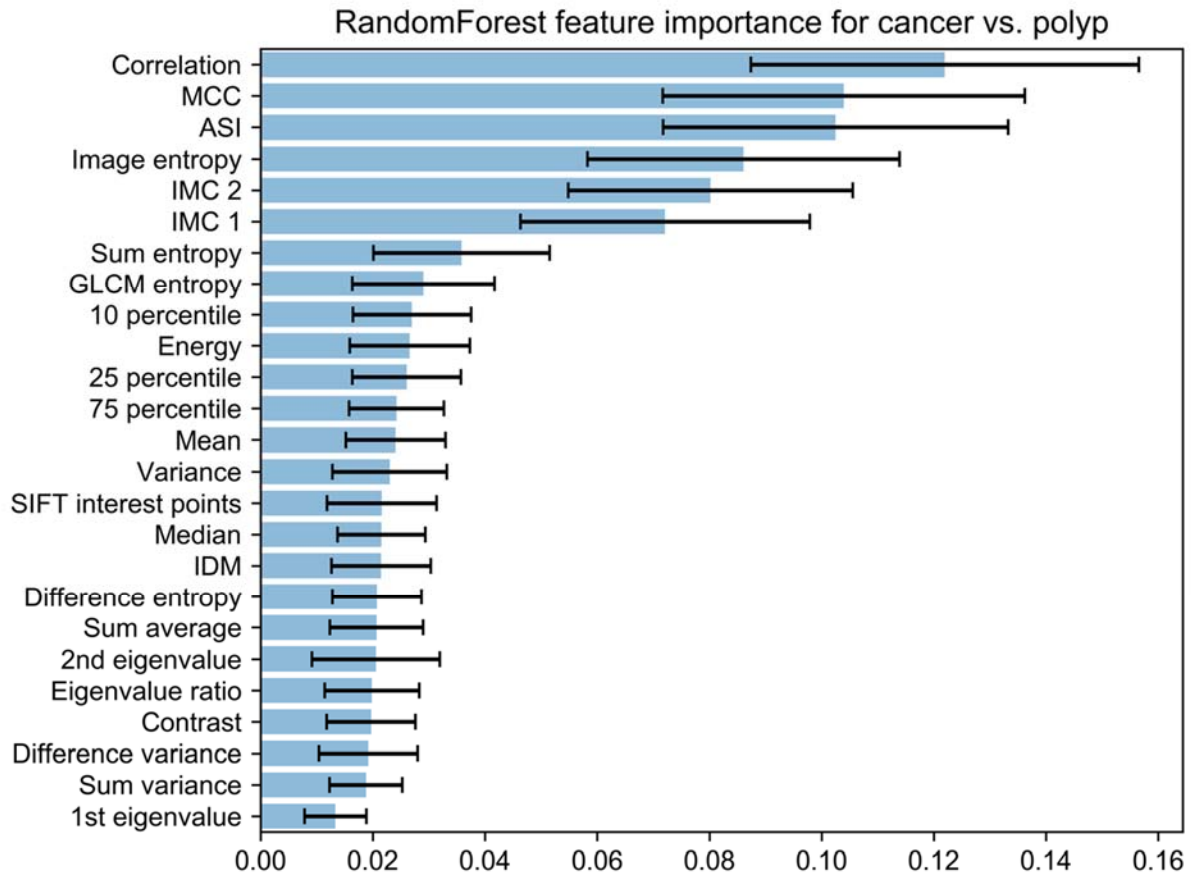


Figure 4.4 Feature importance for distinguishing adenomatous polyp from cancerous tissue. MCC, maximal correlation coefficient; ASI, angular spectrum index; IMC, information measure of correlation; IDM, inverse difference moment.

4.3.3 Image Classification

Table 4.3 shows the testing AUC of RF and SVM trained by different feature sets for distinguishing abnormal from normal tissue. The feature set starts with the most important feature, and adds other features one by one according to their importance rank. RF and SVM show similar trends, and they achieve optimal performance when three features are used. Adding more features does not increase the AUC. Trained by the optimal feature set, RF achieves an AUC, sensitivity, and specificity of 0.973, 90.0%, and 94.4%, whereas SVM does marginally better, with an AUC, sensitivity, and specificity of 0.984, 94.7%, and 94.0%. We conclude that ASI, SIFT interest points,

and IMC 1 form the optimal feature set, while SVM performs better in distinguishing abnormal from normal tissue.

Table 4.4 shows the testing AUC of RF and SVM trained by different feature sets for distinguishing adenomatous polyp from cancerous tissue. RF achieves an optimal performance when four features are used, and SVM achieves an optimal performance when six features are used. Trained by the optimal feature set, RF can achieve an AUC, sensitivity, and specificity of 0.913, 86.9%, and 85.0%, whereas SVM can achieve an AUC, sensitivity, and specificity of 0.892, 81.0%, and 84.8%. Therefore, we conclude that RF has a better performance in distinguishing adenomatous polyp from abnormal tissue, with an optimal feature set of Correlation, MCC, ASI, and Image entropy.

Table 4.3 Testing AUCs for distinguishing abnormal from normal tissue

Features	Random Forest AUC	SVM AUC
ASI	0.938	0.945
+SIFT interest points	0.970	0.981
+IMC 1	0.973	0.984
+2 nd eigenvalue	0.971	0.983
+IDM	0.972	0.985
+Eigenvalue ratio	0.972	0.984
All features	0.966	0.978

Table 4.4 Testing AUCs for distinguishing adenomatous polyp from cancerous tissue.

Features	Random Forest AUC	SVM AUC
Correlation	0.753	0.860
+MCC	0.836	0.863
+ASI	0.882	0.879
+Image entropy	0.913	0.882
+IMC 2	0.905	0.887
+IMC 1	0.906	0.892
+ Sum entropy	0.906	0.888
+GLCM entropy	0.905	0.878
All features	0.895	0.878

4.4 Discussion

This is the first report using texture features and computer vision-based image features acquired from scattering coefficient maps to differentiate malignant, polypoid, and normal colorectal tissue types. From 33 patients, 121 normal, 84 cancer, and 24 polyp ROIs were processed, and 25 features were then derived. Two classifications were assigned: abnormal tissue vs. normal tissue and adenomatous polyp vs. cancerous tissue. Based on the RF classifier using Gini impurity, the feature importance ranking for each task was calculated. Two classifiers, RF and SVM, were trained on

different feature sets according to the feature importance, and the optimal feature set was found based on the AUC. The results indicate that SVM with computer vision-based features (including ASI, SIFT interest points, and IMC1) is suitable for distinguishing abnormal and normal tissues, while RF with texture features (including Correlation, MCC, ASI, and Image entropy) shows better performance in identifying benign polyps.

When identifying abnormal and normal tissues, we found a specific dotted pattern related to the well-organized crypt pattern in the mucosa layer of the colorectal tissue. Studies have shown that changes in crypt size and appearance are associated with the earliest forms of colorectal cancer[20]. Figure 4.2D-F provide evidence that our scattering map approach can detect early colorectal cancer before it becomes visible with a normal endoscopic camera. Since this dotted pattern occurs only in normal tissues, computer vision-based features show great predictive importance because these features fit the morphology best. Both RF and SVM perform well. SVM is slightly better, possibly because separating abnormal and normal tissue is a relatively easier task, i.e., only three features are essential for a high accuracy.

In classifying adenomatous polyp and cancerous tissue, no distinguishing imaging pattern was found. Therefore, texture features are more important for accurate differentiation. Abnormalities in colorectal cancer are heterogeneous even at the histology level, which makes separating different types of abnormality a difficult non-linear problem. Texture features are more important for accurate differentiation under this situation because it provides a statistical measure of the intensity variation in space by evaluating a pixel's intensity with respect to its neighbors. By evaluating contrast, uniformity of energy, correlation, and homogeneity, texture features can reveal tissue functional properties beyond morphology. Since RF is designed for non-linear problems while SVM needs a suitable non-linear kernel to solve such problems, RF yields a better result in

this task. In a recent study using a deep-learning pattern-recognition method to classify OCT B-scans[44], we found that a very accurate diagnosis can be achieved for normal vs. cancer. However, there were limitations in effectively distinguishing polyp from cancer. Future study will focus on combining a feature-based method and a deep learning approach for a more accurate model.

Clinical translation of the scattering map requires integration of the probe into the colonoscopy for “optical biopsy” in real time during endoscopic evaluation. The application of OCT ancillary to endoscopy has been gaining momentum in recent years[21–23]. Integration of this technology into a colonoscope can facilitate investigation of several areas of study. First, such a device would enable *in vivo* imaging and testing. Since the eventual application of such technology would be in perfused tissue, testing it *in vivo* is key. However, we suspect that with minimal modifications, the machine learning algorithm will also function well, so long as it is trained with *in vivo* images. Second, colonoscopic imaging would allow investigation of the device’s performance with other benign pathologies of the colon, such as inflammatory bowel disease and hyperplastic polyps. The ability to differentiate adenomatous polyps from hyperplastic polyps would have a significant clinical impact. Because hyperplastic polyps are a benign growth and usually not resected, an *in vivo* approach is essential to imaging such abnormalities. Certainly, more training samples from all types of abnormalities can improve the machine learning model. A large data base can enable us exploring more complicated training models that best suit the colorectal cancer diagnosis task. Additionally, we believe combining texture features from *en face* scattering maps and B-scan images can potentially help discriminate polyps and cancer, because scattering maps contain functional information of macro-structures (i.e. from an image volume) and B-scan images carry morphology micro-structure information.

In addition, real-time data processing is also crucial for “optical biopsy”. We improved our image processing speed by 25% with the usage of integral image. At present, it takes around 11 minutes to generate an *en face* scattering map for a 1 mm x 1 mm area. Certainly, this is faster than obtaining biopsy results (at least one day), but it remains too slow to facilitate bedside decision-making. Migrating the data processing platform to a GPU using parallel processing is one possible solution that should be investigated in the future. Another possible solution is using a deep learning based surface detection method. This method can predict the surface within seconds after the deep learning model is well-trained. However, the ground truth has to be labeled manually and the training process is in general time-consuming.

Based on these results, we conclude that the scattering map derived from OCT images can provide qualitative and quantitative information which demonstrates the potential for aiding the diagnosis of human colorectal tissues. *In vivo* study is needed to validate the performance of our machine learning model. With further improvement, the scattering map may guide physicians during colonoscopy for early cancer screening and biopsy site selection. Future efforts will focus on the real-time image processing algorithm and integrating the OCT system into a clinical endoscope.

References

- [1] K.C. Zhou, R. Qian, S. Degan, S. Farsiu, and J.A. Izatt, *Nat. Photonics* 2019, 13, 794.
- [2] Z. Dong, G. Liu, G. Ni, J. Jerwick, L. Duan, and C. Zhou, *J. Biophotonics* 2020, 13, e201960135.
- [3] H. Zhou, Y. Dai, G. Gregori, P.R. Rosenfeld, J.L. Duncan, D.M. Schwartz, and R.K. Wang, *Biomed. Opt. Express* 2020, 11, 1834.
- [4] B.E. Bouma, M. Villiger, K. Otsuka, and W.-Y. Oh, *Biomed. Opt. Express* 2017, 8, 2660.

- [5] J. Fujimoto, and E. Swanson, *Investig. Ophthalmol. Vis. Sci.* 2016, 57, OCT1.
- [6] Y. Gan, T.H. Lye, C.C. Marboe, and C.P. Hendon, *J. Biophotonics* 2019, 12, e201900094.
- [7] X. Zhang, L. Beckmann, D.A. Miller, G. Shao, Z. Cai, C. Sun, N. Sheibani, X. Liu, J. Schuman, M. Johnson, T. Kume, and H.F. Zhang, *Invest. Ophthalmol. Vis. Sci.* 2020, 61, 23.
- [8] E. Shostak, L.P. Hariri, G.Z. Cheng, D.C. Adams, and M.J. Suter, *J. Bronchol. Interv. Pulmonol.* 2018, 25, 189.
- [9] K.M. Meiburger, Z. Chen, C. Sinz, E. Hoover, M. Minneman, J. Ensher, H. Kittler, R.A. Leitgeb, W. Drexler, and M. Liu, *J. Biophotonics* 2019, 12, e201900131.
- [10] Y. Zeng, S. Nandy, B. Rao, S. Li, A.R. Hagemann, L.K. Kuroki, C. McCourt, D.G. Mutch, M.A. Powell, I.S. Hagemann, and Q. Zhu, *J. Biophotonics* 2019, 12, e201900115.
- [11] R.M. Juarez-Chambi, C. Kut, J.J. Rico-Jimenez, K.L. Chaichana, J. Xi, D.U. Campos-Delgado, F.J. Rodriguez, A. Quinones-Hinojosa, X. Li, and J.A. Jo, *Clin. Cancer Res.* 2019, 25, 6329.
- [12] R.M. Haralick, K. Shanmugam, and I. Dinstein, *IEEE Trans. Syst. man Cybern.* 1973, 6, 610.
- [13] P. Lambin, E. Rios-Velazquez, R. Leijenaar, S. Carvalho, R.G.P.M. Van Stiphout, P. Granton, C.M.L. Zegers, R. Gillies, R. Boellard, A. Dekker, and H.J.W.L. Aerts, *Eur. J. Cancer* 2012, 48, 441.
- [14] V. Giannini, S. Mazzetti, I. Bertotto, C. Chiarenza, S. Cauda, E. Delmastro, C. Bracco, A. Di Dia, F. Leone, E. Medico, A. Pisacane, D. Ribero, M. Stasi, and D. Regge, *Eur. J. Nucl. Med. Mol. Imaging* 2019, 46, 878.
- [15] A. Wibmer, H. Hricak, T. Gondo, K. Matsumoto, H. Veeraraghavan, D. Fehr, J. Zheng, D. Goldman, C. Moskowitz, S.W. Fine, V.E. Reuter, J. Eastham, E. Sala, and H.A. Vargas, *Eur. Radiol.* 2015, 25, 2840.

- [16] H.J.W.L. Aerts, E.R. Velazquez, R.T.H. Leijenaar, C. Parmar, P. Grossmann, S. Cavalho, J. Bussink, R. Monshouwer, B. Haibe-Kains, D. Rietveld, F. Hoebbers, M.M. Rietbergen, C.R. Leemans, A. Dekker, J. Quackenbush, R.J. Gillies, and P. Lambin, *Nat. Commun.* 2014, 5, 4006.
- [17] J. Cruz-Mota, I. Bogdanova, B. Paquier, M. Bierlaire, and J.P. Thiran, *Int. J. Comput. Vis.* 2012, 98, 217.
- [18] P. Broderick, T. Bagratuni, J. Vijaykrishnan, S. Lubbe, I. Chandler, and R.S. Houlston, *BMC Cancer* 2006, 6, 243.
- [19] K. jian Xia, H. sheng Yin, and Y. dong Zhang, *J. Med. Syst.* 2019, 43, 2.
- [20] T. Tanaka, *J. Carcinog.* 2009, 8, 5.
- [21] M.J. Gora, M.J. Suter, G.J. Tearney, and X. Li, *Biomed. Opt. Express* 2017, 8, 2405.
- [22] K. Li, W. Liang, J. Mavadia-Shukla, H.C. Park, D. Li, W. Yuan, S. Wan, and X. Li, *J. Biophotonics* 2019, 12, e201800205.
- [23] W.A. Welge, and J.K. Barton, *Lasers Surg. Med.* 2017, 49, 249.

Chapter 5: Adaptive Boosting (AdaBoost)-based multi-wavelength spatial frequency domain imaging and characterization for *ex vivo* human colorectal tissue assessment

5.1 Background

Computer-aided diagnosis (CAD) can assist the analysis and classification of medical images with objective and quantitative interpolation. Combined with other optical imaging modalities such as optical coherence tomography (OCT), photoacoustic imaging (PAI), and fluorescence imaging, CAD has demonstrated the ability to differentiate normal from malignant colorectal tissues [1-4]. Recently, Sreyankar et al. reported the application of spatial frequency domain imaging (SFDI) of three visible wavelengths of 460 nm, 530 nm and 630 for differentiating normal from malignant colon using a logistic regression model [5]. It achieved an AUC of 0.902 based on quantitative absorption and scattering information of human colorectal tissues. These studies have established that neoplastic disruptions of the normal colonic wall structure produce altered absorption and/or scattering coefficient patterns in comparison to normal controls.

Among CAD algorithms, Adaptive Boosting (AdaBoost) is a relatively new non-linear machine learning algorithm [6]. AdaBoost can be combined with many other types of machine learning algorithms and the outputs of individual learning algorithms (weak learners) are combined into a weighted sum and the final model will converge to a strong learner [7, 8]. Since AdaBoost is a boosting-based algorithm, like most other ensemble methods, the likelihood of overfitting is very low [9]. AdaBoost has recently been adopted by many researchers in the medical imaging field to assist diagnosis. These applications include discrimination of breast tumors in ultrasonic images

[10], brain tumor classification in Magnetic Resonance Imaging (MRI) [11–13], and lung bronchovascular classification in Computed Tomography (CT) [14].

We report in this study the classification of colorectal tissues including normal, adenomatous polyp, and cancer specimens using AdaBoost-based multi-wavelength SFDI in the spectral range of 660 nm to 930 nm. Freshly excised colorectal tissues were imaged *ex vivo*. Wide-field absorption and scattering maps were constructed for the samples using nine discrete imaging wavelengths. An AdaBoost classifier was trained based on the absorption and scattering features and its performance was further evaluated using the AUC. The performance was also compared with support vector machine (SVM) classifiers.

5.2 Materials and Methods

5.2.1 Colon specimen preparation

Patients undergoing extirpative colonic resection at Washington University School of Medicine were recruited. From these patients, freshly excised colorectal specimens were imaged using a nine wavelength SFDI device. This study was approved by the Institutional Review Board, and the informed consent was obtained from all patients. Diagnoses were ascertained by subsequent histologic examination.

5.2.2 SFDI System

A low-cost, hand-held SFDI probe was used in this study and was described in detail in our previous study [15]. Briefly, 9 LEDs (660, 740, 780, 810, 830, 850, 890, 935 and 950 nm) were placed on a custom-designed printed circuit board (PCB). A rotational stepper motor (PG20L-D20-HHC0, NMB Technologies) was used to rotate the PCB in order to switch the LED that was positioned on the optical axis of the lenses. Light from the LED was homogenized by a beam

diffuser, and then collimated by the collimating lens (Thorlabs, AC254-050-B-ML). A linear stepper motor (19541-12-905, Ametek) drives a printed sinusoidal pattern to provide three phase-shifted patterns shining on the tissue (0 , $2\pi/3$, and $4\pi/3$). Two polarizer plates (one on the illumination path and one on the detection path) are used to reject specular reflection. A CMOS camera (EO-0413M-GL, Edmund Optics) combined with a 25 mm Fixed Focal Length Lens (67-715, Edmund Optics) was used to collect the diffused light. The overall acquisition time for all 9 wavelengths was around 2 minutes per specimen.

5.2.3 Absorption and scattering feature characterization

Briefly, for each wavelength, three phase-shifted images of the diffused reflected light were used to extract the DC (spatial frequency = 0 cm^{-1}) and AC (spatial frequency = 1 cm^{-1}) components using amplitude demodulation method [16, 17]. A reference phantom was used to calibrate the diffuse reflectance components of the sample under the same illumination condition. Absorption coefficient (μ_a) and reduced scattering coefficient (μ_s') maps were calculated using the two measured diffuse reflectance from the tissues and the phantom. The reconstruction time for all wavelengths was about 1 min. Independent regions of interest (ROIs) with sizes of approximately $5 \text{ mm} \times 3.75 \text{ mm}$ were then selected from the reconstructed absorption and reduced scattering coefficient maps. A total of 88 ROIs (44 normal areas, 14 adenomatous polyp and 30 cancer areas) from 16 patients were selected and processed. For each specimen, the ROIs were selected far away from each other to avoid overlap. The averaged absorption and reduced scattering coefficient of each ROI were extracted for further statistical analysis and classification.

5.2.4 Feature selection

A total of 18 features, including the averaged absorption and reduced scattering coefficients for 9 different wavelengths, were extracted from all ROIs. To explore a minimum number of

wavelengths needed to achieve the same performance of classification, we generated a total of 502 data sets with different numbers of features using 9 wavelengths or a subset of 9 wavelengths. To obtain both oxygenated hemoglobin (HbO₂) and deoxygenated hemoglobin (Hb) spectral information, a minimal of 2 wavelengths were used in the subset of 9 wavelength study. These features were input into the AdaBoost classifier to characterize the classification of normal, adenomatous polyp, and cancer tissues.

5.2.5 AdaBoost classifier

AdaBoost is a boosting technique that combines multiple weak classifiers into a single strong classifier. Detailed steps of AdaBoost is given in Algorithm 1 and Figure 5.1. Briefly, in each iteration t , each weak classifier, h_t , is trained by minimizing the weighted training error, ϵ_t , as given in step 2 of Algorithm 1. Then the significance of the h_t is evaluated by computing α_t . If ϵ_t is 0.5, then α_t is zero and the classifier is not counted for final AdaBoost output. If ϵ_t is less than 0.5, then α_t is positive and the corresponding h_t is contributing to the final AdaBoost output. Otherwise, the corresponding h_t is negatively contributing to the final AdaBoost output. If ϵ_t is smaller than a *threshold value* which shows a good fitting, then the iteration will be stopped. The error weight $\omega_i^{(t)}$ for each iteration of boosting is updated by either increasing ($h_t(\vec{x}_i) \neq y_i$) or decreasing ($h_t(\vec{x}_i) = y_i$) as given in Step 5. The final AdaBoost output is the weighted summation of all weaker classifiers. The AdaBoost classifier with decision trees as weak learners is a benchmark tree-based ensemble classification algorithm [18]. Therefore, a simple one layer decision tree was chosen to be the weak learner. An iteration number T of 50 and a *threshold value* of 0.02 were found to be optimal in this study and used for all computations. All classifiers were built under *Python 3.7* environment.

Algorithm 5.1 AdaBoost classifier

Input: $D(y = \{-1, +1\})$, T

Initialize input weights: $\omega_1^{(0)}, \omega_2^{(0)}, \dots, \omega_n^{(0)} \mid = \frac{1}{n}$

For $t = 1, \dots, T$

1. Train a weak learner, h_t , by minimizing the weighted training error;
2. Compute the weighted training error of h_t :

$$\epsilon_t = \sum_{i=1}^n \omega_i^{(t-1)} \llbracket h_t(\vec{x}_i) \neq y_i \rrbracket$$

3. If $\epsilon_t < \text{threshold value}$, end iteration.
4. Compute the “importance” of h_t :

$$\alpha_t = \frac{1}{2} \log\left(\frac{1 - \epsilon_t}{\epsilon_t}\right)$$

5. Update the weights:

$$\omega_i^{(t)} = \frac{\omega_i^{(t-1)}}{Z_t} \times \begin{cases} e^{-\alpha_t} & \text{if } h_t(\vec{x}_i) = y_i \\ e^{\alpha_t} & \text{if } h_t(\vec{x}_i) \neq y_i \end{cases}$$

AdaBoost Output:

$$g_T(\vec{x}) = \text{sign}(H_T(\vec{x})) = \text{sign}\left(\sum_{t=1}^T \alpha_t h_t(\vec{x})\right)$$

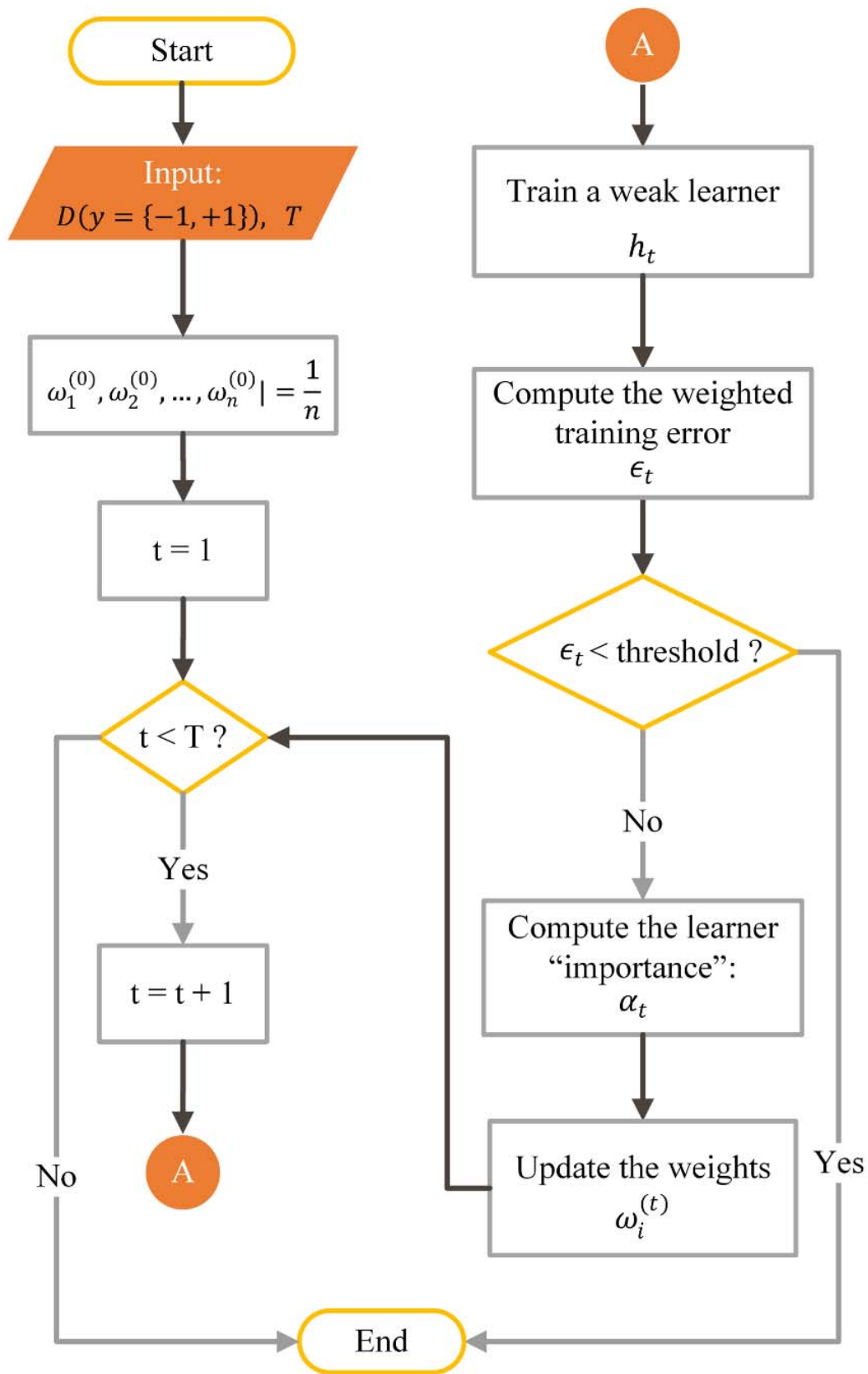


Figure 5.1 Flow chart for AdaBoost algorithm.

Different data sets described in Feature selection session were inputted into the AdaBoost classifiers for identifying colorectal tissue types. To train the abnormal vs. normal classifier, 30 normal areas, and 30 adenomatous polyp and cancer areas were included in the training cohort and the remaining in the testing cohort. 1000 repeated tests were performed and averaged to obtain the ROC curve. For each test, the training set was randomly selected, and the remaining ROIs were used for testing.

For comparison with the well-known SVM classifier, two abnormal vs. normal SVM classifiers with linear kernel or radial basis function (RBF) kernel were also trained using 18 features from all 9 wavelengths. The training set size and number of tests were the same as the AdaBoost classifier.

Additionally, we trained AdaBoost adenomatous polyp vs. normal and adenomatous polyp vs. cancer classifiers individually to better differentiate performance in both adenomatous and malignant settings. For each classifier, 10 adenomatous polyp areas, and 10 normal or cancer areas were used for training and the remaining for testing. The number of tests was the same as the abnormal vs. normal classifier.

5.2.6 Statistical analysis

The student's t-test was used to evaluate the statistical significance within each individual feature. A p-value less than 0.05 is considered statistically significant. And the ROC and AUC were used for evaluating the accuracy of the trained AdaBoost or SVM classification models.

5.3 Results

5.3.1 Reconstructed absorption and reduced scattering coefficient maps

Figure 5.2 shows representative absorption and reduced scattering coefficient maps (at 660 nm and 950 nm), H&E stained histology results and photographs of cancer and normal region from one colon sample. It was observed that the cancer region had a significantly higher absorption coefficient compared to the normal area. In contrast, the cancer region had a lower reduced scatter coefficient compared to the normal area.

Figure 5.3 shows representative absorption and reduced scattering coefficient maps at 660 nm and 950 nm, H&E stained histology results and photographs of one colon specimen with an adenomatous polyp and corresponding normal area. This polyp has an absorption coefficient that is close to the normal area, which is relatively low, but the reduced scattering coefficient is close to the cancer area with a relatively low value.

5.3.2 Absorption and scattering feature characterization

A comparison between lesions of mean absorption coefficient and reduced scattering coefficient of all regions of interest at all wavelengths is shown in Figure 5.4. According to the student's t-test, μ_a and μ_s ' for all wavelengths are significantly different between cancer and normal areas ($p < 0.001$). For all wavelengths, μ_a in adenomatous polyp areas are significantly different from cancer areas ($p < 0.001$), but has no significant difference compared to normal areas for wavelengths between 780 nm to 935 nm ($p > 0.05$). As for μ_s ', adenomatous polyps at all wavelengths show statistical significance from normal areas ($p < 0.001$) and statistical significance ($p < 0.05$) than malignancy areas except at 935 nm ($p = 0.06$).

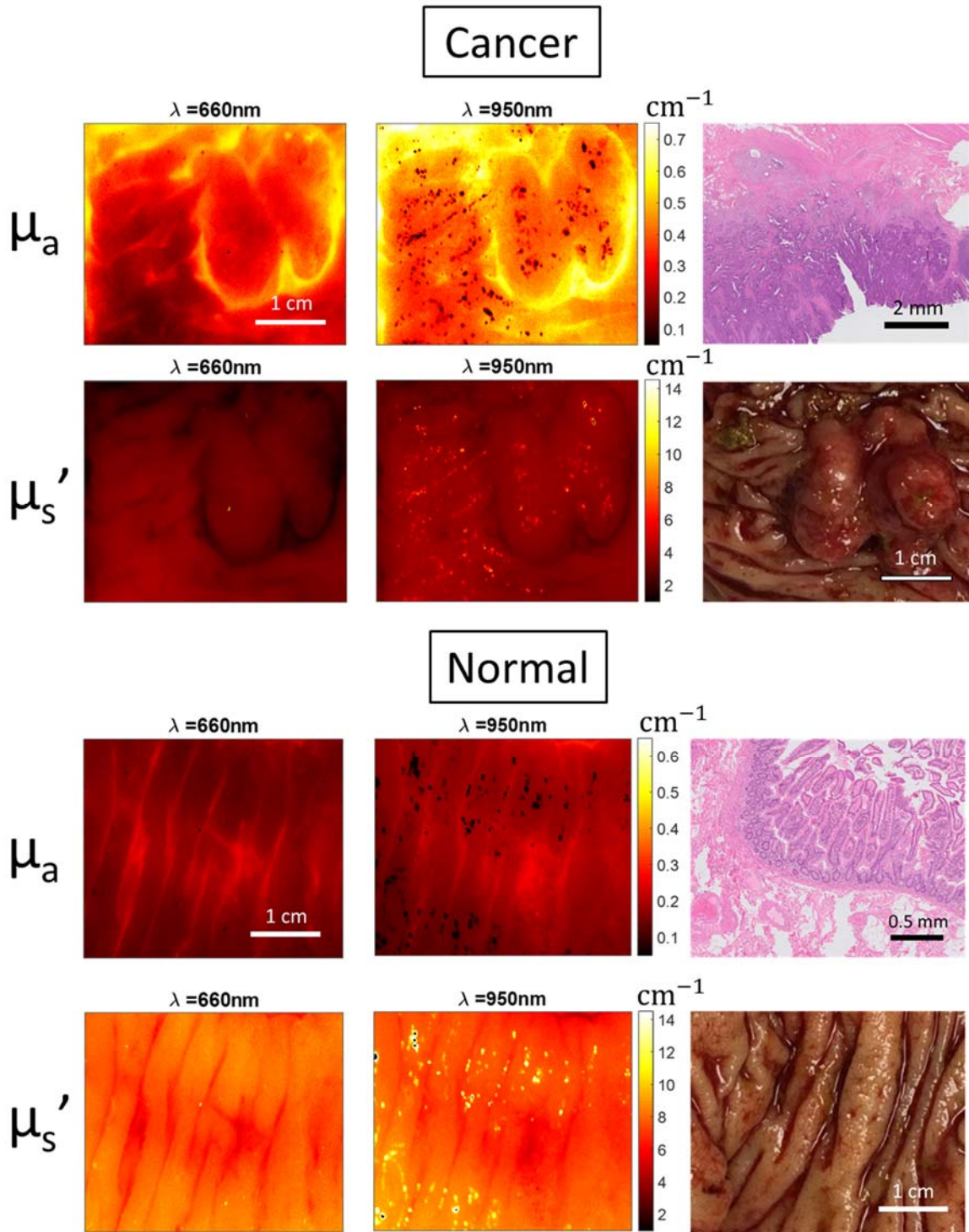


Figure 5.2 Absorption and reduced scattering coefficient maps (at 660 nm and 950 nm), H&E stained histology results and photographs of a T2 adenocarcinoma and corresponding normal tissue.

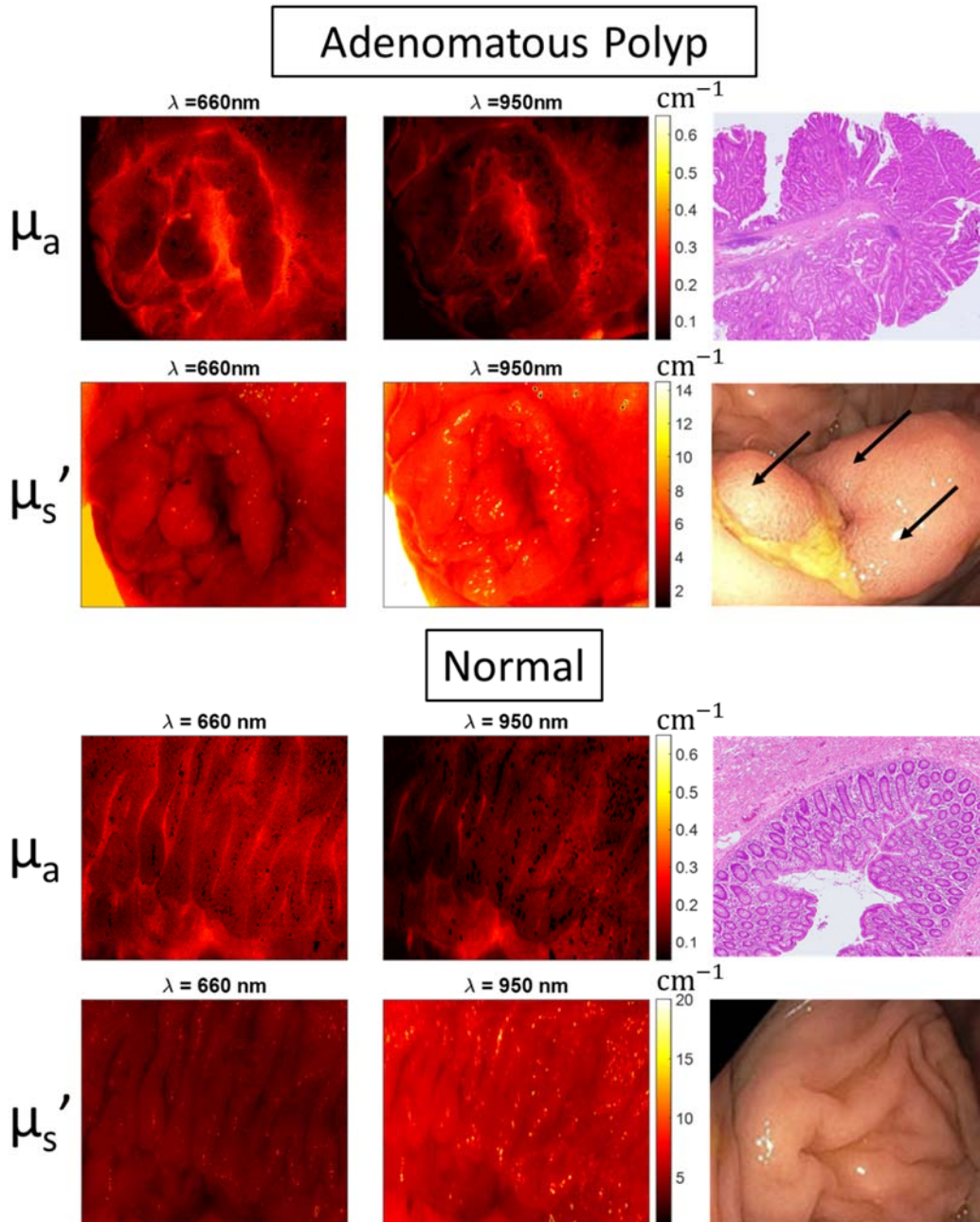


Figure 5.3 Absorption and reduced scattering coefficient maps (at 660 nm and 950 nm), H&E stained histology results and photographs of an adenomatous polyp and corresponding normal tissue. The photographs were taken *in vivo* using white light colonoscope.

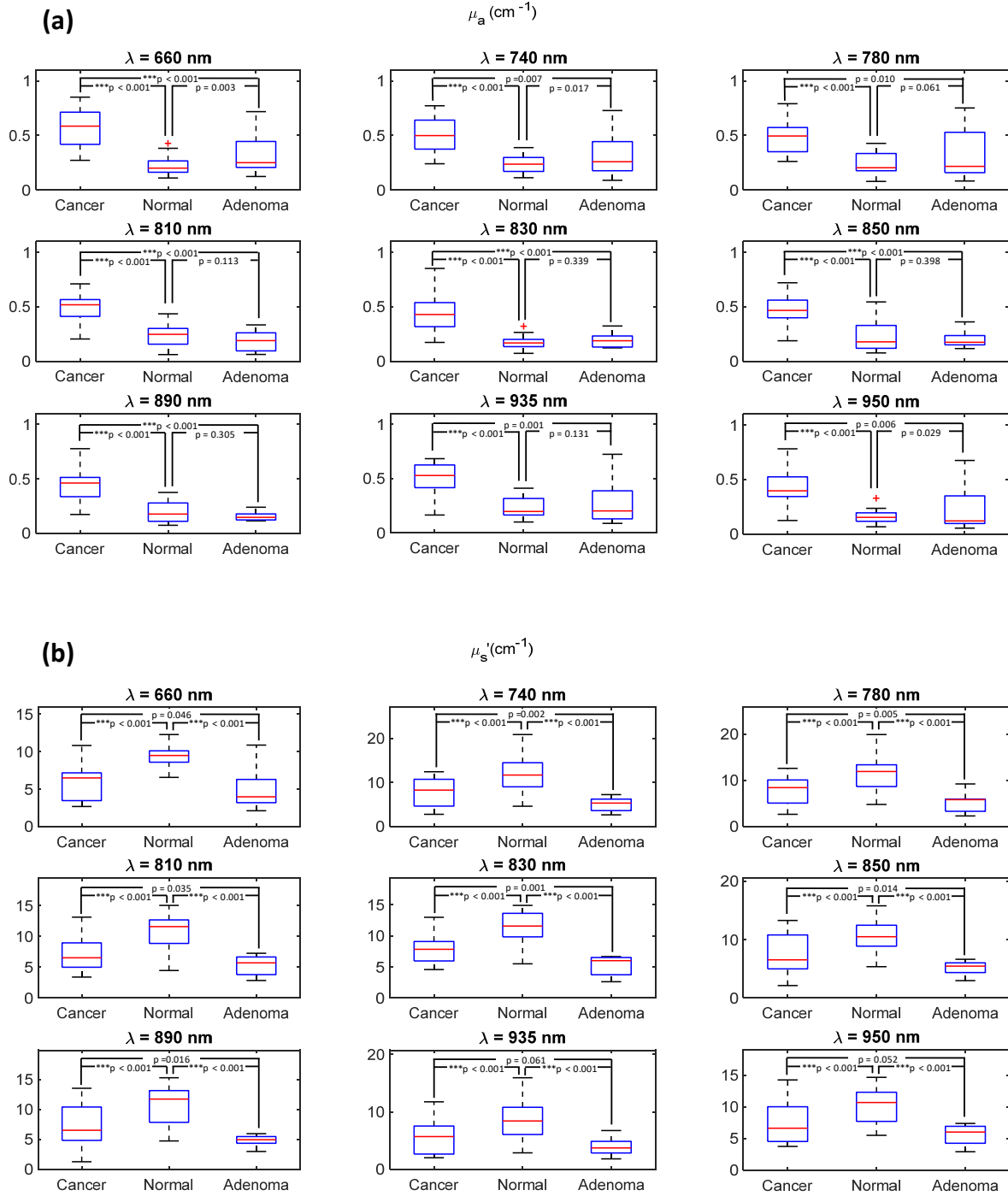


Figure 5.4 Boxplot of averaged absorption coefficient (a) and reduced scattering coefficient (b) of cancer, normal and adenomatous polyp (adenoma) groups.

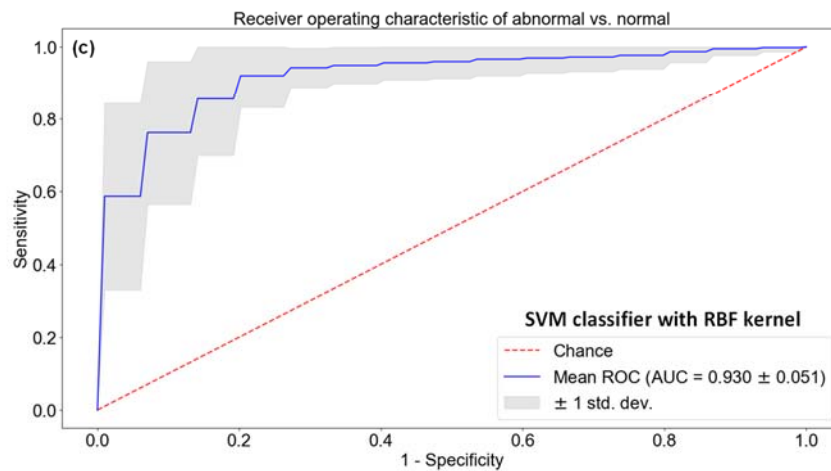
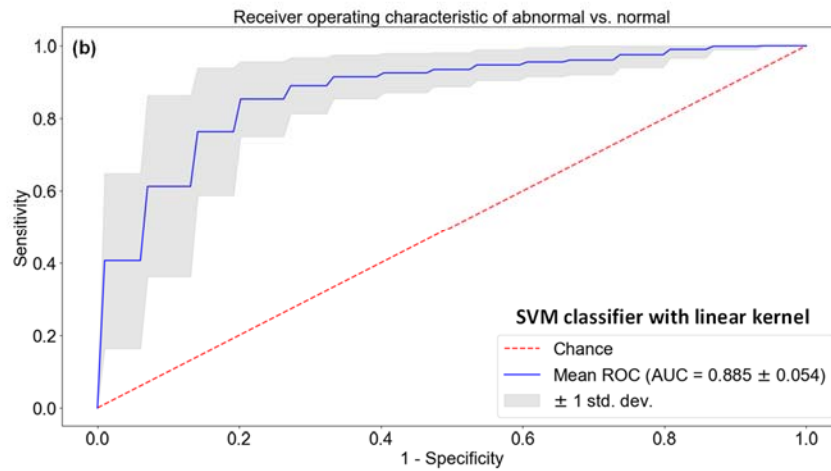
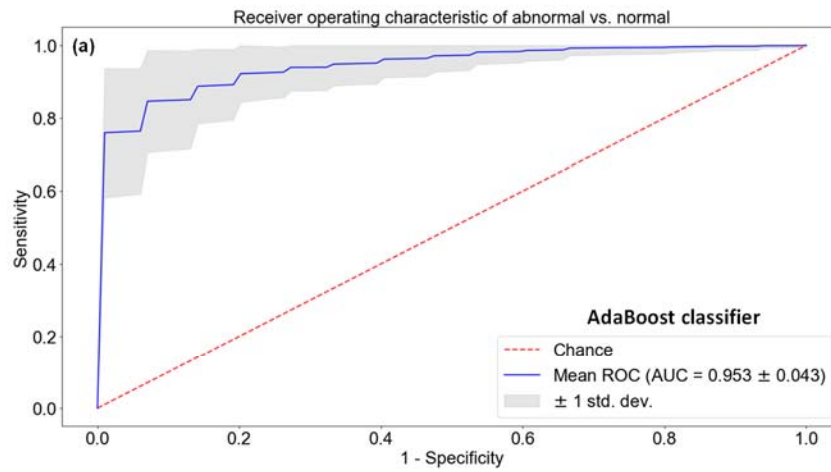


Figure 5.5 Receiver operating characteristic curve for abnormal vs. normal AdaBoost classifier (a), SVM classifier with linear kernel (b), and SVM classifier with RBF kernel (c). The shaded zone marks the standard deviation.

5.3.3 Testing result of AdaBoost classifier and SVM classifiers using all wavelengths

The ROC curve of the testing results of the AdaBoost abnormal vs. normal classifier is shown in Figure 5.5a. An AUC of 0.953, optimal sensitivity and specificity of 89.1% and 85.7% were achieved. The linear SVM and SVM with RBF kernel yield AUC of 0.885 and 0.934, respectively, and the ROC curves are shown in Figure 5.5b-c. Besides improved AUC, it can also be seen that AdaBoost has a smaller standard deviation compared to SVM.

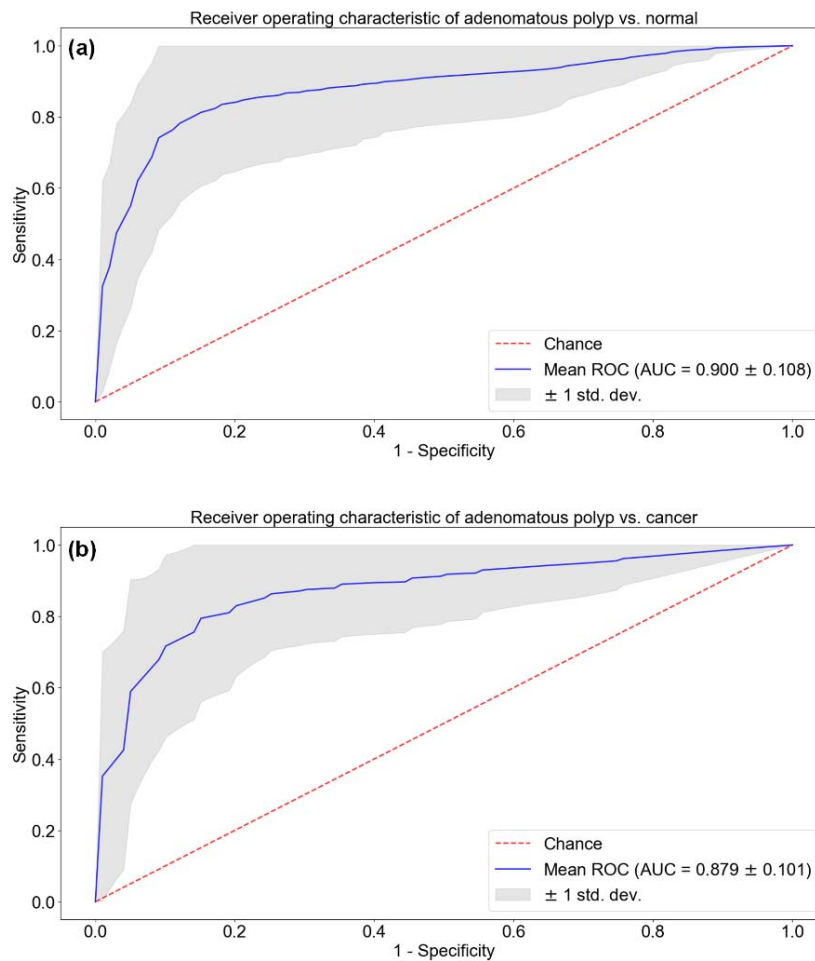


Figure 5.6 Receiver operating characteristic curve for adenomatous polyp vs. normal AdaBoost classifier (a), and adenomatous polyp vs. cancer AdaBoost classifier (b). The shaded zone marks the standard deviation.

The ROC curves of the testing results of the AdaBoost normal vs. adenomatous polyp and adenomatous polyp vs. cancer classifiers are shown in Figure 5.6. They yield AUC of 0.900 and 0.879, respectively.

5.4 Discussion

This is the first report using an AdaBoost-based multiwavelength SFDI system for the classification of colorectal tissues including normal, malignant, and adenomatous polyp specimens. Wide-field absorption and scattering maps were estimated for colorectal specimens over nine wavelengths. Drastically different quantitative characteristics were captured by SFDI for these three types of specimens. Elevated absorption coefficient among tumors, potentially due to malignant angiogenesis, were uniformly noted along with decreased scattering coefficient as a contrast to normal specimens, which may result from structural disruption of highly organized colorectal tissues. Adenomatous polyps were found to have a lower absorption coefficient than tumors and lower scattering coefficient than normal colorectal tissues.

An abnormal vs. normal AdaBoost classifier was trained based on absorption and scattering features and achieved good AUC, sensitivity, and specificity with this limited dataset. It has been shown that linear SVM has a relatively low AUC for our data because spectral features of μ_a and μ_s are non-linearly related to the wavelength. SVM with a non-linear RBF kernel shows improved performance. AdaBoost further improves SVM with RBF kernel because Adaboost with decision trees is suitable for non-linear structure and robust to overfitting by taking a weighted average of many weak learners. Thus, AdaBoost is more suitable for our colorectal tissue classification based on multi-wavelength optical properties. Besides, the AdaBoost classifiers also achieved good AUC

in differentiating adenomatous polyps from normal or cancer tissue, which demonstrated its potential to apply to more complex or challenging situations.

It is worth mentioning that a similar AUC can be achieved with reduced wavelengths in distinguishing between the normal and abnormal colorectal tissues, which can provide guidance for selecting the optimal wavelengths for probing colorectal cancer to reduce the cost and complexity of the system. For example, we observed similar performance in distinguishing between normal and abnormal tissues even with two wavelengths (660 nm and 890 nm). This is likely due to differences between normal colorectal tissue vascular contrast and structure than cancer and polyps because 660 nm is highly sensitive to Hb absorption and 890 nm is highly sensitive to HbO₂ absorption in the spectral range investigated in the study [19]. In addition to hemoglobin, the contrast between normal and abnormal colorectal tissue may involve other components such as water and lipid. Thus, a wider range of wavelengths has achieved superior classification performance. These results suggest that multi-wavelength SFDI may be possible to assist clinical decision-making in several aspects. First, with a suitable segmentation algorithm, SFDI may be able to assist surgeons with tumor margin detection during surgeries based on tissue spectral absorption and scattering features and morphology changes. Second, the system may provide real-time assistance in detecting early, hard-to-identify lesions from normal endoluminal mucosa – which could lead to earlier identification of cancers. Currently, the data acquisition is using LabView, all image reconstruction and statistical analysis are performed in MATLAB, and the diagnosis is done using Python. It took less than 5 minutes for all the steps for one specimen. To further improve data acquisition and processing speed, a single snapshot SFDI system and algorithm can be adopted to reduce the data acquisition time by reconstructing optical properties

with one single image instead of three phase-shifted images. A deep learning-based reconstruction algorithm may also have the potential to reduce computational time.

In the above-described models, an optimal cut-off value was determined to obtain both high sensitivity and high specificity. However, in clinical practice, a high-sensitivity value is critical because we cannot afford to miss a malignant lesion [20]. Under this decision criterion, the AdaBoost classifier would have correctly detected cancer and adenomatous polyps as abnormality with 95% sensitivity and 61% specificity.

This study must be considered in the context of several limitations. First, all imaged specimens were imaged *ex vivo*. The human *in vivo* environment is likely more complex and may produce different results in actively perfused tissues. Besides, all *ex vivo* specimens had been identified as abnormal with white-light endoscopy prior to resection and imaging via SFDI. Within our sample set, we did not encounter any patients with incidentally found neoplasia. Further *in vivo* study is needed to test the ability of AdaBoost-based SFDI to identify abnormalities otherwise overlooked by standard endoscopy. Additionally, the system was not tested in the setting of all colorectal abnormalities, such as inflammatory bowel disease or non-neoplastic polyps. In the future, more patients including these tissue types need to be included for a complete evaluation of the AdaBoost-based SFDI system. In the future, more patients including thorough tissue types need to be included for a complete evaluation of the AdaBoost-based SFDI system. Fine-tune of the classifier's hyperparameters should also be performed as we are targeting 100% sensitivity with high specificity in clinical application.

References

- [1] Y. Zeng, B. Rao, W. C. Chapman, S. Nandy, R. Rais, I. González, D. Chatterjee, M. Mutch and Q. Zhu, *Sci. Rep.*, 2019, 9, 2998.
- [2] X. Leng, W. Chapman, B. Rao, S. Nandy, R. Chen, R. Rais, I. Gonzalez, Q. Zhou, D. Chatterjee, M. Mutch and Q. Zhu, *Biomed. Opt. Express*, 2018, 9, 5159.
- [3] G. Yang, E. Amidi, W. Chapman Jr, S. Nandy, A. Mostafa, H. Abdelal, Z. Alipour, D. Chatterjee, M. Mutch and Q. Zhu, in *Proc. SPIE* (Eds: A. A. Oraevsky, L. V. Wang), SPIE, U.S.A. 2019, 345.
- [4] N. Iftimia, A. K. Iyer, D. X. Hammer, N. Lue, M. Mujat, M. Pitman, R. D. Ferguson and M. Amiji, *Biomed. Opt. Express*, 2012, 3, 178.
- [5] S. Nandy, W. Chapman, R. Rais, I. González, D. Chatterjee, M. Mutch and Q. Zhu, *Tech. Coloproctol.*, 2018, 22, 617.
- [6] R. E. Schapire and Y. Freund, *Kybernetes*, 2013, 42, 164.
- [7] B. Kégl, arXiv preprint arXiv, 2013, 1312.6086.
- [8] H. Drucker and C. Cortes, in *Adv. in Neural Inf. Process. Syst. (NIPS)* (Eds: M. I. Jordan, T. Petsche), MIT Press, U.S.A. 1996, 479.
- [9] G. Ratsch, T. Onoda and K. R. Muller, in *Adv. in Neural Inf. Process. Syst.(NIPS)* (Eds: M.C. Mozer, M.I. Jordan, T. Petsche), MIT Press, U.S.A. 1998, 506.
- [10] A. Takemura, A. Shimizu and K. Hamamoto, *IEEE Trans. on Med. Imaging*, 2009, 29, 598.
- [11] S. Ghanavati, J. Li, T. Liu, P. S. Babyn and W. Doda, in *2012 9th IEEE Int. Symp. Biomed. Imaging (ISBI)*, IEEE, Spain 2012, 574.
- [12] A. Prabin and J. Veerappan, *Res. J. Appl. Sci. Eng. Technol.*, 2014, 8, 2374.
- [13] A. Minz and C. Mahobiya, in *IEEE 7th Int. Adv. Comput. Conf. (IACC)*, IEEE, India 2017, 701.

- [14] R. A. Ochs, J. G. Goldin, F. Abtin, H. J. Kim, K. Brown, P. Batra, D. Roback, M. F. Mcnittgray and M. S. Brown, *Med. Phys.*, 2008, 11, 315.
- [15] M. Erfanzadeh, S. Nandy, P. D. Kumavor and Q. Zhu, *Biomed. Opt. Express*, 2018, 9, 5503.
- [16] D. Cuccia, F. Bevilacqua, A. J. Durkin, F. R. Ayers and Bruce J., *J. Biomed. Opt.*, 2009, 14, 1.
- [17] S. Nandy, A. Mostafa, P. D. Kumavor, M. Sanders, M. Brewer and Q. Zhu, *J. Biomed. Opt.*, 2016, 21, 101402.
- [18] J. C. W. Chan and D. Paelinckx, *Remote Sens. Environ.*, 2008, 112, 2999.
- [19] S.A. Prahl, Tabulated molar extinction coefficient for hemoglobin in water. <http://omlc.ogi.edu/spectra/hemoglobin/summary.html> (accessed: December, 2019).
- [20] V. Giannini, S. Mazzetti, I. Bertotto, C. Chiarenza, S. Cauda, E. Delmastro, C. Bracco, A. Di Dia, F. Leone, E. Medico, A. Pisacane, D. Ribero, M. Stasi and D. Regge, *Eur. J. Nucl. Med. Mol. Imaging*, 2019, 46, 878.

Chapter 6: Histogram Analysis of *en face* Scattering Coefficient

Map Predicts Malignancy in Human Ovarian Tissue

6.1 Background

Optical coherence tomography (OCT) can provide micro-scale real-time images and is able to obtain an ‘optical biopsy’ without physically resecting the tissue.[1-4] The OCT contrast is generated from the backscattered light from different layers of tissue; thus, it is suitable for extracting tissue scattering heterogeneity. The feasibility of OCT in laparoscopy and fallopscopy for ovarian tissue B-scan imaging has already been demonstrated.[5,6] The scattering coefficient, which is related to the collagen content and directivity, was extracted from OCT A-scans and found to be a good biomarker for characterizing human ovarian cancer.[7,8] Scattering coefficient distribution within B-scans based on 2-D analysis and histogram analysis of B-scan images have been used in automated classification of urinary bladder cancer, Barrett’s esophagus, human skin cancer, and human atrial tissue using OCT.[9-12] All these studies mainly focus on B-scan images and features, and show promising results. 3-D texture analysis of OCT images of a mouse ovary model achieved statistically significant performance.[13] Histogram analysis has also been applied to MRI, ultrasound, and CT to characterize tumor heterogeneity.[14-16] Spatial frequency domain imaging (SFDI) is another imaging modality that is able to quantify scattering and has shown promise in classifying ovarian tissue.[17] SFDI has a large field of view; however, its resolution (~mm) is not high enough to detect neoplastic micro-structural scatter changes associated with the progression of ovarian cancer.

In this study, we report, for the first time, characterization and classification of *ex vivo* human ovary and fallopian tube based on features obtained from 3-D analysis of depth-resolved *en face*

scattering maps of OCT images. Initial results indicate that quantitative scattering features extracted from the OCT images can be used to identify ovarian cancer.

6.2 Materials and Methods

6.2.1 Ovary sample preparation

This study was approved by the Institutional Review Board (IRB), and informed consent was obtained from all patients. 26 freshly excised human ovaries and 9 fallopian tubes from 20 patients (see Table 6.1) undergoing surgery for various clinical indications were imaged with OCT in the Optical and Ultrasound Imaging Lab located at Washington University School of Medicine. Ovaries were imaged immediately after surgery (~5 mins) and returned to the Pathology Department within an hour for routine processing. Pathologists in the frozen section lab provided guidance to the researchers as to the sample orientation and location of tumor, which was in any event not subtle. Therefore, we are certain that we imaged the tumor for the malignant specimens.

6.2.2 Feature extraction

For ovarian specimens, collagen fibers were found to be the main scattering source in the stroma underlying the surface epithelium.[18-20] Thus, the ovarian epithelium layer was first located semi-automatically (area between the two red curves in Figure 6.1a and 1c using the shortest-path algorithm). Then the scattering coefficient within the ovarian cortex layer was calculated by fitting each A-scan with a single scattering model based on Beer's law. By fitting all A-lines within one 3-D scan (1000 A-lines x 500 B-scans), we generated a depth-resolved *en face* scattering coefficient map of the scanned ovarian tissue.

Table 6.1 Ovarian Lesion characteristics

Cancerous ovaries	High grade serous carcinoma (n=4, average size 8 cm, range 5.5-10 cm) Sertoli-Leydig cell tumor (n=1, size 19.2cm)
Benign ovaries	Fibrothecoma (n=1, size 14cm) Cystic follicles (n=1, size 3cm) Epidermoid cyst (n=1, size 7.6cm) Inclusion cysts (n=2, average size 4.3cm, range 3.5-5cm) Mesothelial cyst (n=1, size 3.1cm) Cortical, fibrosis, and hyperthecosis hemorrhagic corpus luteum (n=1, size 4cm) Benign leiomyoma (n=1, size 5.5cm) Serous/Mucinous cystadenoma (n=6, average size 8.4cm, range 2.5-21 cm) Benign cystic endometriosis (n=1, size 6cm) No significant histopathological abnormalities (n=6)
Benign fallopian tubes	No significant histopathological abnormalities (n=9)

Each scattering map was further subdivided into several non-overlapping images to avoid hyper-reflection and out-of-focus areas. Six features were extracted quantitatively using MATLAB R2018a from the analysis of the histogram of all scattering maps. Six features can be computed from Equation (1) to (6), where x_i is the pixel gray level and N is the total number of pixels.

$$\text{Mean}(\mu) = \frac{1}{N} \sum_{i=1}^N x_i \quad (1)$$

$$\text{Variance}(\sigma^2) = \frac{1}{N} \sum_{i=1}^N (x_i - \mu)^2 \quad (2)$$

$$\text{Entropy} = - \sum_{i=1}^N p(x_i) \log_2 p(x_i) \quad (3)$$

$$\text{Skewness} = \frac{1}{N} \sum_{i=1}^N \left[\frac{x_i - \mu}{\sigma} \right]^3 \quad (4)$$

$$\text{Kurtosis} = \frac{1}{N} \sum_{i=1}^N \left[\frac{x_i - \mu}{\sigma} \right]^4 - 3 \quad (5)$$

$$\text{Energy} = \frac{1}{N} \sum_{i=1}^N [p(x_i)]^2 \quad (6)$$

where $p(x_i) = \frac{x_i}{s(1)*s(2)}$, $s(1)$ is the image width and $s(2)$ is the image length. The statistical significance of these six features was further evaluated using the Wilcoxon rank-sum test.

6.2.3 Feature selection and classification

In the first step, the Spearman's cross correlation among all features was evaluated and features with correlation coefficient smaller than 0.5 were considered independent of each other. Next, two optimal feature sets: "mean and entropy" and "energy, skewness, entropy" were selected. Each optimal feature set consists of features that are not correlated by our measure and provide best testing results. Then two prediction models (LR and SVM) were trained using these two feature sets through `glmfit` and `fitsvm` functions in MATLAB. Approximately two thirds of the data were used for training two predictive classifiers and the rest were used for testing the models. Repeated rounds (100 times) of training and testing were applied by randomly selecting 2/3 of the samples for training and 1/3 of the samples for testing. One hundred receiver operating curves (ROC) were

generated, and the averaged sensitivity, specificity, and area under the curve (AUC) were used for evaluating the accuracy of the model.

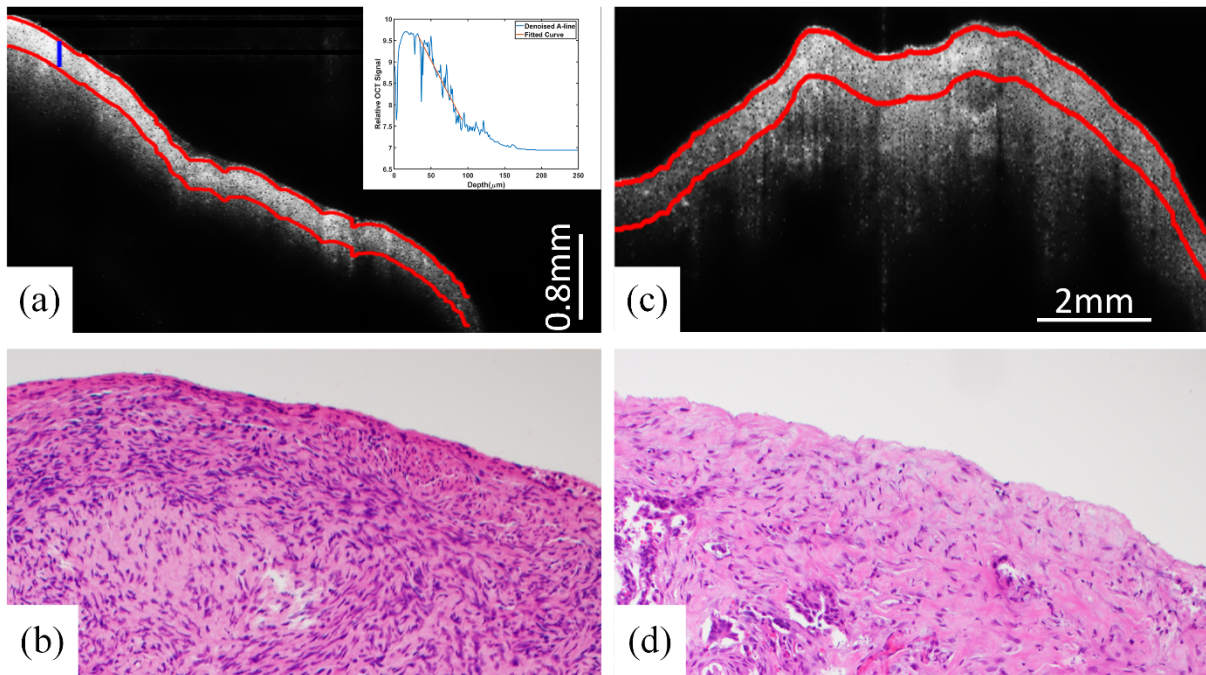


Figure 6.1 Representative OCT images of benign and malignant ovary specimens. The ovarian surface epithelium is between the two red curves in the B-scan SS-OCT images. (A) representative B-scan image from a benign ovary and (B) corresponding H&E image. (C) representative B-scan image from a malignant ovary (high-grade serous carcinoma) and (D) corresponding H&E image. Inset: best-fit Beer’s law is used to calculate the scattering coefficient.

6.3 Results

A total of 20 patients (mean age 56 years; range 37-87) of 26 ovaries were imaged ex vivo from February 2017 to October 2018. Table 1 provides pathological characteristics of these ovaries. Diagnoses ascertained by subsequent surgical pathology examination revealed high-grade serous carcinoma (n=4 ovaries), Sertoli-Leydig cell tumor (a sex cord-stromal tumor; n=1), normal ovaries (n=6), other causes of benign but enlarged ovaries (n=15), and benign fallopian tubes (n=9) (Table 1).

6.3.1 B-scan images of ovary samples

Representative SS-OCT B-scan images of benign ovaries, malignant ovaries, and corresponding H&E slides are shown in Figure 6.1. The OCT and the histologic images have similar scales and come from similar, but not identical, locations within the ovary specimens. In Figure 6.1b, non-neoplastic ovarian stroma is seen, characterized by bland spindle cells in a dense collagenous background. Figure 6.1d, in contrast, is infiltrated by high-grade serous carcinoma. Irregular islands of neoplastic cells are present in the lower left of the panel, characterized by increased nuclear to cytoplasmic ratio, formation of abortive glandular structures, and surrounding stromal desmoplasia (stromal reaction to invasive tumor). The neoplastic cellularity in this case is approximately 20% by visual estimate of the H&E slide, which is typical of cases included in the study.

6.3.2 Scattering coefficient maps of human ovary specimens

Figure 6.2a-c shows photographs of one benign ovary, one malignant ovary (high-grade serous carcinoma), and one benign fallopian tube, respectively. The scattering coefficient maps of the scanned areas, identified as white boxes in Figure 6.2a-c, are shown in Figure 6.2d-f. The white areas in the scattering map indicate the background or tissue area that is out of focus. The normal ovarian specimen exhibits much higher scattering on average and is more homogeneous compared to malignant ovary, which has significantly lower scatter and disorganized collagen distribution. The benign fallopian tube shows a spatially heterogeneous scattering distribution that significantly differs from the ovary scattering maps.

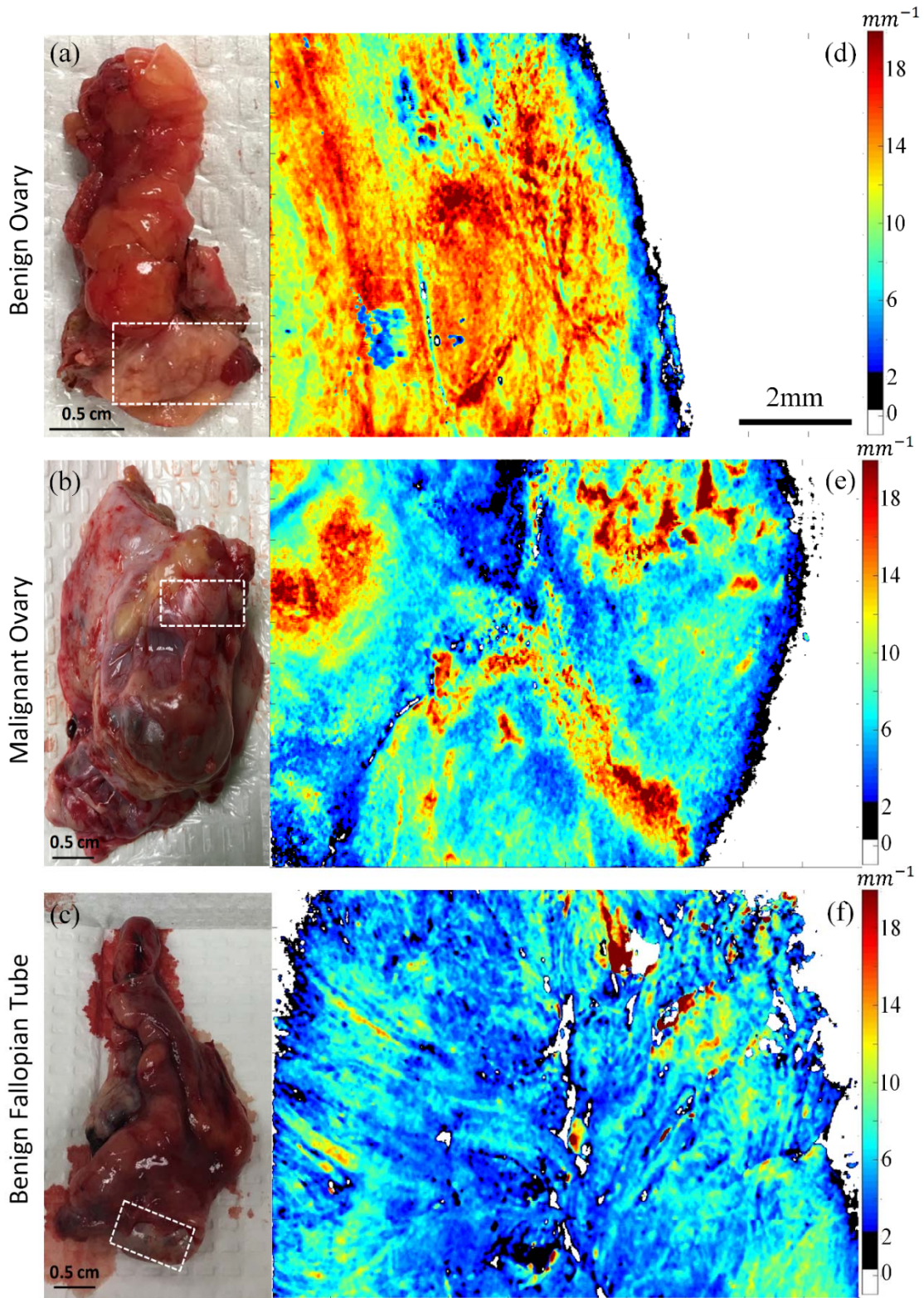


Figure 6.2 Scattering coefficient maps of human ovarian tissues. Photographs (A-C) of one benign ovary, one malignant ovary, and one benign fallopian tube, respectively. Scattering coefficient maps (D-F) of the scanned areas, identified as white boxes in Figure (A-C). The scale bar of 200 μm is shared by maps (D-F).

6.3.3 Histogram analysis

Six features were extracted from scattering maps and histograms of 27 non-overlapping malignant ovary scattering maps, 64 non-overlapping benign/normal ovary scattering maps, and 9 non-overlapping benign fallopian tube scattering maps. Each non-overlapping scattering map was from a 5 mm x 10 mm area of a different region of the examined ovary. Depending on the size of the ovary, one to four non-overlapping areas were imaged and scattering maps were generated. Figure 3 shows representative histograms derived from one malignant ovary (Figure 6.3a) and one benign ovary (Figure 6.3b). Gaussian curves (best-fit) of the histograms are shown in red for visualization. Figure 6.4 shows the boxplots for the mean, variance, entropy, skewness, kurtosis, and energy across the entire set of 26 ovaries. All features showed statistically significant differences between malignant and benign ovarian tissues. Cancerous specimens had significantly lower mean, variance, and entropy of scattering coefficient, but markedly higher skewness, kurtosis, and energy than benign specimens. The mean and variance were significantly different between cancer ovaries and benign fallopian tubes, and the mean, variance, and kurtosis had statistically significant differences between benign ovaries and benign fallopian tubes. In addition, fallopian tubes showed different scatter distribution than either malignant tissue or benign tissue.

6.3.4 Training and testing results of two predictive models

Although all features differed between benign and malignant, we hypothesized that a combination of features would allow better classification of ovaries. Figure 6.5 shows ROC curves for the testing sets of both LR and SVM models trained on two optimal feature sets. The first feature set consisted of mean scattering coefficient and scattering map entropy. For this set, a sensitivity and specificity of 97.0% and 97.8% was obtained from LR, with average AUC of 0.986; a sensitivity and specificity of 99.6% and 96.4% was achieved from the SVM, with average AUC of 0.991. A

second set consisted of energy, skewness, and entropy. The trained LR model achieved a sensitivity and specificity of 93.4% and 82.1%, with average AUC of 0.956; the SVM achieved a sensitivity and specificity of 91.1% and 84.2%, with average AUC of 0.957. Thus the optimal set of features is mean scattering coefficient and scattering map entropy. Both LR and SVM have similar diagnostic performance.

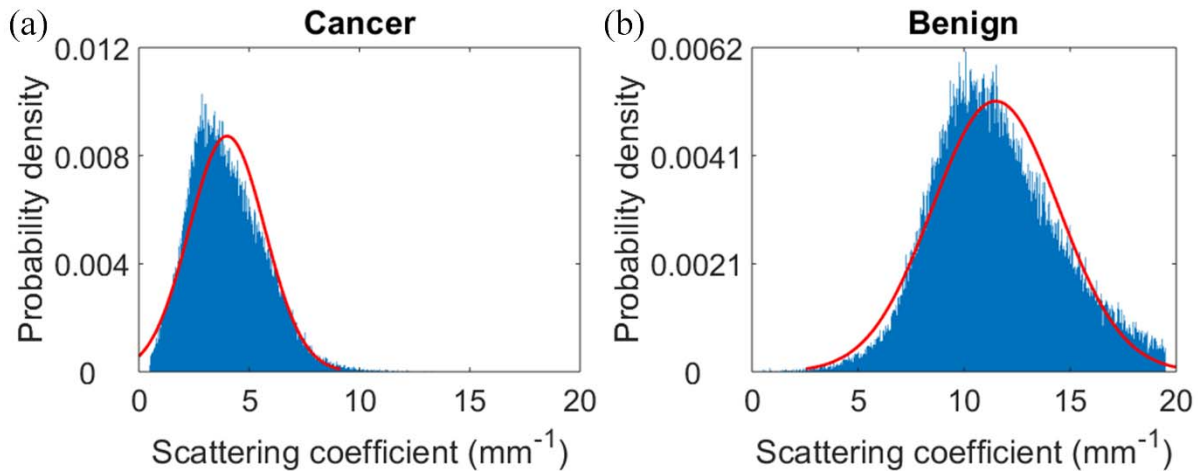


Figure 6.3 Histogram analysis of one representative malignant ovary (A) and one representative benign ovary (B). The six features for (A) are 4.0 mm^{-1} (mean), 1.71(variance), 6.50(entropy), 0.77(skewness), 4.33(kurtosis), and 0.17(energy). The six features for (B) are 11.48 mm^{-1} (mean), 2.98(variance), 7.30(entropy), 0.22(skewness), 2.85(kurtosis), and 0.10(energy). Fitted Gaussian distribution is shown as red curves.

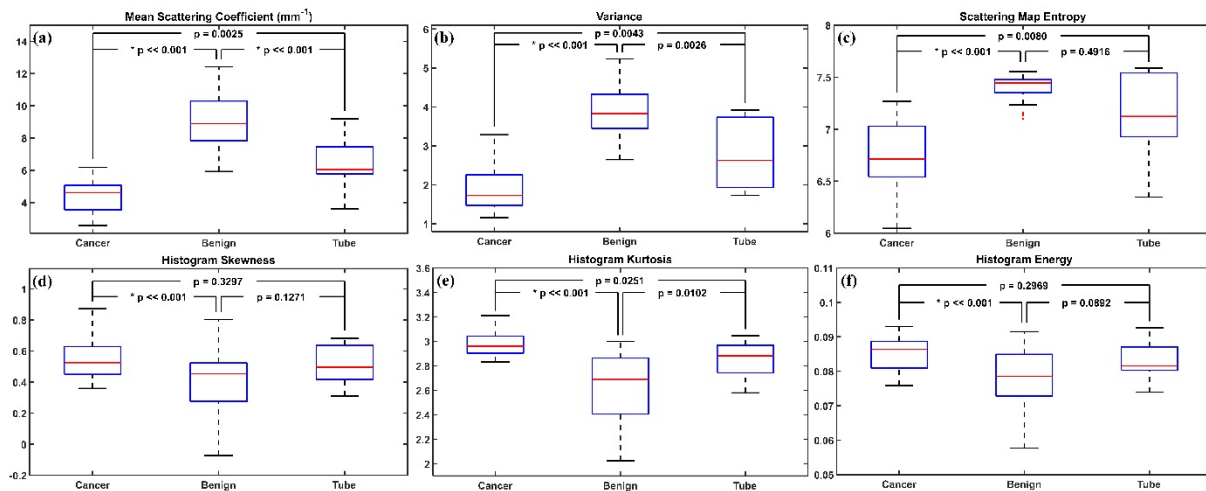


Figure 6.4 Boxplot of the six features extracted from histogram analysis of scattering maps of malignant ovaries, benign ovaries, and benign fallopian tubes.

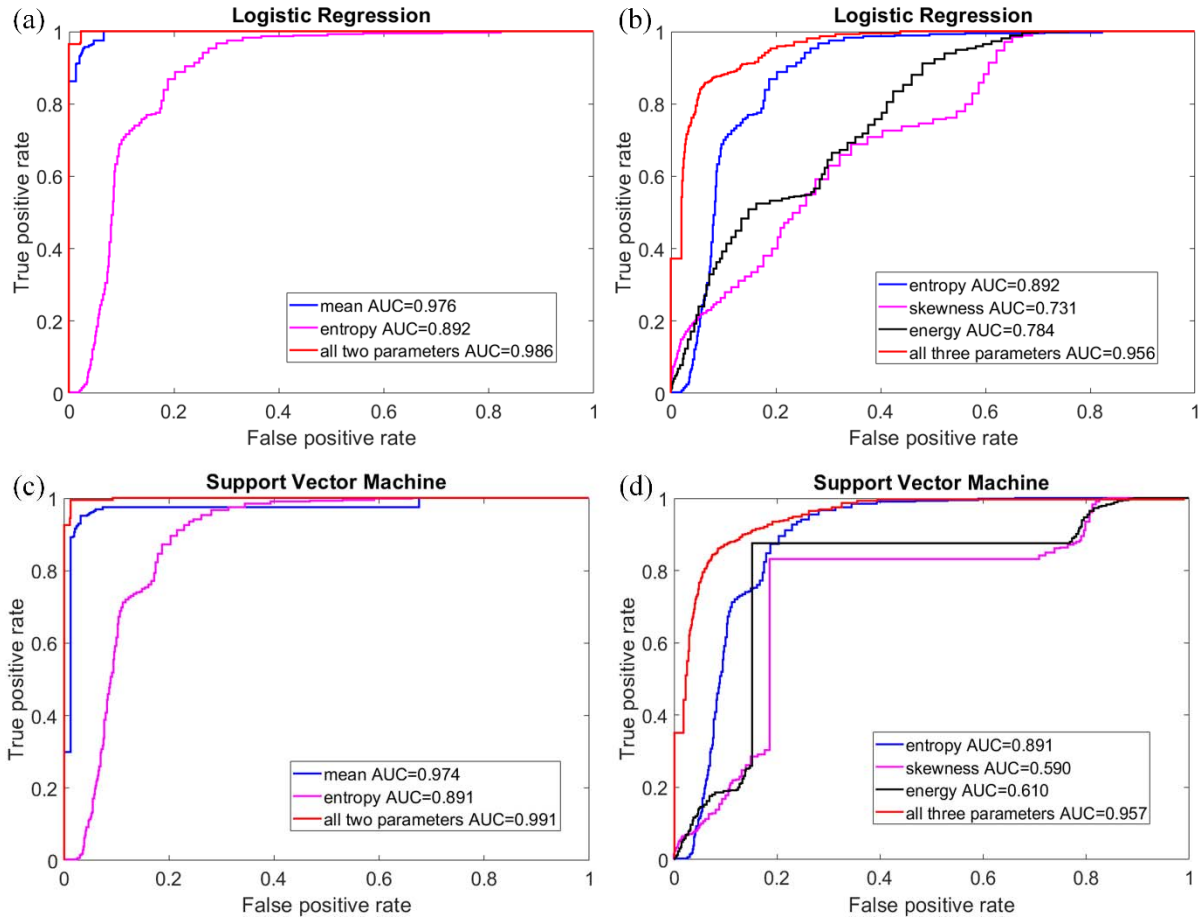


Figure 6.5 Testing results of two optimal data sets ([mean, entropy] and [energy, skewness, entropy]) used to train two classification models. (A-B) show the ROC curves for the testing sets of logistic regression and (C-D) show the ROC curves of SVM model.

6.4 Discussion

In this study, depth-resolved human ovary and fallopian tube *en face* scattering coefficient maps are presented for the first time. The scattering coefficient map of malignant and benign ovarian tissues shows differences attributed to the presence of malignancy. Benign ovarian tissue demonstrated a homogeneous scatter distribution with high average scattering coefficient. Malignant ovarian tissues were heterogeneous with generally lower subsurface scattering coefficient. The difference between the scattering properties of the samples can be attributed to the reorganization of collagen in the ovarian tissue, although we did not directly test this. When cancer

develops in healthy ovaries, it invades the collagen network and causes the remodeling of collagen architecture.[21,22] This results in the heterogeneous distribution seen in Figure 6.2e.

In addition, we can summarize the scattering coefficient maps by calculating mean, variance, entropy, skewness, kurtosis, and energy, which statistically separate benign from malignant tissues (Figure 6.4). Both LR and SVM models were trained based on these histogram features and achieved a high sensitivity, specificity, and AUC in testing. These interesting results indicate that OCT may be possible to predict the risk of cancer before surgery, which could potentially aid in clinical decision-making (e.g., prioritizing surgical cases with higher risk of malignancy, avoiding unnecessary resection of low-risk cases, or triaging patients for referral to a gynecologic oncologist). It is worth to mention that the training and testing datasets are small (60 for training and 30 for testing), and overfitting can occur when the training dataset is limited. We have selected the minimal number of independent predictors (one optimal set has 3 parameters, and second has 2 parameters) for each prediction tests, performed 100 times cross-validation, and used fairly high amounts (33%) of the sample data for testing. The performances of the prediction models based on respective training and testing datasets are similar with no obvious pattern of higher AUC values for training data and much lower AUCs for testing data, which would be expected if there were problem of overfitting. With more patients recruited to the study, we will be able to establish a large database to validate prediction models with more input predictors.

The malignant cases reported in this study were at various stages including stage I (for the Sertoli-Leydig cell tumor), stage II (one high-grade serous cancer) and stage III (three high-grade serous cancers). Thus, a range of stages were represented. The progression from stage I to IV, based on the definitions of the International Federation of Gynecology and Obstetrics, does not necessarily involve more extensive involvement of the ovary, but rather is based on involvement of remote

sites in the pelvis (stage II), abdomen (stage III) or elsewhere (stage IV). Therefore, one would not *a priori* expect the imaging characteristics of stage I ovarian cancers to differ from those of more advanced cases; the ovary could be involved to the same extent in any of these stages. The *volume* of cancer in an ovary may range from small to large, and it is plausible that the scattering maps of ovarian cancer tissue might vary depending on the size of the tumors. Our tumors did range from 5.5 to 10 cm in diameter (Table 6.1). It might be desirable to explore the operating characteristics of the imaging over a wider range of sizes. We would underline that this was a proof of principle study intended to document the imaging characteristics of benign as compared to malignant tissue. Once these characteristics are known, they can then be applied to ambiguous or difficult cases. It will eventually be important to determine the sensitivity and specificity of the OCT technique in a real-world mix of cases, including early-stage and small cases. Ovarian cancer is usually detected at advanced stage, and is often clinically “silent” until the tumor reaches a large size. It is therefore not surprising that our relatively small sample of convenience consisted of larger tumors.

Our study provides evidence that the benign fallopian tubes demonstrate different microscopic scattering distribution as compared to ovarian tissues. We have made the assumption that benign entities can be considered together (regardless of specific histologic diagnosis) and that malignant entities can be considered together, an assumption that is supported by the homogeneity of features in each group, as shown in Figure 4. A limitation of our study is the lack of malignant fallopian tubes. Studies have shown that the fallopian tube is the origin of high-grade serous carcinoma, which is the most common and most lethal subtype of ovarian cancer.[23-25] Keenan *et al.* provided B-scan images using an OCT falloscope imaging porcine fallopian tubes, presumably benign.[26] Madore *et al.* showed B-scan images of a fresh excised healthy human fallopian tube.[27] These studies focus on proving the feasibility of falloscope and providing qualitative

OCT images. Our future work will be focused on quantitative discrimination of microscopic scattering changes in benign and malignant fallopian tubes. Because malignant fallopian tubes are rare, a larger scale clinical study is needed.

A limitation of this study is that we have studied only the most common pathologic entities to occur in the ovary. A real-world mix of patients will include a larger spectrum of diagnoses, including tumors of other epithelial cell types, borderline tumors, sex cord-stromal tumors, germ cell tumors, metastatic tumors, and benign processes that enlarge the ovary such as tubo-ovarian abscess and endometriosis. Some more complicated cases will be included in future studies, including but not limited to specimens with a mixture of pathologies and ovaries with subtle involvement. Moving forward, one critical obstacle for translating OCT into *in vivo* imaging as a clinical screening technique will be data acquisition. As ovaries are deeply buried within the human abdomen, it is challenging to access them. Several approaches have been proposed so far, including OCT laparoscopy and falloposcopy. Future studies will focus on endoscopic OCT designs and evaluate them *in vivo*.

Currently, all image post-processing is performed in MATLAB. The total image post-processing time for a 5 mm by 1 cm (500 B-scans, 1000 A-lines/B-scan, and 1024 pixels/A-line) area is 12 hours on a Dell Inspiron 3650 (64 bits, Intel Core i5-6400 CPU @ 2.70GHz, 8GB RAM), which is too long for real-time decision-making. Future work will need to focus on algorithm optimization for faster and more accurate surface delineation and scattering coefficient fitting, and on GPU implementation for improving computational speed. Certainly, an automatic scattering coefficient map segmentation algorithm is needed for real-time data processing. Many automatic segmentation algorithms for OCT images have been implemented, e.g., feature-based segmentation and machine learning based methods. A suitable methodology will be thoroughly

explored in the future. The final goal is to provide real-time quantitative assessment of microscopic optical scattering changes associated with development and progression of ovarian cancers.

References

- [1] D. Huang, E. A. Swanson, C. P. Lin, J. S. Schuman, W. G. Stinson, W. Chang, M. R. Hee, T. Flotte, K. Gregory, C. A. Puliafito, J. G. Fujimoto, *Science* 1991, 254(5035):1178-81.
- [2] G. J. Tearney, M. E. Brezinski, B. E. Bouma, S. A. Boppart, C. Pitris, J. F. Southern, J. G. Fujimoto, *Science* 1997, 276(5321):2037-9.
- [3] B. E. Bouma, S. Yun, B. J. Vakoc, M. J. Suter, G. J. Tearney, *Curr. Opin. Biotechnol.* 2009, 20(1):111-8.
- [4] T. Wang, L. Xie, H. Huang, X. Li, R. Wang, G. Yang, Y. Du, G. Huang, *Chin. Opt. Lett.* 2013, 11(11):111102.
- [5] S. A. Boppart, A. Goodman, J. Libus, C. Pitris, C. A. Jessor, M. E. Brezinski, J. G. Fujimoto, *Br. J. Obstet. Gynaecol.* 1999, 106(10):1071-7.
- [6] M. Keenan, T. H. Tate, K. Kieu, J. F. Black, U. Utzinger, J. K. Barton, *Biomed. Opt. Express* 2017, 8(1):124-136.
- [7] Y. Yang, T. Wang, N. C. Biswal, X. Wang, M. Sanders, M. Brewer, Q. Zhu, *J. Biomed. Opt.* 2011, 16(9):090504.
- [8] T. Wang, Y. Yang, Q. Zhu, *Biomed. Opt. Express* 2013, 4(5):772-7.
- [9] C. A. Lingley-Papadopoulos, M. H. Loew, M. J. Manyak, J. M. Zara, *J. Biomed. Opt.* 2008, 13(2):024003.
- [10] X. Qi, M. V. Sivak, G. Isenberg, J. E. Willis, A. M. Rollins, *J. Biomed. Opt.* 2006, 11(4):044010.

- [11] T. Marvdashti, L. Duan, S. Z. Aasi, J. Y. Tang, A. K. Ellerbee Bowden, *Biomed. Opt. Express* 2016, 7(9):3721-3735.
- [12] Y. Gan, D. Tsay, S. B. Amir, C. C. Marboe, C. P. Hendon, *J. Biomed. Opt.* 2016, 21(10):101407.
- [13] T. W. Sawyer, S. Chandra, P. F. S. Rice, J. W. Koevary, J. K. Barton, *Phys. Med. Biol.* 2018, 63(23):235020.
- [14] N. Just, *Br. J. Cancer* 2014, 111(12):2205-13.
- [15] A. Sadeghi-Naini, N. Papanicolau, O. Falou, J. Zubovits, R. Dent, S. Verma, M. Trudeau, J. F. Boileau, J. Spayne, S. Iradji, E. Sofroni, J. Lee, S. Lemon-Wong, M. Yaffe, M. C. Kolios, G. J. Czarnota, *Clin. Cancer Res.* 2013, 19(8):2163-74.
- [16] K. A. Miles, B. Ganeshan, M. P. Hayball, *Cancer Imaging* 2013, 13(3):400-6.
- [17] S. Nandy, A. Mostafa, P. D. Kumavor, M. Sanders, M. Brewer, Q. Zhu, *J. Biomed. Opt.* 2016, 21(10):101402.
- [18] I. S. Saidi, S. L. Jacques, F. K. Tittel, *Appl. Opt.* 1995, 34(31):7410-8.
- [19] J. M. Watson, S. L. Marion, P. F. Rice, D. L. Bentley, D. G. Besselsen, U. Utzinger, P. B. Hoyer, J. K. Barton, *Cancer Biol. Ther.* 2014, 15(1):42-60.
- [20] T. Wang, M. Brewer, Q. Zhu, *Wiley Interdiscip. Rev. Nanomed. Nanobiotechnol.* 2015, 7(1):1-16.
- [21] D. Arifler, I. Pavlova, A. Gillenwater, R. Richards-Kortum, *Biophys. J.* 2007, 92(9):3260-74.
- [22] S. Nandy, H. S. Salehi, T. Wang, X. Wang, M. Sanders, A. Kueck, M. Brewer, Q. Zhu, *Biomed. Opt. Express* 2015, 6(10):3806-11.
- [23] R. J. Kurman, I. M. Shih, *Am. J. Surg. Pathol.* 2010, 34(3):433-43.

- [24] B. K. Erickson, M. G. Conner, C. N. Landen Jr., *Am. J. Obstet. Gynecol.* 2013, 209(5):409-14.
- [25] S. H. George, R. Garcia, B. M. Slomovitz, *Front. Oncol.* 2016, 6:108.
- [26] M. Keenan, T. H. Tate, K. Kieu, J. F. Black, U. Utzinger, J. K. Barton, *Biomed. Opt. Express* 2017, 8(1):124-136.
- [27] W. J. Madore, E. De Montigny, A. Deschenes, F. Benboujja, M. Leduc, A. M. Mes-Masson, D. M. Provencher, K. Rahimi, C. Boudoux, N. Godbout, *J. Biomed. Opt.* 2017, 22(7):76012.

Chapter 7: Conclusion and Future Work

In this dissertation, optical imaging modalities combined with computer-aided diagnosis were applied for *ex vivo* human colorectal and ovarian tissue diagnosis and assessment. Quantitative optical properties related to tissue absorption and scattering, as well as morphological properties were evaluated and classified for discriminating different types of colorectal and ovarian tissues.

In the first study, the use of swept-source optical coherence tomography and a novel quantitative feature to differentiate malignant from normal tissue were demonstrated in nine fresh human colon specimens. Subsurface scattering coefficient maps were automatically generated, and ASI were calculated for each imaged specimen. We found significant qualitative and quantitative differences between normal and malignant tissue. While further system optimization and clinical testing are required, we conclude that SS-OCT may provide new diagnostic information when screening for early cancers or surveilling known disease following oncologic therapy.

In the second study, we report the first usage of a RetinaNet-based PR-OCT system to distinguish normal from neoplastic tissue within human colorectal specimens with real-time diagnosis capability. Quantitative scoring of the estimated probability of a normal specimen was used to evaluate performance. The results presented suggest that PR-OCT may differentiate normal from cancerous colon rapidly, potentially enabling for real-time use.

In the third study, texture features and computer vision-based image features acquired from scattering coefficient maps were used to differentiate malignant, polypoid, and normal colorectal tissue types. Two classifications were assigned: abnormal tissue vs. normal tissue and adenomatous polyp vs. cancerous tissue. The results indicate that SVM with computer vision-based features is suitable for distinguishing abnormal and normal tissues, while RF with texture features shows better performance in identifying benign polyps. Based on these results, we

conclude that the scattering map derived from OCT images can provide qualitative and quantitative information which demonstrates the potential for aiding the diagnosis of human colorectal tissues. We are currently working on integrating the OCT system into the commercial endoscopic system for *in vivo* human colon evaluation. Work is going on to combine the neural network with the endoscopic system that can be readily used as a guiding tool for intraoperative image guided colorectal tissue screening.

In the fourth study, an AdaBoost-based multiwavelength SFDI system was used for the classification of colorectal tissues including normal, malignant, and adenomatous polyp specimens. Wide-field absorption and scattering maps were estimated for colorectal specimens over nine wavelengths. Drastically different quantitative characteristics were captured by SFDI. Elevated absorption coefficient among tumors were uniformly noted along with decreased scattering coefficient as a contrast to normal specimens, which may result from structural disruption of highly organized colorectal tissues. Adenomatous polyps were found to have a lower absorption coefficient than tumors and lower scattering coefficient than normal colorectal tissues.

In the final study, depth-resolved human ovary and fallopian tube *en face* scattering coefficient maps are presented for the first time. The scattering coefficient map of malignant and benign ovarian tissues shows differences attributed to the presence of malignancy. The difference between the scattering properties of the samples can be attributed to the reorganization of collagen in the ovarian tissue, although we did not directly test this. Initial results indicate that quantitative scattering features extracted from the OCT images can be used to identify ovarian cancer. We are currently developing an endoscope OCT system for imaging the fallopian tube, which is suspected to be the origin of human ovarian cancer. In the meantime, we are accumulating more *ex vivo* fallopian tube data.

Curriculum Vitae

Yifeng Zeng

EDUCATION

2021(expected)	Washington University in St. Louis Ph.D. in Biomedical Engineering
2016	Tsinghua University B. Eng. in Engineering Physics

PEER REVIEWED JOURNAL PUBLICATIONS

1. **Zeng, Yifeng**, William C. Chapman Jr, Yixiao Lin, Shuying Li, Matthew Mutch, and Quing Zhu. "Diagnosing colorectal abnormalities using scattering coefficient maps acquired from optical coherence tomography." *Journal of Biophotonics* 14, no. 1 (2021): e202000276. (Inside Cover)
2. Li, Shuying*, **Yifeng Zeng***, William C. Chapman Jr, Mohsen Erfanzadeh, Sreyankar Nandy, Matthew Mutch, and Quing Zhu. "Adaptive Boosting (AdaBoost)-based multiwavelength spatial frequency domain imaging and characterization for ex vivo human colorectal tissue assessment." *Journal of biophotonics* 13, no. 6 (2020): e201960241. (Inside Cover)
3. **Zeng, Yifeng***, Shiqi Xu*, William C. Chapman Jr, Shuying Li, Zahra Alipour, Heba Abdelal, Deyali Chatterjee, Matthew Mutch, and Quing Zhu. "Real-time colorectal cancer diagnosis using PR-OCT with deep learning." *Theranostics* 10, no. 6 (2020): 2587.
4. **Zeng, Yifeng**, Sreyankar Nandy, Bin Rao, Shuying Li, Andrea R. Hagemann, Lindsay K. Kuroki, Carolyn McCourt et al. "Histogram analysis of en face scattering coefficient map predicts malignancy in human ovarian tissue." *Journal of biophotonics* 12, no. 11 (2019): e201900115.

5. Rao, Bin*, Xiandong Leng*, **Yifeng Zeng***, Yixiao Lin, Ruimin Chen, Qifa Zhou, Andrea R. Hagemann et al. "optical Resolution photoacoustic Microscopy of ovary and fallopian tube." *Scientific reports* 9, no. 1 (2019): 1-9.
6. **Zeng, Yifeng***, Bin Rao*, William C. Chapman*, Sreyankar Nandy, Rehan Rais, Iván González, Deyali Chatterjee, Matthew Mutch, and Quing Zhu. "The angular spectrum of the scattering coefficient map reveals subsurface colorectal Cancer." *Scientific reports* 9, no. 1 (2019): 1-11.
7. Samanta, Suranjana, Jianyong Jiang, Dezhuang Ye, Maya Hutchinson, **Yifeng Zeng**, Shuying Li, Xiaohui Zhang et al. "Point-of-Care PET/Ultrasound Imaging for Detection of Atherosclerotic Vulnerable Plaque: A Feasibility Study." *Journal of Nuclear Medicine* 61, no. supplement 1 (2020): 310-310.
8. Jiang, Jianyong, Ke Li, Beichuan Qi, Sergey Komarov, Joseph A. O'Sullivan, **Yifeng Zeng**, Ryan Wahidi, Quing Zhu, and Yuan-Chuan Tai. "Development of a simultaneous PET/Ultrasound imaging system with near real-time reconstruction capability for point-of-care applications." In *2017 IEEE Nuclear Science Symposium and Medical Imaging Conference (NSS/MIC)*, pp. 1-3. IEEE, 2017.
9. Gan, Yingjie, Atieh Talebzadeh, Xiaoying Xu, Satyajeet Shinde, **Yifeng Zeng**, Ki-Hyuk Kim, and David Pommerenke. "Experimental Characterization and Modeling of Surface Discharging for an Electrostatic Discharge (ESD) to an LCD Display." *IEEE Transactions on Electromagnetic Compatibility* 60, no. 1 (2017): 96-106.